# PROTECT2024

9th International Colloquium on Performance, Protection & Strengthening of Structures Under Extreme Loading & Events

13 - 16 August 2024 I Singapore

## CONFERENCE PROCEEDINGS

Organised by

NANYANG TECHNOLOGICAL UNIVERSITY SINGAPORE

NTU CEE Alumni Association

# LIST OF TECHNICAL PAPERS

| ID Number | Authors (s) – Paper Title |
|---|---|
| PS-2 | ***Pengfei He, Dan Gan, Lei Gao, Xuhong Zhou –*** Topology optimization and tensile behavior of square concrete–filled steel tubular connections with diagonal plates |
| PS-3 | ***Li Yang, Gan Dan, Xuhong Zhou -*** Seismic Analysis Of Steel Staggered Truss Framing Structure With Flexible Connection Between Slab And Chord |
| PS-4 | ***Y.Y.Y. Cao, Dianyi Song, Yimin Huang, Song Li -*** Enhancing The Damage Resistance Of High-strength Concrete Under Penetration By An Optimized Layered-structure Concept |
| PS-14 | ***Anupoju Rajeev, Prince Jeya Lal Lazar –*** Structural Integrity Of Mild Steel Sandwich Panels Subjected To Air-backed Underwater Shock Loads |
| PS-15 | ***Chao Hou, Wendong Chen, Gen Li –*** Research Advancement On CFST With Localized Pitting Corrosion Subjected To Static And Impact Loading |
| PS-17 | ***Rujin Ma, Huseyin Saglik, Zichao Pan, Airong Chen*** - The Performance Of Cable Clamp Systems In Suspension Bridges Considering Bolt Fracture Under Vehicle Fire |
| PS-20 | ***Shen Liu –*** Seismic Performance Of A Hybrid System Of Hot-rolled Steel Frame And Steel Sheathed Cold-formed Steel Shear Wall |

# Topology optimization and tensile behavior of square concrete–filled steel tubular connections with diagonal plates

*Pengfei He[1], Dan Gan[2]*, Lei Gao[3], Xuhong Zhou[4]*

[1] School of Civil Engineering, Chongqing University, 15537898976@163.com.

[2] School of Civil Engineering and Geomatics, Southwest Petroleum University, gand03@qq.com.

[3] School of Civil Engineering, Chongqing University, 1406862722@qq.com.

[4] School of Civil Engineering, Chongqing University, zhouxuhong@126.com.

**Corresponding Author*: Dan Gan, PhD, Professor.**

Southwest Petroleum University, Chengdu, China, 610500. **Email:** gand03@qq.com.

## ABSTRACT

This work proposes a square concrete–filled steel tubular (CFST) joint system, in which vertically placed diagonal plates help transfer the tensile load from the beam flanges. Then, a variable density method is used to validate that the exterior–diaphragm of square CFST connections can be largely reduced or even eliminated. Seven square CFST connections with diagonal plate were experimentally and comparatively investigated under tension. Studied parameters included the width and thickness of beam flange, length and thickness of diagonal plate. The failure mode, initial stiffness, yield load, and peak load were analyzed based on the test results. The failure modes of the tested specimens included fracture of the beam flanges, fracture of welds—between the beam flange and the steel tube corner—after the beam yielding, and fracture of welds at the corner of the steel tube column and fracture of the diagonal plate. The failure mode of the connections depends on the strength of the beam and connection, and varying thickness and width of beam flanges would change the strength of the beam, which affects the failure mode. Finally, theoretical formulas are presented to predict the yield capacities of the connections, and the predicted results agree well with the test results. The diagonal–plate connection has the advantages of conveniently concrete pouring and not occupying indoor space, and thus provides an alternative for CFST construction.

***Keywords:*** *Concrete filled steel tube; Beam to column joint; Exterior diaphragm; Composite connection; Topology optimization; Tensile yield bearing capacity.*

## 1. INTRUCTION

Composite construction with concrete–filled steel tubular (CFST) columns and steel beam joints is widely used in building structures [1,2]. The commonly used joint types [3,4] include interior–diaphragm joint (Fig. 1a), through–diaphragm joint (Fig. 1b), and exterior–diaphragm joint (Fig. 1c). Engineering practice and academic research show that all the three types of joints have high load capacity, high stiffness, and good seismic behavior [5–9]. The interior–

diaphragm joint is mainly used in joints with large column cross–sections due to the laborious welding work of the diaphragm, which needs electro slag welding or to be conducted inside the steel tube. The through–diaphragm joint can be seen as a compromise between the interior– and exterior–diaphragm joint, and the column steel tube needs to be disconnected at the through–diaphragm. The exterior–diaphragm joint is with simple construction process, and easy to guarantee the quality of concrete pouring.

An exterior diaphragm has a non–direct force transfer path. If an exterior diaphragm has a small dimension, stress concentration at the steel tube corners may lead to premature fracture failure when subjected to earthquakes [10]. Therefore, exterior diaphragms, designed according to the current code, account for a large proportion of steel (about 1/3) of the CFST column. In addition, exterior diaphragms occupy the indoor building space and are aesthetically unappealing.

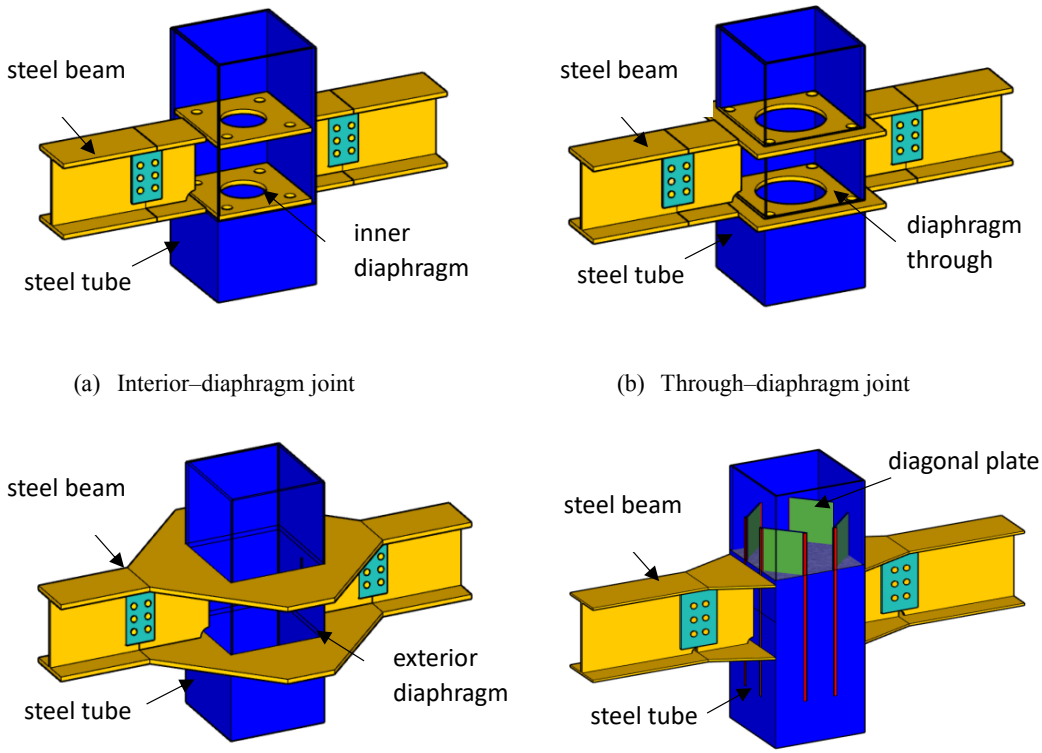


(a) Interior–diaphragm joint

(b) Through–diaphragm joint

(c) Exterior–diaphragm joint

(d) Diagonal–plate joint

Fig. 1 CFST joints

In order to reduce the size of the exterior diaphragm or even eliminate it, this work proposes to set diagonal plates in the joint region based on the research on stiffened CFST columns [11], and the vertically placed diagonal plates also do not hinder concrete pouring. Subsequently, the exterior–diaphragm connection stiffened with diagonal plate is optimized by using the variable density method—the less stressed region of the exterior diaphragm is gradually removed [12]. Then, the CFST diagonal–plate connection is obtained (Fig. 1d).

The diagonal–plate joint has a reasonable force transfer path. In the vertical direction, diagonal plates act as shear connectors and effectively transfer the shear force from the steel beam to the concrete. In the transverse direction, diagonal plates effectively transfer the tension or compression force from the beam flange to the steel tube and concrete. Combined with the extended flange, the diagonal–plate joint shown in Fig. 1d effectively relieves the stress concentration at the steel tube corners and can relocate the plastic hinge or the failure position.

A beam–end moment is resisted by the force couple acting on beam flanges shown in Fig. 2, i.e., a tensile force and a compressive force. The failure of CFST joints mainly depends on the connection between the tensile flange and the column tube. Therefore, the tensile behavior of connections is very important, which provides the basis for investigating the seismic behavior of diagonal–plate joints. The tensile behavior of the joint can be equivalent to that of an equivalent T–stub [13–15].

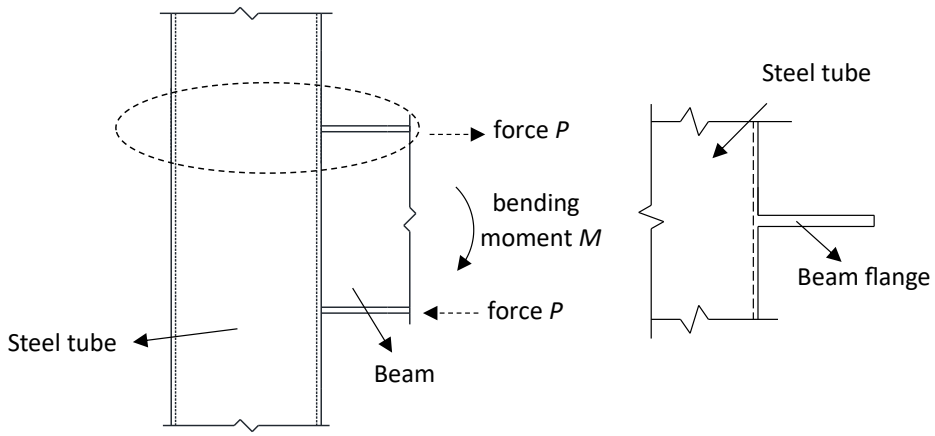


(a) Joint elevation (b) Equivalent T–stub

Fig. 2 Schematic diagram of the force coupling of bending moment at the beam end

Most laboratory testing in the past mainly investigated the tensile behavior of a single type of CFST connection. Park et al [16], Yu et al [17] and Qin et al [18] conducted tensile tests on the exterior–diaphragm, interior–diaphragm, and through–diaphragm CFST connections, respectively; the tensile properties and force transfer mechanism were investigated, and the load–capacity predicting methods were proposed based on the yield line theory. Zhu et al [19] conducted tensile tests on the CFST exterior–diaphragm connections stiffened with PBL, and the improvement of the tensile behavior by the setting PBL and the effect of removing the exterior diaphragm on the tensile behavior were investigated. The above investigations on the load–resisting mechanism and design method of connections under tension can be used as a reference for diagonal–plate connections.

In this work, tensile testing of seven square CFST column–to–steel beam connections were carried out, the test parameters included the width and thickness of the beam flange and the length and thickness of diagonal plates. Theoretical formulas are presented to predict the yield capacities of the connections.

## 2 TOPOLOGY OPTIMIZATION OF CONNECTION

Four CFST connection specimens with diagonal plate were designed and tested to evaluate the tensile behavior (Fig. 3).

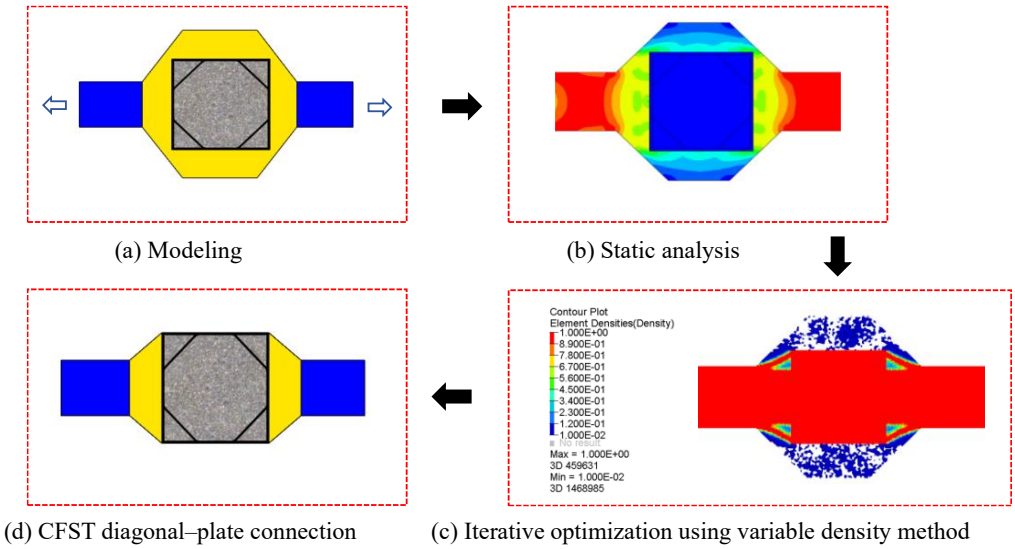


(a) Modeling (b) Static analysis

(d) CFST diagonal–plate connection (c) Iterative optimization using variable density method

Fig. 3 Connection optimization process

The external diaphragm can be largely reduced when vertical diagonal plates are placed to help transfer the bending moment from the beam end. Therefore, optimization was conducted, and the optimization process for obtaining the diagonal–plate joints is as follows (see Fig. 3) [20, 21]:

1) A 3D model of the connection was established using SolidWorks, which was input into the OptiStruct solver module in Altair HyperWorks (Fig. 3a).

2) Finite element analysis was conducted to obtain the stress contour of the connection (Fig. 3b).

3) The optimization objective of the connection was stiffness maximization, the constraint was 40% structural volume fraction, and the design variable was cell mesh density. Then, the variable density optimization algorithm was used to optimize the specified (yellow) region of the exterior diaphragm. In addition, to reduce the number of cell meshes, a penalty factor ($p$=3.0) was set within the OptiStruct module, thus forcing the cell meshes to tend to be retained or removed. Finally, convergence results were obtained when the calculated values were changed by less than a given convergence tolerance of 0.5% in any two consecutive iterations (Fig. 3c).

4) The surface feature points of the model after topology optimization were captured using Rhino 5.0 to reconstruct the connection model. And the CFST diagonal–plate connection was obtained by combining engineering experience (Fig. 3d).

## 3 EXPERIMENTAL PROGRAM

### 3.1 Test specimens

The test matrix included beam flange width ($b_b$), beam flange thickness ($t_b$), diagonal plate length ($l_d$) and diagonal plate thickness ($t_d$), as shown in Table 1. CJD denotes diagonal plate connection and CJE denotes exterior–diaphragm connection. Taking specimen CJD–100–8–100–6 as an example, the Arabian numbers in the designation indicate the beam flange width of 100 mm, beam flange thickness of 8 mm, diagonal–plate height of 100 mm and diagonal plate thickness of 6 mm, respectively.

The reference exterior–diaphragm connection CJE–100–8–0–8 was un–optimized (Fig. 4), and was designed according to the technical code for CFST structures (GB/T 50936–2014) [4] and Wang's work [10]. Specimen CJD–100–8–100–6 was the optimized counterpart (Fig. 5). Specimen CJD–100–8–100–6, CJD–100–8–200–6, and CJE–100–8–0–8 were expected to be failed at the beam, while the remaining specimens were expected to be failed at the welds at the steel tube corners from preliminary finite element analysis.

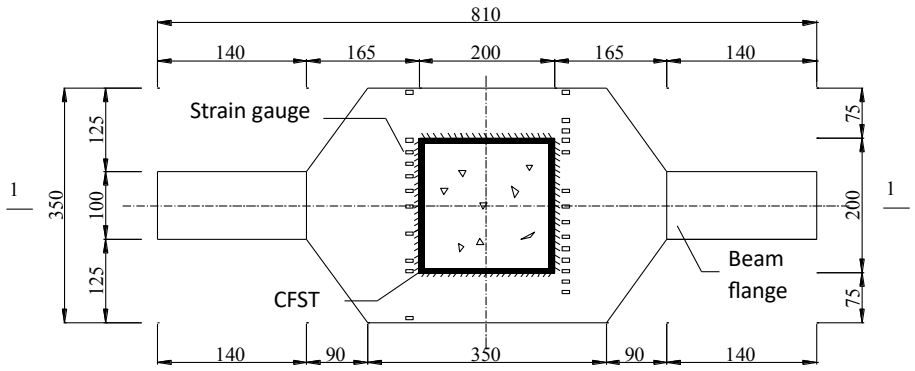


(a) Plan

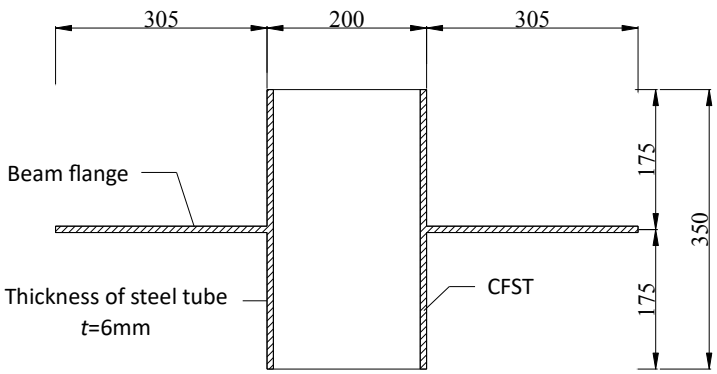


(b) Elevation

Fig. 4 Details and dimension of CJE–100–8–0–8

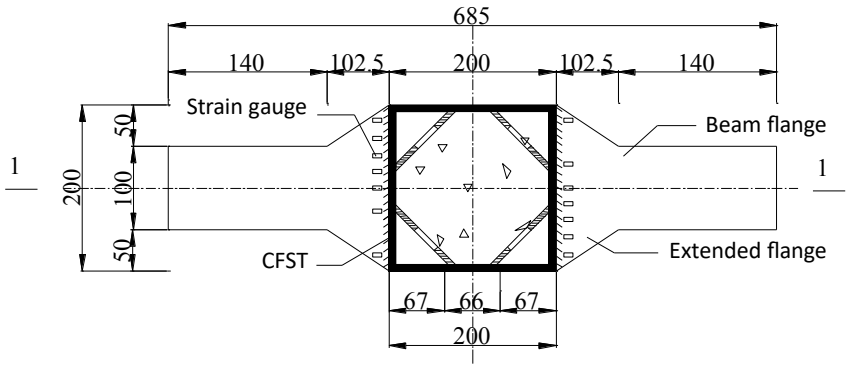


(c) Plan

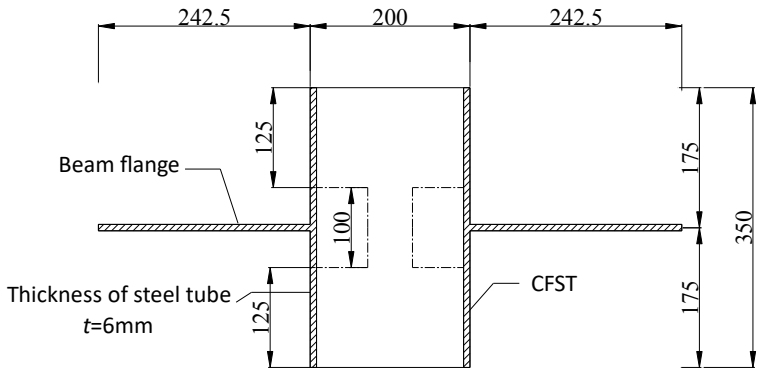


(d) Elevation

Fig. 5 Details and dimensions of CJD–100–8–100–6

**Table 1.** Parameters of test specimens

| Specimens | $b_b$ (mm) | $t_b$ (mm) | $l_d$ (mm) | $t_d$ (mm) |
|---|---|---|---|---|
| CJE–100–8–0–8 | 100 | 8 | – | – |
| CJD–100–8–100–6 | 100 | 8 | 100 | 6 |
| CJD–100–8–200–6 | 100 | 8 | 200 | 6 |
| CJD–100–8–100–2 | 100 | 8 | 100 | 2 |
| CJD–130–8–100–6 | 130 | 8 | 100 | 6 |
| CJD–130–8–100–8 | 130 | 8 | 100 | 8 |
| CJD–100–12–100–6 | 100 | 8 | 100 | 6 |

The installation method of the diagonal plate is shown in Fig. 6. Firstly, cut openings in the wall of a structural steel tube, and then insert diagonal plates into the openings and weld them. A full penetration butt weld was used to connect the beam flange plate or exterior diaphragm to the steel tube.

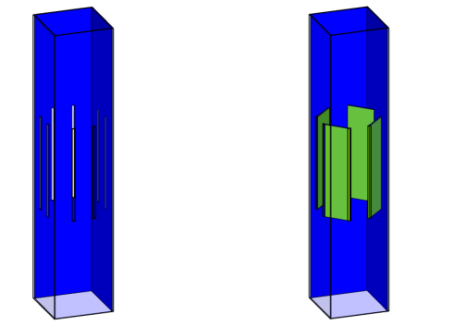


Fig. 6 Installation of diagonal plates

### 3.2 Material properties

The concrete compressive strength ($f_{cu}$) was measured by six 150×150×150 mm cubes cured under the same conditions as the test specimens [22–25]. The average value of the measured strength was 50.2 MPa. The material properties of the steel tube, exterior diaphragm, beam flange and diagonal plate were obtained by testing three coupons [26–28], and the results are shown in Table 2.

**Table 2.** Material properties of steel

| Nominal thickness (mm) | Measured thickness (mm) | Yield strength (MPa) | Ultimate strength (MPa) | Elastic modulus (MPa) | Elongation (%) |
|---|---|---|---|---|---|
| 2 | 1.9 | 179.0 | 315.5 | 180 911 | 46.5 |
| 6 | 5.5 | 298.2 | 443.2 | 186 982 | 31.5 |
| 8 | 7.4 | 289.1 | 430.3 | 185 768 | 35.0 |
| 12 | 11.6 | 238.2 | 381.8 | 174 349 | 34.5 |

### 3.3 Test procedure

The loading device is shown in Fig. 7. The tensile testing was conducted by using a 600 kN electro–hydraulic servo testing machine, which adopted a displacement control loading method. Both flanges of the specimen were clamped, and the upper flange was fixed and the tension displacement was applied at the lower flange.

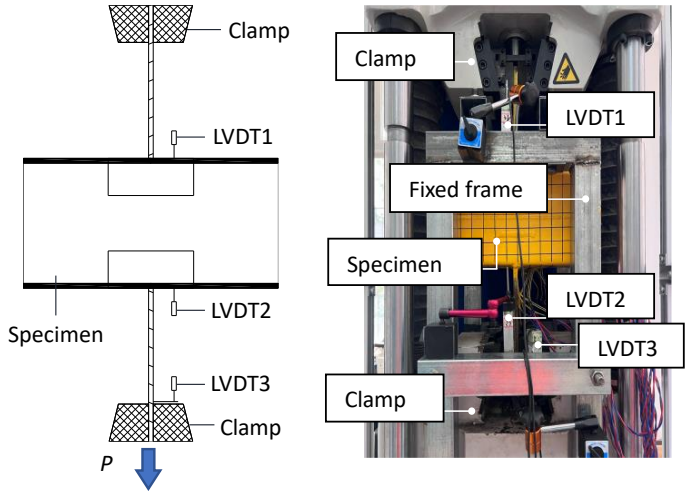


Fig. 7 Test setup

The deformation of the joint region of the specimen was measured by two Linear Variable Displacement Transducers (LVDT1 and LVDT2), and the overall deformation of the specimen was measured by LVDT3. The longitudinal strains of the beam were measured by strain gauges, which were located at the extended flange or the exterior–diaphragm and 20 mm away from the edge of the column steel tube.

## 4 TEST RESULT

### 4.1 Failure modes

#### *4.1.1 Fracturing at the beam*

As shown in Figs. 8(a)–(c), exterior–diaphragm connection CJE–100–8–0–8, and diagonal–plate connections CJD–100–8–100–6 and CJD–100–8–200–6 fractured at the end of the beam flange. They showed similar failure pattern. Before reaching the yield load of each specimen, there were no obvious test observations in all specimens. When the loading was closed to the ultimate load, the crack first appeared at the end of the flange and rapidly developed towards the center, and the displacement increased rapidly until the steel fractured. After the testing, the steel tube was cut, and it was found that the welds between the steel tube and diagonal plate were intact, and the joint region was not damaged during the loading process.

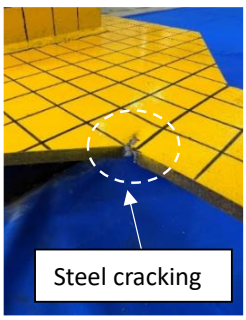


(a) CJE–100–8–0–8

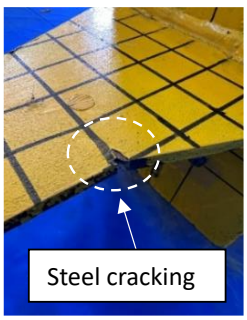


(b) CJD–100–8–100–6

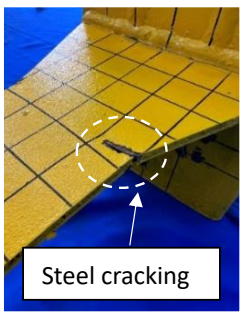


(c) CJD–100–8–200–6

Fig. 8 Failure modes of specimens

### *4.1.1 Fracturing at weld*

The weld between the extended flange and the steel tube corners of diagonal–plate connection CJD–100–8–100–2 fractured, as shown in Fig. 9(a). At the initial stage of loading, a slight outward deformation of the steel tube flange was observed. When the load approached the ultimate load, cracks occurred at the welds of the corners. Subsequently, the load carrying capacity of the specimen decreased dramatically, which eventually led to the termination of the test. The steel tube showed large out–of–plane deformation, but the beam flanges did not yield. After the testing, the steel tube was cut open and found that the weld between a diagonal plate and the column steel tube fractured, as shown in Fig. 9(a).

The welds between the extended flange and the steel tube corners of diagonal–plate connections CJD–130–8–100–6, CJD–100–12–100–6 and CJD–130–8–100–8 fractured after the beam flange yielded, as shown in Fig. 9(b)–(d). The observations during the test were similar to the failure mode of the weld fractured before the beam flange yielded, except that he out–of–plane deformation of the steel tube was not obvious during the loading process since the restraint of the diagonal plates. That the beam flange yielded first led to a yielding platform showing in the load displacement curve. After the test, the steel tube was cut open, and it was found the weld between the diagonal plate and the steel tube was intact.

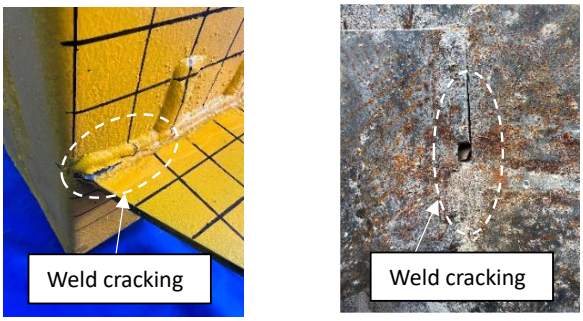


(a) CJD–100–8–100–2

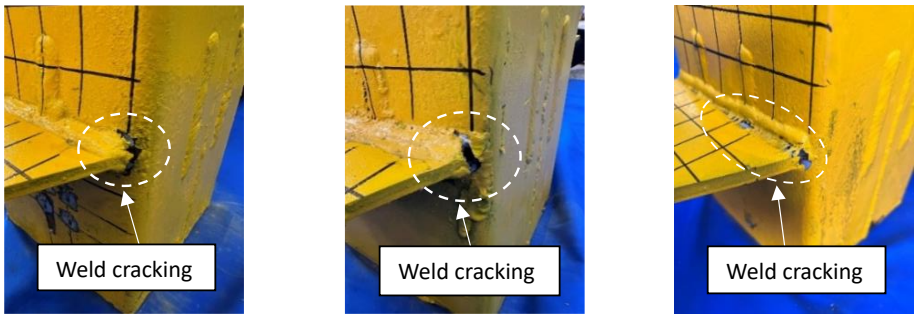


(b) CJD–130–8–100–6 (c) CJD–130–8–100–8 (d) CJD–100–12–100–6

Fig. 9 Failure modes of specimens

### 4.2 Comparative analysis of load–displacement curves

The measured tensile load ($P$) versus deformation ($\Delta$) curves for all the specimens are shown in Fig. 10. For a quantitative comparison of the curve characteristics, the measured initial stiffness ($K_0$), yield load ($P_y$), peak load ($P_u$) and limit displacement ($\Delta_u$) are listed in Table 3. $K_0$ is defined as the slope of the $P$–$\Delta$ curves. $P_y$ is the test measured yield load. All specimens except specimen CJD–100–8–100–2 had a yield plateau. The yield load for specimen CJD–100–8–100–2 was determined based on the geometric graphic method [29]. The theoretical yield load $F_y$ is also given in Table 3, which is defined as the product of the measured cross–sectional area of the steel beam and the measured yield strength. The average ratio of $P_y$ to $F_y$ was 0.93, and the difference was due to the specimen machining error and the systematic error of the loading device (minor eccentricity during loading). The measured peak load $P_u$ is defined as the maximum load, and the ultimate displacement $\Delta_u$ is defined as the displacement corresponding to $P_u$.

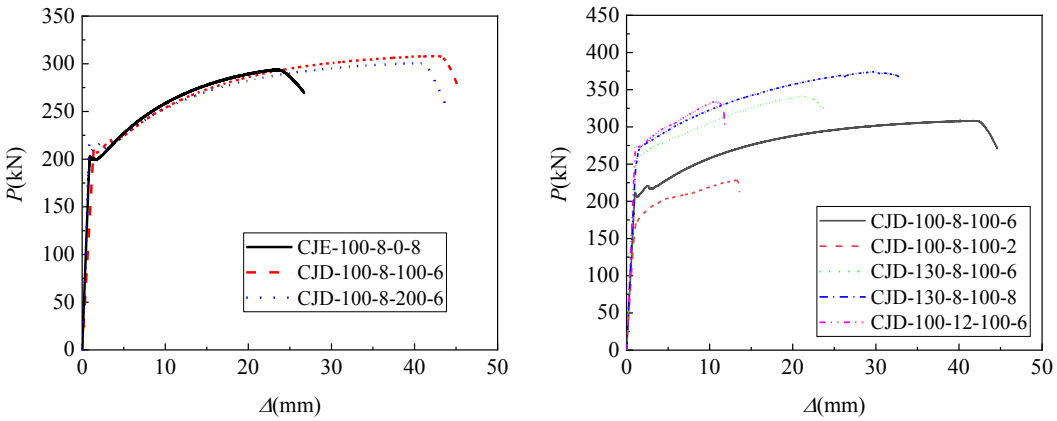


Fig. 10 Comparison of load–displacement curves

**Table 3.** Tensile mechanical property parameters

| Test piece number | initial stiffness $K_0$(kN·mm–1) | Theoretical yield load $F_y$(kN) | Measured yield load and ultimate load | | Limit displacement $\Delta_u$(mm) | Failure mode |
|---|---|---|---|---|---|---|
| | | | Yield load $P_y$(kN) | Ultimate load $P_u$(kN) | | |
| CJE–100–8–0–8 | 228.9 | 213.9 | 200.3 | 293.9 | 23.8 | F1 |
| CJD–100–8–100–6 | 199.3 | 213.9 | 218.1 | 308.3 | 42.9 | F1 |
| CJD–100–8–200–6 | 205.2 | 213.9 | 213.3 | 300.5 | 40.9 | F1 |
| CJD–100–8–100–2 | 172.1 | 213.9 | 180.4 | 228.5 | 13.7 | F2 |
| CJD–130–8–100–6 | 228.0 | 278.1 | 256.3 | 341.6 | 22.0 | F3 |
| CJD–130–8–100–8 | 233.8 | 278.1 | 273.7 | 373.7 | 30.7 | F3 |
| CJD–100–12–100–6 | 258.3 | 276.3 | 274.2 | 334.0 | 10.9 | F3 |

Note: F1 refers to the fracture of the beam flange; F2 refers to the fracture of welds at the corner of the steel tube column and fracture of the diagonal plate; F3 refers to the fracture of welds at the corner of the steel tube column after steel beam yielding.

#### *4.2.1 Tensile properties of the optimized connection compared to the original exterior–diaphragm connection*

Diagonal–plate connection CJD–100–8–100–6 realized the same failure mode of beam–flange fracture as reference exterior–diaphragm connection CJE–100–8–0–8, which indicates diagonal plates effectively transfer the beam–end load into the joint region and improve the composite effect of the steel tube and concrete. However, the initial stiffness of specimen CJD–100–8–100–6 was slightly lower (10.96%) than that of specimen CJE–100–8–0–8, indicating the vertical diagonal plates were a little lower effective in restraining the out–of–plane deformation.

#### *4.2.2 Diagonal plate height $l_d$*

CJD–100–8–200–6 with 200–mm height of diagonal plates, had similar values of the initial stiffness, yield load, ultimate load and ultimate displacement as CJD–100–8–100–6 with 100–mm height of diagonal plates. It can be inferred that the diagonal plate with a height of half of the steel tube width (100 mm) was appropriate.

#### *4.2.3 Beam flange width bb and thickness $t_b$*

Increasing the width (CJD–130–8–100–6) and thickness (CJD–100–12–100–6) of beam flanges increased the initial stiffness, yield load, and ultimate load when compared with specimen CJD–100–8–100–6, and led to a greater load capacity of the beam than that of the joint, which changed the failure mode, so reduced the ultimate displacement.

#### *4.2.4 Diagonal plate thickness $t_d$*

Reducing the thickness (CJD–100–8–100–2) of diagonal plates reduced the initial stiffness, yield load, and ultimate load compared to specimen CJD–100–8–100–6. Combined with the test observation, it is inferred that during the loading process, due to the cracking of the diagonal plate, the tensile force originally transmitted by the diagonal plate can only be transmitted through the corner of the steel tube column, where a stress concentration occurs, thus changing the failure mode and decreasing the tensile stiffness and strength.

Increasing the thickness (CJD–130–8–100–8) of diagonal plates increased the initial stiffness, yield load, and ultimate load when compared with specimen CJD–130–8–100–6, Their failure modes were all weld fracture at the corner of the steel tube. This indicates that in this failure mode, increasing the thickness of the diagonal plate enhances the restraining effect on the steel tube and reduces the out–of–plane deformation of the tube, thus improving the tensile properties of the connection.

## 5. CALCULATION OF TENSILE YIELD BEARING CAPACITY OF THE CONNECTION

As shown in Fig. 22, the horizontal load ($P_y$) transmitted from the beam flange in the diagonal–plate connection is shared by the column wall and the diagonal plate. The horizontal load on the column wall is defined as $P_{y,c}$ and the horizontal load on the diagonal plate as $P_{y,d}$. Therefore,

the tensile capacity of the joint can be obtained by calculating the capacity of these two parts separately.

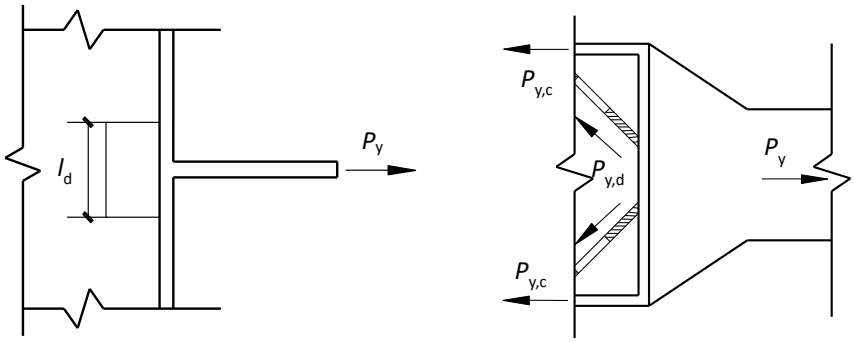


(a) Elevation (b) Plan

Fig. 22 Connection tension transmission path

The stiffening effect of the diagonal plate under tensile load will limit the bending deformation of the steel tube flange. Fig. 22 indicates that the diagonal plate serves as a longitudinal stiffener, thus limiting the force transmission length of the plate along the longitudinal direction of the steel tube. When the load reaches the yield load capacity, the length of the diagonal plate when it reaches the yield stress is defined as its transfer length ($l_{eu}$). According to the validated finite element model, the transfer length ($l_{eu}$) of each specimen is shown in Table 4.

**Table 4.** Transfer length of the diagonal plate (connection yield capacity state)

| Specimens | $l_{eu}$ (mm) |
|---|---|
| CJD–100–8–100–6 | 35 |
| CJD–100–8–200–6 | 35 |
| CJD–130–8–100–6 | 42 |
| CJD–100–12–100–6 | 40 |
| CJD–130–8–100–8 | 37 |
| CJD–100–8–100–2 | 100 |

Based on static equilibrium, the horizontal load borne by the diagonal plate is:

$$P_{y,d} = 2t_d l_{eu} f_{y,d} \tag{1}$$

Where: $t_d$ is the thickness of the diagonal plate. $f_{y,d}$ is the yield strength of the diagonal plate.

Since the expanded flange of the diagonal–plate connection is of equal width to the column, for the case of equal width of the beam and column, the following equations are proposed in the literature [30] to calculate the tensile yield capacity of the steel tube:

$$P_{y,c} = 2(t_b + t_c) f_{y,c} t_c \tag{2}$$

Where: $f_{y,c}$ is the yield strength of steel tube; $t_c$ is the thickness of the column wall.

In summary, the tensile yield capacity of the diagonal–plate connection can be calculated as:

$$P_y = P_{y,d} + P_{y,c} = 2t_d l_{eu} f_{y,d} + 2(t_b + t_c) f_{y,c} t_c \tag{3}$$

The theoretical value of the tensile bearing capacity of the diagonal plate is calculated by equation (1), the theoretical value of the tensile bearing capacity of the steel tube wall is

calculated by equation (2), and the theoretical value of the tensile yield–bearing capacity of the connection calculated by equation (3) are statistically compared with those in Table 5. Table 5 also lists the tensile yield capacity of the beam flange end, and its calculated value is the product of the cross–sectional area of the beam flange and the yield strength.

It can be seen that the failure modes of specimens CJD–100–8–100–6 and CJD–100–8–200–6 are fractures of the beam flange or stress concentration at the end of the beam flange. Their test values of tensile yielding capacity are close to the calculated values of steel beam flange capacity and smaller than the calculated values of the theoretical capacity in the joint region. The failure modes of the rest of the specimens were weld fracture at the corner of the column, and their test values of tensile yielding capacity were generally in good agreement with the theoretical capacity in the joint region. The results show that the theoretical formulation is able to accurately estimate the tensile yield capacity of the connection.

**Table 5** Comparison of experimental value and theoretical calculation value

| Test number | Test value | Theoretical value | | | | Test value/theoretical value | Test results |
|---|---|---|---|---|---|---|---|
| | $P_y^e$(kN) | Joint region | | | Steel beam | $P_y^e/P_y$ | |
| | | $P_{y,d}$(kN) | $P_{y,c}$(kN) | $P_y$(kN) | $P_y$(kN) | | |
| CJD–100–8–100–6 | 218.1 | 114.7 | 114.4 | 229.1 | 213.9 | 1.02 | F1 |
| CJD–100–8–200–6 | 213.3 | 114.7 | 114.4 | 229.1 | 213.9 | 1.00 | F1 |
| CJD–130–8–100–6 | 256.3 | 137.7 | 114.4 | 252.1 | 278.0 | 1.02 | F3 |
| CJD–100–12–100–6 | 274.2 | 131.1 | 128.2 | 259.3 | 276.3 | 1.06 | F3 |
| CJD–130–8–100–8 | 273.7 | 158.3 | 114.4 | 272.7 | 278.0 | 1.00 | F3 |
| CJD–100–8–100–2 | 180.4 | 68.0 | 114.4 | 182.4 | 213.9 | 0.99 | F2 |
| Average value | — | — | — | — | — | 1.02 | — |
| Standard deviation | — | — | — | — | — | 0.03 | — |

Note: F1 refers to the fracture of the beam flange; F2 refers to the fracture of welds at the corner of the steel tube column and fracture of the diagonal plate; F3 refers to the fracture of welds at the corner of the steel tube column after steel beam yielding.

## 6. CONCLUSION

1. The diagonal–plate connection proposed by combining the topology optimization method has the characteristics of clear force transmission, simple construction, convenient construction, does not affect the concrete casting, and does not occupy the space outside the column. The tensile test results show that the tensile mechanical properties of the diagonal–plate connection are similar to those of the exterior–diaphragm connection, and the expected beam end failure mode can be realized.

2. The failure modes of the specimens were categorized into three main types: fracture of the beam flanges, fracture of welds—between the beam flange and the steel tube corner—after the beam yielding, and fracture of welds at the corner of the steel tube column and fracture of the diagonal plate. Within the parameters of the experimental study, an increase in the thickness and width of the beam flange leads to a shift in the failure mode of the specimen, and an increase in the length and thickness of the diagonal plate has no effect on the failure mode of the specimen.
3. The increase in the thickness and width of the beam flange and the thickness of the diagonal plate resulted in an upward trend in the tensile stiffness and strength of the connection over the range of parameters tested. A too thin diagonal plate would fracture during loading, resulting in a significant reduction in the tensile capacity of the connection.
4. A formula for calculating the tensile yielding capacity of the diagonal–plate connection is presented. The calculation results of the formula were compared with the experimental and finite element results, and the results are in good agreement, which can predict the tensile yielding capacity of this type of connection.

## ACKNOWLEDGMENTS

The research in this paper was funded by the National Natural Science Foundation of China (No. 52378133) and the Chongqing Natural Science Foundation (No. 2023NSCQ–MSX3013). The authors wish to express their gratitude to the sponsors.

## REFERENCES

[1] Han L–H, Xu C–Y, Tao Z. Performance of concrete filled stainless steel tubular (CFSST) columns and joints: Summary of recent research. J Constr Steel Res 2019;152:117–31. https://doi.org/10.1016/j.jcsr.2018.02.038.

[2] Han L–H, Li W, Bjorhovde R. Developments and advanced applications of concrete–filled steel tubular (CFST) structures: Members. J Constr Steel Res 2014;100:211–28. https://doi.org/10.1016/j.jcsr.2014.04.016.

[3] CECS159–2004 Technical specification for structures with concrete–filled rectangular steel tube member. Beijing (China): China Planning Press; 2004 (in Chinese).

[4] GB50936–2014 Technical code for concrete filled steel tubular structures. Beijing (China): China Architecture and Building Press; 2014 (in Chinese).

[5] Nie J, Qin K, Cai CS. Seismic behavior of connections composed of CFSSTCs and steel–concrete composite beams — finite element analysis. J Constr Steel Res 2008;64:680–8. https://doi.org/10.1016/j.jcsr.2007.12.003.

[6] Nie J, Qin K, Cai CS. Seismic behavior of connections composed of CFSSTCs and steel–concrete composite beams — finite element analysis. J Constr Steel Res 2008;64:680–8. https://doi.org/10.1016/j.jcsr.2007.12.003.

[7] Qin Y, Chen Z, Yang Q, Shang K. Experimental seismic behavior of through–diaphragm connections to concrete–filled rectangular steel tubular columns. J Constr Steel Res 2014;93:32–43. https://doi.org/10.1016/j.jcsr.2013.10.020.

[8] Vulcu C, Stratan A, Ciutina A, Dubina D. Beam–to–CFT High–Strength Joints with External Diaphragm. I: Design and Experimental Validation. J Struct Eng 2017;143:04017001. https://doi.org/10.1061/(ASCE)ST.1943–541X.0001709.

[9] Nishiyama I, Fujimoto T, Fukumoto T, Yoshioka K. Inelastic Force–Deformation Response of Joint Shear Panels in Beam–Column Moment Connections to Concrete–Filled Tubes. J Struct Eng 2004;130:244–52. https://doi.org/10.1061/(ASCE)0733–9445(2004)130:2(244).

[10] Wang W–D, Han L–H, Uy B. Experimental behaviour of steel reduced beam section to concrete–filled circular hollow section column connections. J Constr Steel Res 2008;64:493–504. https://doi.org/10.1016/j.jcsr.2007.10.005.

[11] Zhou Z, Gan D, Zhou X. Cyclic–shear behavior of square thin–walled concrete–filled steel tubular columns with diagonal ribs. Eng Struct 2022;259:114177. https://doi.org/10.1016/j.engstruct.2022.114177.

[12] Wang L, Du W, He P, Yang M. Topology Optimization and 3D Printing of Three–Branch Joints in Treelike Structures. J Struct Eng 2020;146:04019167. https://doi.org/10.1061/(ASCE)ST.1943–541X.0002454.

[13] Li Y–L, Zhao X–L. Study on stainless steel blind bolted T–stub to concrete–filled stainless steel tube connections. Eng Struct 2022;257:114107. https://doi.org/10.1016/j.engstruct.2022.114107.

[14] Sun FF, Xue XY, Xiao Y, Le YM, Li GQ. Effect of welding and complex loads on the high–strength steel T–stub connection. J Constr Steel Res 2018;150:76–86. https://doi.org/10.1016/j.jcsr.2018.08.002.

[15] Wang Z–Y, Wang Q–Y, Xue H, Liu X. Low cycle fatigue response of bolted T–stub connections to HSS columns — Experimental study. J Constr Steel Res 2016;119:216–32. https://doi.org/10.1016/j.jcsr.2015.12.009.

[16] Park JW, Kang SM, Yang SC. Experimental Studies of Wide Flange Beam to Square Concrete–Filled Tube Column Joints with Stiffening Plates Around the Column. J Struct Eng 2005;131:1866–76. https://doi.org/10.1061/(ASCE)0733–9445(2005)131:12(1866).

[17] Yu Y, Lyu X, Tanaka K, Sasaki S. Experimental study on connection between concrete–filled square tube column and steel beams under tensile loading. Struct Eng 1999:23–8. https://doi.org/10.15935/j.cnki.jggcs.1999.01.005.

[18] Qin Y, Chen Z, Rong B. Component–based mechanical models for axially–loaded through–diaphragm connections to concrete–filled RHS columns. J Constr Steel Res 2014;102:150–63. https://doi.org/10.1016/j.jcsr.2014.06.016.

[19] Zhu W, Mo Z, Liu Y, Cui Y. Tensile behavior and load transfer mechanism of concrete–filled square steel tube exterior–diaphragm connections stiffened with PBL. Eng Struct 2021;231:111780. https://doi.org/10.1016/j.engstruct.2020.111780.

[20] Chen M, Zhao Y, Xie Y. Topology optimization and additive manufacturing of nodes in spatial structures. CHINA Civ Eng J 2019;52:1–10. https://doi.org/10.15951/j.tmgcxb.2019.02.001.

[21] Seifi H, Rezaee Javan A, Xu S, Zhao Y, Xie YM. Design optimization and additive manufacturing of nodes in gridshell structures. Eng Struct 2018;160:161–70. https://doi.org/10.1016/j.engstruct.2018.01.036.

[22] GB50081–2019 Standard for test methods of concrete physical and mechanical properties. Beijing (China): China Architecture and Building Press; 2019 (in Chinese).

[23] Yi S, Chen M–T, Young B. Design of concrete–filled cold–formed steel elliptical stub columns. Eng Struct 2023;276:115269. https://doi.org/10.1016/j.engstruct.2022.115269.

[24] Chen M–T, Zhang T, Young B. Behavior of concrete–filled cold–formed steel built–up section stub columns. Thin–Walled Struct 2023;187:110692. https://doi.org/10.1016/j.tws.2023.110692.

[25] Yi S, Chen M–T, Young B. Stub Column Behavior of Concrete–Filled Cold–Formed Steel Semi–Oval Sections. J Struct Eng U S 2023;149. https://doi.org/10.1061/JSENDH.STENG–11667.

[26] Zhang T, Chen M–T, Cai A, Cao H, Yun X, Zhao H, et al. Behaviour of high strength steel butt joints exposed to arctic low temperatures. Thin–Walled Struct 2023;192:111157. https://doi.org/10.1016/j.tws.2023.111157.

[27] Chen M–T, Cai A, Pandey M, Shen C, Zhang Y, Hu L. Mechanical properties of high strength steels and weld metals at arctic low temperatures. Thin–Walled Struct 2023;185:110543. https://doi.org/10.1016/j.tws.2023.110543.

[28] GB/T 228.1–2021 Metallic materials – Tensile testing – Part 1: Method of test at room temperature. Beijing (China): Standards Press of China; 2021 (in Chinese).

[29] Priestley MJN, Park R. Strength and Ductility of Concrete Bridge Columns Under Seismic Loading. Struct J 1987;84:61–76. https://doi.org/10.14359/2800.

[30] Nie J, Qin K, Cai CS. Seismic behavior of composite connections — flexural capacity analysis. J Constr Steel Res 2009;65:1112–20. https://doi.org/10.1016/j.jcsr.2008.12.003.

# SEISMIC ANALYSIS OF STEEL STAGGERED TRUSS FRAMING STRUCTURE WITH FLEXIBLE CONNECTION BETWEEN SLAB AND CHORD

*Li Yang[1], Gan Dan[2]*, Xuhong Zhou[3]*

[1] Mr., School of civil engineering, Chongqing university, 20174957@cqu.edu.cn.

[2] Prof., School of Civil Engineering and Geomatics, Southwest Petroleum University, gand03@qq.com.

[3] School of Civil Engineering, Chongqing University, zhouxuhong@126.com.

**Corresponding Author: Prof. Gan Dan.**

Southwest Petroleum University, Chengdu, China, 610500. **Email:** gand03@qq.com.

## ABSTRACT

Steel staggered truss framing (SSTF) structures, with high load-carrying capacity and good economic benefits, have been adopted in low intensity areas. The traditional seismic design of SSTF structure is that plastic hinges appear at chords at the end of the Vierendeel to realize the ductility of the structure. However, this requires a high cost to strengthen the rest of the member and repair after earthquake. The seismic force of SSTF structure is transferred to the foundation by slabs, shear connectors, and trusses sequentially floor by floor. The shear connector plays a key role in the shear path, and transfers lateral seismic force from truss to slab. Therefore, suitable designed shear connectors behave as both seismic isolation and energy dissipation. Therefore, two finite element (FE) models were established and verified: one with the weld element to simulate the rigid shear connector (RSSTF), and the other with the translator element to simulate the flexible shear connector (FSSTF) with appropriate plastic properties. The results of time-history analysis in five earthquakes proved that FSSTF has less seismic response and seismic design requirements. The damage to the truss during earthquakes has significantly decreased, and the stress level of the truss components has decreased by more than half. The floor shear force was more distributed to the columns, resulting in an 11.9% increase in stress at the end of the columns, which will be considered in the design.

***Keywords:*** *Steel staggered truss framing structure, flexible shear connector, seismic performance, finite element method, seismic time history analysis*.

# INTRODUCTION

Steel staggered truss framing (SSTF) structures are composed of slabs, trusses, columns, beams and the connections between them (Fig. 1), have been widely used in hotels and office buildings in low seismic areas [1]. The characteristic of SSTF structures lies in the horizontal direction, where the trusses with the same height as the floor are arranged staggered, and the lateral load-resisting system is formed with the slab and the shear connectors between them. This characteristic brings SSTF structures more flexible internal space, less material and foundation cost, larger lateral stiffness, and fast construction speed [2].

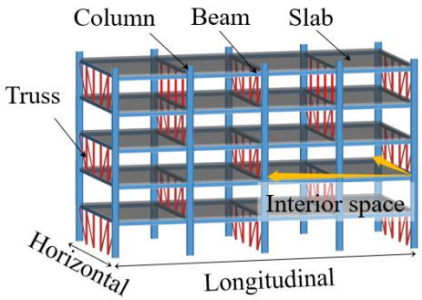


**Figure 1.** Steel staggered truss frame.

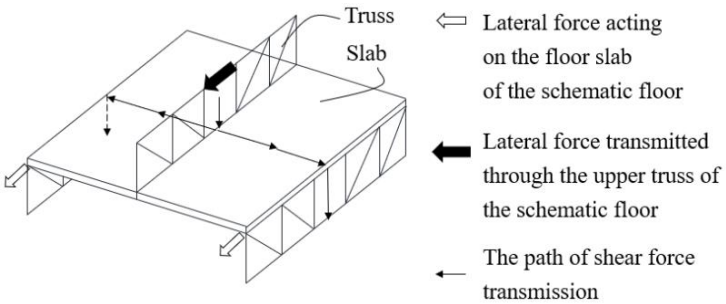


**Figure 2.** Shear force transfer path.

The horizontal shear force of each floor of a SSTF structure is mainly transferred to the foundation alternately by truss and floor slab[3] (Fig. 2). And because of that, the truss member is the key to earthquake resistance in SSTF structure. The test results in previous years indicated that SSTF structure has high bearing capacity and lateral stiffness, but poor ductility, deformation capacity and energy dissipation capacity[4]. The diagonal web member of the truss was prone to buckling, resulting in rapid stiffness degradation and poor seismic performance of the structure[5]. Therefore, efforts to improve the seismic performance of SSTF structures through design methods, structural measures, and energy dissipation components are important.

"Steel design guide series 14: staggered truss framing systems"[6] issued by AISC proposes that the chords at the end of the Vierendeel of the truss can be used as energy dissipation

members, and the rest of the members remain elastic. Chen et al.[7] also proposed the concept of ductile SSTF structure and corresponding energy-based plastic design method. Zhou et al.[8] also adopted the same design idea and design SSTF by magnifying the design requirements of elastic segment, and achieved satisfactory results.

However, the strengthening of the chord by the slab will significantly reduce the bending deformation of the chord at the end of the Vierendeel and prevent the formation of the expected failure mode mentioned above. On the one hand, the realization of the failure mode requires a high design cost, because scholars suggest enlarging the design requirements of protected components by 1.5-2 times[7][8], on the other hand, the chords and slabs rotate greatly, which is difficult to repair and will result in a decrease in the lateral and vertical bearing capacity of the structure.

Kim et al.[9] proposed a variety of structural schemes, such as adding internal columns, suspenders, oblique braces at the end of the story without trusses and buckling restrained braces. Simasathien et al.[10] proposed the use of multi-Vierendeel trusses, which improved the ductility of the structure to a certain extent. Yang[11] proposed a plastic design method for three-Vierendeel SSTF structure based on energy balance. The story drift of the designed three-Vierendeel SSTF structure was more uniform and the ductility was better. In addition, Y-shaped eccentrically web members[12] and the two-side connecting steel plate (TSCSP)[13] were also used to improve the seismic performance of SSTF structures (Fig. 3), but these measures have relatively complex construction details.

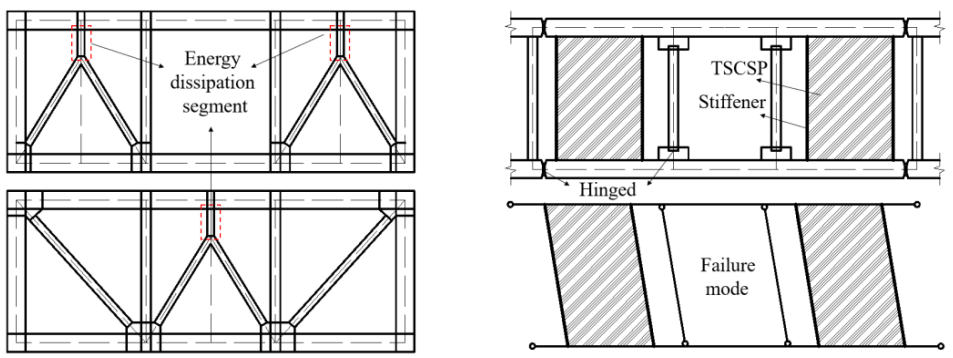


(a) Y-shaped eccentrically web members (b) two-side connecting steel plate

**Figure 3.** Structural measures.

Zhao et al.[14] and Kim et al.[15] adopted friction dampers at the diagonal web members and the chords at the end of the Vierendeel of the truss, respectively; Zhou et al.[16] adopted dampers with low yield point at the end of the web members adjacent to the Vierendeel, so that the structures showed a satisfactory damage controllable behaviour, but its lateral stiffness decreased. Liu[17] introduced the energy dissipation column[18] into SSTF structure, designed

the connecting rod to yielded and dissipated energy before the main structure. The energy dissipation column made the story drift more uniform.

Generally speaking, the above methods can effectively improve the seismic performance of SSTF structures and reduce the failure probability. However, there are still the following problems more or less: the expected yield model is difficult to achieve, the amount of steel used and the difficulty of construction may increase, the presupposition chord damage leads to a decrease in the vertical bearing capacity of the truss, and the difficulty of repairing after the earthquake increase.

In a SSTF structure, the shear connector between the slab and the chord plays two roles in the earthquake: transfer seismic energy from the truss to slab, and transfer the horizontal force from the slab to truss. Therefore, the shear connector could be endowed with the function of seismic isolation and energy dissipation. This would not only reduce the seismic action, but also participate in energy dissipation initially, thereby enhancing the seismic performance of SSTF structures. A suitable shear connector can prevent the formation of plastic hinges at the end of the chord, reduce the demand of deformation and energy dissipation of the main structure, and reduce the damage to structural and non-structural members caused by earthquakes.

In this work, two SSTF structures were analysed: one designed based on the code[19], and the other differing only in the use of a flexible connector. Through the verified finite element (FE) model, the seismic time history analysis of the two structures was conducted. The modal characteristics, acceleration response, displacement response, base shear, structural damage, and stress states of the two structures were compared in detail, which demonstrated the advantages of flexible connectors in SSTF structures. The lateral deformation mode and the transfer path of the lateral shear force of the SSTF structure with flexible shear connectors were analysed, which facilitates put forward the corresponding design method in subsequent research work.

# METHOD OF STRUCTURAL DESIGN AND ANALYSIS

## Structural design

An eight-story SSTF structure with fixed shear connectors between the slab and the chord (RSSTF) was designed according to the code[19], and its design conditions are shown in Table 1. The story height was 2.8 m, there were 5 trusses distributed longitudinally with a horizontal spacing of 6.6 m. The transverse hybrid truss consisted of five panels with a width of 2.4 m, including a middle Vierendeel (see Fig. 4b and c). The structural layout and the dimensions of the members were shown in Fig. 4 and Table 2, respectively. The structural steel was Q355 grade with a yield strength of 355 MPa; the thickness of the slab was 200 mm, using C30 grade concrete and HRB400 grade reinforcement [20].

On the basis of RSSTF, a SSTF structure with flexible connections (referred to as FSSTF) was designed, which allows the slab and the chord to move relative to each other along the direction of A to B axis shown in Fig. 4.

**Table 1.** Design Conditions.

| Design information | Values |
|---|---|
| Permanent load (Variable load) | 5kN/m$^2$ (2kN/m$^2$) |
| Site category | Class II |
| Ground roughness | Category B |
| Seismic intensity | 8 degrees (0.2 g) |
| Classification of design earthquake | Group 1 |

**Table 2.** Section of the members.

| Members | Sections | |
|---|---|---|
| Columns | H500×450×25×25 (F1-F4) | H450×400×25×25 (F5-F8) |
| Beams | H300×250×15×15 | |
| Chords | H180×180×10×10 (F0-F5) | H160×160×10×10 (F6-F8) |
| Oblique web members | F160×12 (F1-F5) | F140×12 (F6-F8) |
| Vertical web members | F160×10 (F1-F3) | F140×10 (F4-F5) F140×8 (F6-F8) |

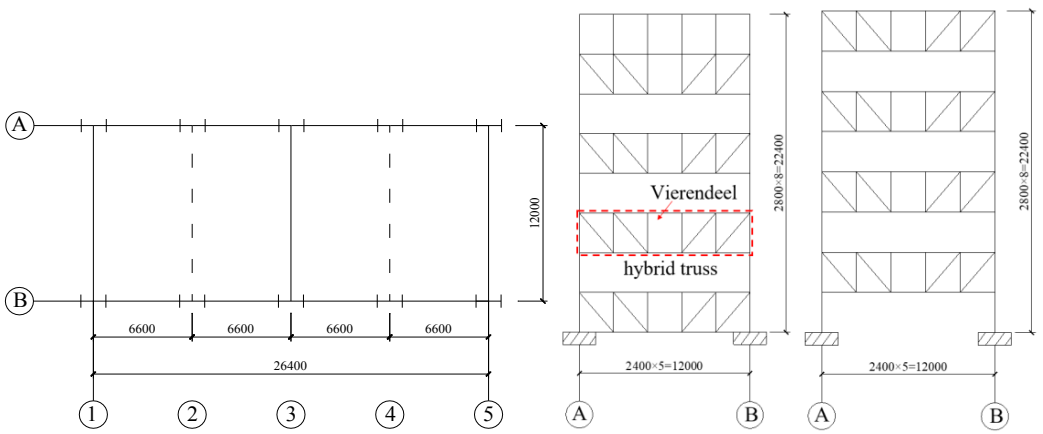


(a) Plane drawing (b) Elevation 1 (Axis 1, 3, 5) (c) Elevation 2 (Axis 2, 4)

**Figure 4.** Layout diagram of the structures. (mm)

## Establishment of nonlinear finite element model

In the model established by using ABAQUS [21], the structural plane consists of five staggered trusses, of which the first, third, and fifth are called odd trusses, and the second and fourth are called even trusses, as shown in the annotations Fig. 5. All degrees of freedom of the bottom end of the 10 columns were constrained. All the steel structural members were simulated by

line (beam) elements, which are divided into integral elements with 300 mm length, and different members were merge to simulate welding. The slab was simulated by a 7-layer composite shell element, as shown in Table 3.

**Table 3.** Parameters of composite shell.

| Layers | Materials | Thickness (mm) | Rotation (°) | Integral points |
|---|---|---|---|---|
| 1 | C30 | 20 | 0 | 3 |
| 2 | Reinforcement | 15 | 0 | 3 |
| 3 | Reinforcement | 15 | 90 | 3 |
| 4 | C30 | 100 | 0 | 3 |
| 5 | Reinforcement | 15 | 90 | 3 |
| 6 | Reinforcement | 15 | 0 | 3 |
| 7 | C30 | 20 | 0 | 3 |

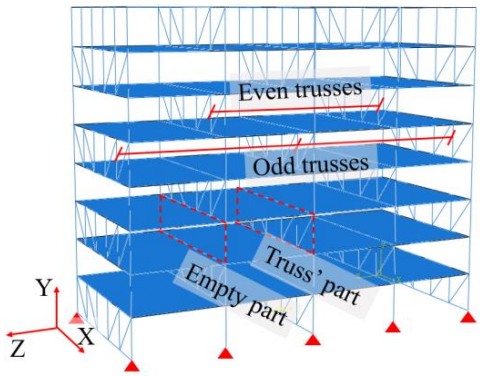


**Figure 5.** The FE model.

The materials in the model included concrete, steel and reinforcement. The stress-strain curve of concrete in compression is shown in Fig. 6(a). The elastic modulus, Poisson's ratio and density were taken as 20289.4 MPa, 0.2 and $2.5\times10^{-9}$ t/mm$^3$, respectively. The plastic damage parameters were listed in Table 4. The stress-strain curves of steel and reinforcement are shown in Fig. 6(b). Their elastic modulus, Poisson's ratio and density were taken as 206000 MPa, 0.3, and $7.85\times10^{-9}$ t/mm$^3$, respectively.

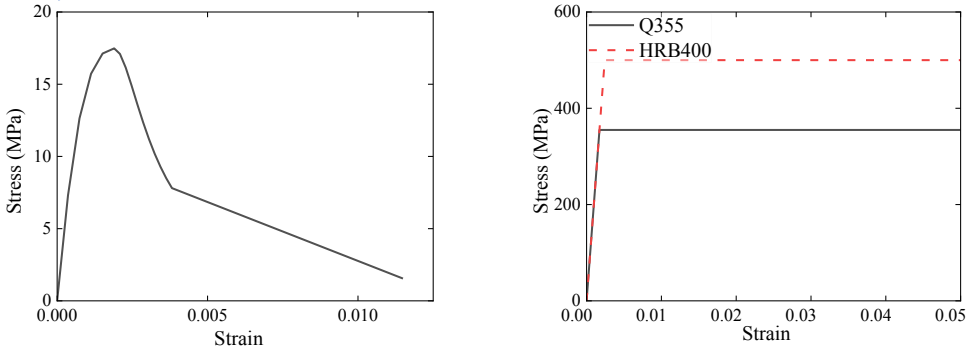


(a) Concrete (b) Steel and reinforcement

**Figure 6.** Stress-strain curves of materials

**Table 4.** Plastic damage parameters of concrete.

| Parameters | Values |
|---|---|
| $f_{bo}/f_c'$ | 1.16 |
| Flow potential eccentricity ($e$) | 0.1 |
| Dilation angle ($\psi$) | 30° |
| Compressive meridian ($K_c$) | 2/3 |
| Viscosity parameter | 0.0005 |

Eleven groups of connections were set between the slabs and chords on each floor, and were assigned different connection properties, i.e., weld element and translator element were adopted to simulate the rigid and flexible connections in the RSSTF model and the FSSTF model, respectively. The weld element, used in the RSSTF, constrains all degrees of freedom at both ends of the connecting pair, thus not allowing the two ends to move relative to each other in any direction.

Translator element was used in FSSTF as the flexible connection, which only allows both ends of the connecting pair to move in a specified way in one direction (that is, the truss direction) while completely constrains the remaining degrees of freedom. The prototype of the flexible connection between the slab and the chord is a metal shear connector specially designed based on the lateral yield bearing capacity of each layer of truss for the SSTF structure. Additionally, the translator element, whose free direction was not constrained at all, was also set between the slabs and the frame beams in order to prevent the beam from impeding the movement of the slab.

## Modal analysis

The modal information of the first five orders of RSSTF and FSSTF is summarized in Table 5. The two structures had no difference in frame direction (Z), their effective mass coefficients of

the first five orders in truss direction (X) were 0.98 and 0.94, respectively, both exceeding the minimum value (0.9) specified by the code[22].

**Table 5.** Modal information.

| Mode order | Period (s) | | Effective mass coefficient (%) | | | | | |
|---|---|---|---|---|---|---|---|---|
| | RSSTF | FSSTF | RSSTF | | | FSSTF | | |
| | | | X | Z | R | X | Z | R |
| 1 | 1.322 | 1.323 | 0.00 | 0.81 | 0.10 | 0.00 | 0.81 | 0.10 |
| 2 | 0.668 | 0.800 | 0.87 | 0.00 | 0.54 | 0.83 | 0.00 | 0.52 |
| 3 | 0.625 | 0.718 | 0.00 | 0.00 | 0.22 | 0.00 | 0.00 | 0.21 |
| 4 | 0.418 | 0.418 | 0.00 | 0.11 | 0.01 | 0.00 | 0.11 | 0.01 |
| 5 | 0.229 | 0.301 | 0.11 | 0.00 | 0.07 | 0.11 | 0.00 | 0.07 |
| Summation | | | 0.98 | 0.92 | 0.94 | 0.94 | 0.92 | 0.92 |

The ratio of the periodic value of the first-order torsion to the first order translation of the two structures was 0.47 and 0.54, respectively, both being less than the limit value of 0.9. FSSTF exhibited greater flexibility than RSSTF in truss direction, resulting in a 20% increase in the second natural vibration period. The reason is that the flexible connection makes the slabs lose the ability to coordinate the two adjacent trusses, and the upper and lower chords in a same floor no longer move in coordination with the slab.

## Selection of seismic wave and time history analysis

A total of five seismic waves were selected for time-history analysis of structures under rare earthquakes. The basic information is shown in Table 6, the response spectra compared with the designed response spectra are as shown in Fig.7. Before the time history analysis, the peak acceleration of each seismic wave was adjusted to 70cm/s$^2$ and 400cm/s$^2$ for different seismic conditions, and the modal analysis of the structure was carried out to obtain the natural frequency, and the Rayleigh damping coefficient was calculated and given to the material of the structure.

The results verified that the two structures showed a similar trend under the action of all of the five seismic waves, so this work took the analysis results of seismic wave KGS as an example.

**Table 6.** Basic information of seismic waves.

| Seismic waves | Duration (s) | Peak acceleration (mm/s$^2$) | Magnification factor |
|---|---|---|---|
| AOM | 31.02 | 51.4 | 13.62 (77.81) |
| HKD | 22.02 | 609.5 | 1.15 (6.56) |
| WITH | 23.02 | 97.1 | 7.21 (41.21) |
| KGS | 24.04 | 41.6 | 16.83 (96.21) |
| MYZ | 21.04 | 61.9 | 11.31 (64.58) |

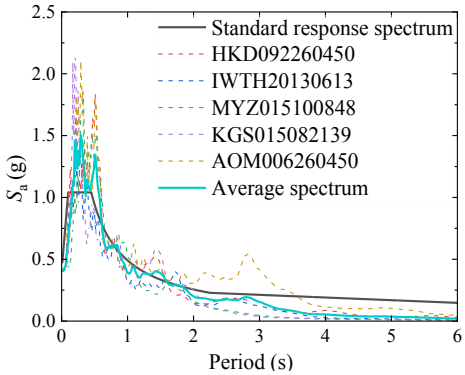


**Figure 7.** response spectrum of seismic waves.

# RESULTS OF TIME HISTORY ANALYSIS

## Acceleration response

The two seismic designed structures had no damage in frequent earthquakes (70cm/s$^2$). The sensation during the earthquake deserved attention. The slab and structural acceleration time-history curves of the top and fifth floors of the two structures were shown in Fig. 8. The data revealed that the slab acceleration of FSSTF was significantly lower than that of RSSTF, and the higher the floor was, the more obvious it was. The maximum acceleration of the slab in top floor and the fifth floor of FSSTF was 1006.8 mm/s$^2$ and 1220.8 mm/s$^2$ respectively, which was 60.3% and 26.0% less than that of RSSTF (the corresponding values were 2538.7 mm/s$^2$ and 1649.6 mm/s$^2$, respectively). This phenomenon indicates that the flexible connection between the slab and the chord can reduce the felt during the earthquake on the one hand and greatly reduce the inertia force of the slab on the other hand.

The acceleration of each slab of RSSTF was consistent with that of the structure of the corresponding floor. The acceleration of the structure of FSSTF was greater than that of the corresponding slab, but the acceleration of the structure did not determine the damage degree of the structure, so it would not cause harm to the structure.

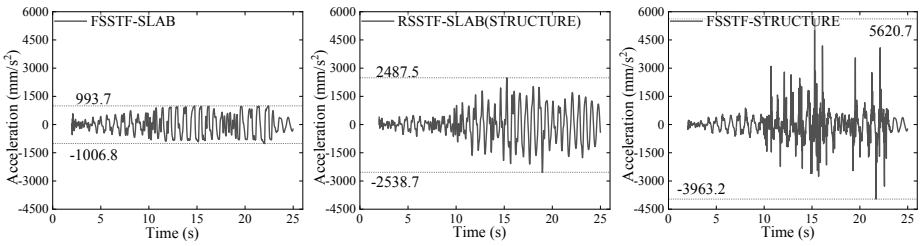


Top floor

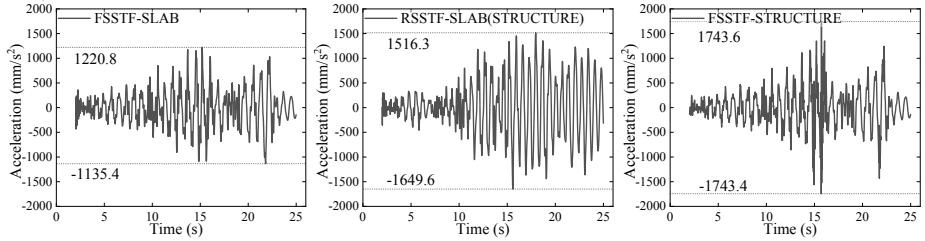


The fifth floor

**Figure 8.** Acceleration response.

## Displacement response

The story drift of FSSTF in the empty part was larger than that of RSSTF, but smaller in the truss part (Fig. 9(a)). The reason is that the two parts of FSSTF cannot coordinate to resist the lateral force, resulting in a low overall lateral stiffness. This phenomenon depends on the distribution of the shear force of the empty part and truss part in the structure, i.e., based on the stiffness of both. The stiffness ratio of the empty part to truss' part of RSSTF remains unchanged until the structure enters plasticity, while the flexible shear connectors of FSSTF enters the plasticity in advance due to a large force, which leads to a great decrease in the stiffness of the shear path of the truss part, and finally increases the shear force and deformation of the empty part.

However, on the whole, the displacement of FSSTF with flexible connections was smaller than that of RSSTF (Fig. 9(b)). The maximum top displacement of FSSTF was 82.5 mm, which was 24.6% less than that of RSSTF (109.4 mm). This effect will predictably reduce structural damage effectively.

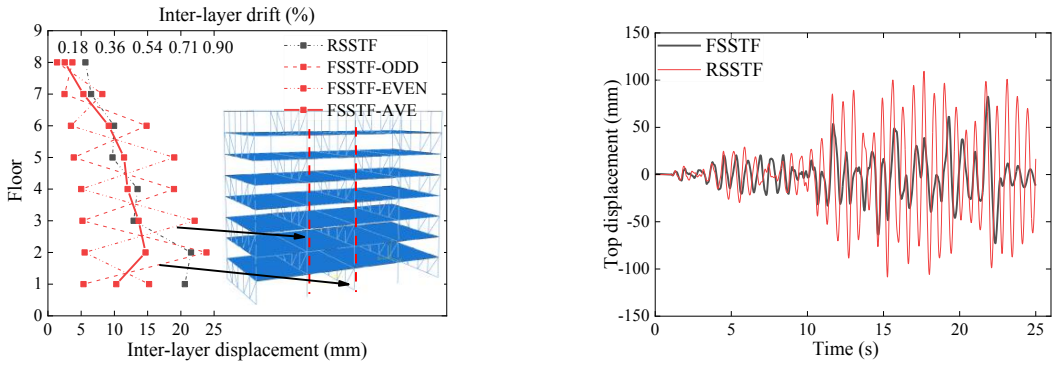


(a) Inter-layer displacement

(b) Top displacement

**Figure 9.** Displacement time history curves.

## Lateral deformation of structure

RSSTF showed the lateral deformation mode of the traditional SSTF, that is, each floor presented an overall deformation along with the slab in the X direction (Fig. 10(a)). However, in structure-FSSTF, the lateral deformation of the empty part of each floor was larger than that of the truss part (That's why the interlayer displacement shown in Fig. 9(a) appears.), showing the lateral deformation shown in Fig. 10(b).

Based on the above results and reasons, the demand for lateral resistance of trusses of FSSTF decreased while the demand for moment-bearing capacity of column ends increased. In addition, the frame beam ends exhibited a bending moment around the vertical axis (Y) with the lateral deformation of the structure (see the beams in F5 and F6 in Fig. 10(b)), which should be paid attention to in design.

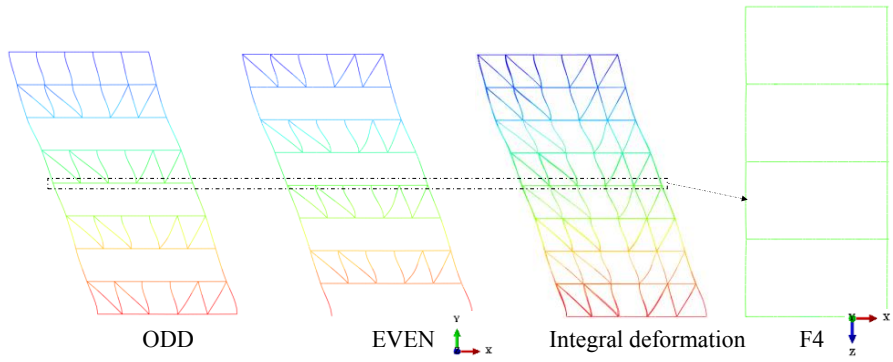


(a) RSSTF

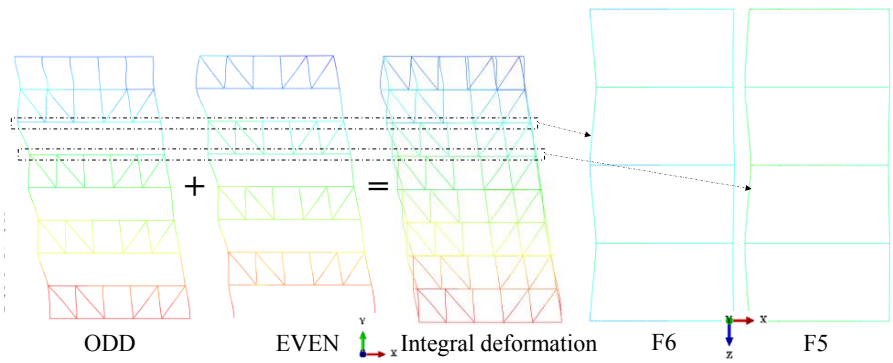


(b) FSSTF

**Figure 10.** Overall deformation mode of structures.

## Base shear

The base shear time history curves of the two structures in frequent and rare earthquakes were extracted as shown in Fig. 11. The maximum base shear of FSSTF were 1947.8 kN and 5161.4 kN, which were 33.2% and 63.8% lower than those of RSSTF (corresponding values of 2914.5

kN and 14256.5 kN, respectively). The flexible connection in FSSTF played a role of isolation bearing and reduced the energy transfer from the truss to the slab, so the seismic action was significantly reduced, which also means that the seismic demand of the members was reduced.

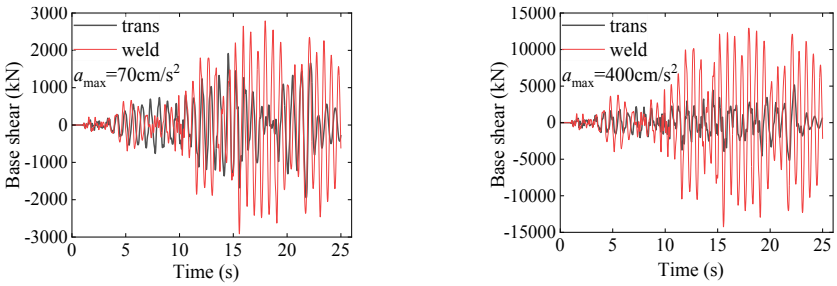


**Figure 11.** Time history curves of base shear.

## Structural damage and stress

In rare earthquakes, some damage and local plasticity of the structure are allowed, so as to prevent collapse or other brittle failures. The bottom of the columns of RSSTF and the diagonal web members of the lower truss yielded, which indicating the seismic demand of the structure depends on the trusses; while the position of the maximum stress of FSSTF shifted from the trusses member to the column ends, and no member yielded, which showed the advantage of flexible connections in the seismic resistance of SSTF structure (see Fig. 12).

The von Mises stress time history curve of the representative web member and column (the marked member in Fig. 12) is shown in Fig. 13. It can be found that the stress of the truss member in FSSTF was exceedingly small (the maximum value was about 200 MPa, half of the maximum value of RSSTF in the same position), but the stress of the column was somewhat larger (the maximum value was 347 MPa, less than yield strength, and 11.9% larger than that of 310 MPa in the same position of RSSTF). Such a stress situation was consistent with the overall deformation mode of the structure. Therefore, the redundancy of the columns should be considered in the design, but the cross-section of the truss member can be greatly reduced.

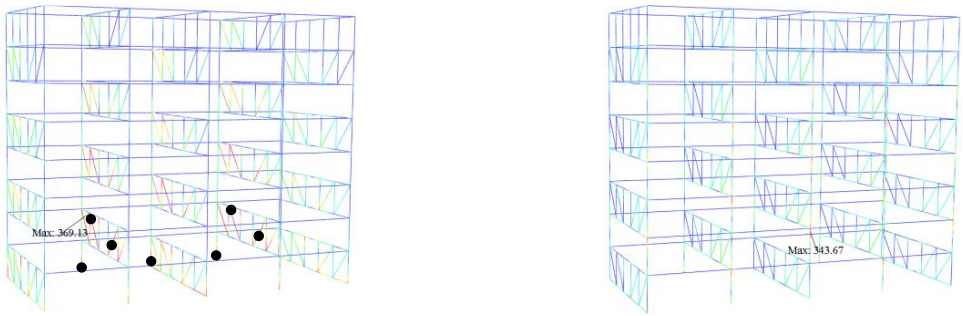


(a) RSSTF (b) FSSTF

**Figure 12.** Damage of two structures.

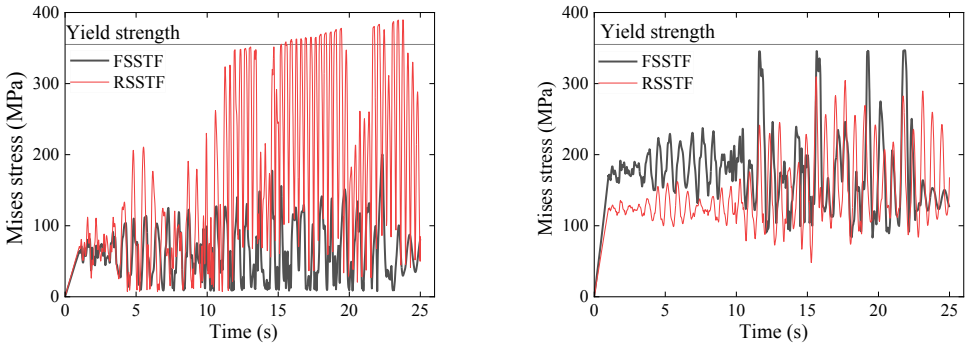


(a) Oblique web members (b) Columns

**Figure 13.** Stress time history curves of members.

# CONCLUSIONS

The seismic time history analysis of a traditional SSTF structure (RSSTF) and a SSTF structure with flexible connection between slab and chord (FSSTF) was conducted. The advantages and characteristics of FSSTF in earthquake resistance were evident, which were summarized as follows:

1. In frequent earthquakes, intensity of the felt during the earthquake is a factor of concern, which is determined by the acceleration of the slab. The slab acceleration of FSSTF was much smaller than that of RSSTF under the same conditions (Top floor: 1006.8 mm/s$^2$ vs 2538.7 mm/s$^2$, fifth floor: 1220.8 mm/s$^2$ vs 1649.6 mm/s$^2$), which undoubtedly results in a slighter shock.

2. The flexible shear connectors made the structure appear a unique lateral deformation mode: the empty part and the truss part in a same floor were not deformed due to the cooperation of the slab, but independently. As a result, the demand of the structure for the truss was obviously reduced, but the bending moment at the end of the column and the bending moment at the end of the beam around the vertical axis should be taken into account in the design.

3. The top displacement and base shear and other seismic responses of FSSTF were significantly lower than those of RSSTF (Top displacement: 82.5 mm vs 109.4 mm, Base shear: 5161.4 kN vs 14256.5 kN). These improvements mean the reduction of structural damage and the improvement of seismic performance. The structural members of FSSTF did not yield in rare earthquakes, while the plastic hinges appeared in many truss web members of RSSTF under the same design conditions.

## ACKNOWLEDGMENTS

Funding: This study has been supported by research grants from the National Natural Science Foundation of China (No. 52378133). The authors wish to express their gratitude to the sponsor.

## REFERENCES

[1] Gan Dan, Zhou Xuhong, Zhou Qishi. A Review on the Seismic Behavior of Steel Staggered Truss Framing System[J]. Progress in Steel Building Structures, 2019, 21(04): 1-10. (In Chinese)

[2] Hansen R J, LeMessurier W J, Paul P J. New Steel Framing System Promises Major Savings in High-Rise Apartments[J]. Architecture Record, 1966, 139(6): 191-196.

[3] Zhou Xuhong, Mo Tao, Liu Yongjian, et al. Experimental study on high-rise staggered truss steel structure[J]. Journal of Building Structures, 2006(5): 86-92. (In Chinese)

[4] Ran Hongdong, Su Mingzhou, Hu Tianbing, et al. An experimental study on the hysteretic behavior of composite steel staggered truss structures under cyclic load[J]. China Civil Engineering Journal, 2009, 42(11): 55-63. (In Chinese)

[5] Zhao Baocheng, Gu Qiang, He Ruoquan, et al. Horizontal bearing capacity test of Steel staggered truss frame structure with concrete-filled Steel Tubular columns[J]. Journal of Shenyang Jianzhu University (Natural Science), 2010, 26(1): 13-19. (In Chinese)

[6] AISC. Steel design guide series 14：staggered truss framing systems［M］. Chicago：American Institute of Steel Construction, 2003: 15-24.

[7] Chen Xiangrong, Zong Zhifang, Ran Hongdong. Plastic design of special staggered truss based on energy balance[J]. Earthquake Engineering and Engineering Dynamics, 2015, 35(4): 236-243. (In Chinese)

[8] Zhou Xuhong, Zhou Zhibin, Zhou Qishi, et al. Study on Seismic Design Method of Steel Staggered Truss Framing Systems[J]. Journal of Hunan University (Natural Sciences), 2022, 49(01): 1-11. (In Chinese)

[9] Kim J, Lee J, Kim B. Seismic retrofit schemes for staggered truss structures[J]. Engineering Structures, 2015, 102: 93-107.

[10] Simasathien S, Chao S H, Moore K, et al. Modified structural layouts for Staggered Truss Framing systems used in seismically active areas[J]. NCEE 2014-10th U.S. National Conference on Earthquake Engineering: Frontiers of Earthquake Engineering, 2014.

[11] Yang Zhiqiang. Research on Plastic Design Method and Seismic Performance Evaluation of Staggered Truss Steel Framing Structure Based on Energy Balance[D]. Chongqing University, 2021. (In Chinese)

[12] Zhao Baocheng, Zhou Dehao, Gu Qiang, Yu Anlin. Experimental study on hysteretic behavior of eccentrically web members staggered truss[J]. Engineering Mechanics, 2013, 30(12):71-77. (In Chinese)

[13] Gan Dan, Liu Tao, Yao Yushan, Zhou Xuhong. Study on Plastic Design Method of Staggered Truss Structure with Two-Side Connecting Steel Plates[J]. Steel Construction (Chinese & English), 2020, 35(11): 1-24.

[14] Zhao Baocheng, Ji Mingming, Gu Qiang, He Ruoquan. Experimental Investigation of Hysteretic Behavior of Passive Energy Dissipation Staggered Truss[J]. Journal of Shenyang Jianzhu University (Natural Science), 2013, 29(01):7-15. (In Chinese)

[15] Kim J, Kim S. Performance-based seismic design of staggered truss frames with friction dampers[J]. Thin-Walled Structures, 2017, 111: 197-209.

[16] Zhou X, Chen Y, Ke K, et al. Hybrid steel staggered truss frame (SSTF): A probabilistic spectral energy modification coefficient surface model for damage-control evaluation and performance insights[J]. Journal of Building Engineering, 2022, 45: 103556.

[17] Liu Tao. Finite element analysis of seismic performance of energy dissipation column-staggered truss steel framing structure[D]. Chongqing University, 2021. (In Chinese)

[18] Li Yanwen, Li Guoqiang. Mechanism and application of dual energy-dissipative rocking columns in RC frames for seismic mitigation[J]. Journal of Building Structures, 2021, 42(12): 65-75. (In Chinese)

[19] JGJT 329-2015, Specification for design of staggered steel truss framing systems[S]. Beijing: China Architecture Publishing & Media Co., Ltd, 2015.

[20] GB50010-2010, Code for design of concrete structures[S]. Beijing: China Architecture Publishing & Media Co., Ltd, 2015.

[21] V. Abaqus, 6.14-1. Abaqus/standard user's manual and Abaqus CAE manual, Providence, RI, USA: Dassault Systemes Simulia Corp. (2014).

[22] GB50011-2010, Code for seismic design of buildings[S]. Beijing: China Architecture Publishing & Media Co., Ltd, 2016.

# Enhancing the Damage Resistance of High-Strength Concrete under Penetration by an Optimized Layered-Structure Concept

*Y.Y.Y. Cao[1], Dianyi Song[2], Yimin Huang[3] and Song Li[4]*

[1] Doctor, Undergraduate School, National University of Defense Technology, cy3yeah@163.com.

[2] Associate professor, Undergraduate School, National University of Defense Technology, 149070703@qq.com.

[3] Associate professor, Undergraduate School, National University of Defense Technology, 13397481418@189.cn.

[4] Master, Undergraduate School, National University of Defense Technology, 331213462@qq.com.

**Corresponding Author: Dianyi Song, PhD.**

No.1 Fuyuan Road, Changsha, Hunan, China, 410072

**Email:** 149070703@qq.com

## ABSTRACT

The study aims to improve the damage resistance of high-strength concrete (HSC) under penetration by applying the multilayer concept. The designed layered HSC consists of three layers, i.e., crack-resistant layers at the top and bottom of the sample (concentrating steel fibers), and a penetration-resistant layer in the middle (containing coarse basalt aggregates). A series of penetration experiments were carried out and influencing factors such as aggregate size and fiber shape were discussed. The study reveals that the designed layered HSC provides superior damage resistance compared to the single-layered reference HSC, with a 66% reduction in the crater diameter and a crater volume about 13% of that of the reference group. The improved damage resistance of the layered HSC is associated with the synergistic effect of the aggregate size and the fibers shape. It is exhibited that straight fibers produce smaller crater sizes when the penetration-resistant layer consists of smaller aggregates, i.e., 10 mm to 30 mm; conversely, hooked-end fibers produce better damage resistance when the aggregate size is between 50 mm and 80 mm. The results of this study contribute to the understanding of the ballistic properties of layered HSC, and promote its application in protective structures.

***Keywords:*** *High-strength Concrete, Layered-structure Concept, Preplaced, Steel Fiber, Coarse Aggregate, Penetration Impact.*

# INTRODUCTION

Improving the performance of structures under impact load is important for ensuring the safety of people and reducing casualties caused by violent conflicts or terrorist attacks, especially for buildings such as nuclear power plants, government buildings and protective constructions. The study of structural impact resistance is also a reflection of the continuous progress and development of engineering technology, which promotes the application of new materials, technologies and design concepts. Concrete is the most commonly used building material, but its brittle damage pattern seriously affects the impact resistance of the structure, and the spalling of concrete on the back side of the impacted structure can cause secondary injuries to people inside the building [1]. The addition of steel fibers helps to improve the toughness of concrete and changes the damage pattern from brittle to ductile [2,3]. Due to the relatively high carbon emission of steel fiber and cement in their production processes, for massive concrete structures, the reasonable reduction of cement dosage and effective utilization of steel fiber are of great practical significance for energy saving, emission reduction and sustainable development.

An innovative approach to achieve this goal is designing concrete target with a layered-structure concept, i.e., producing multi-layered prepacked aggregate fibrous concrete (MLPAFC) [4]. MLPAFC is manufactured by prepacking coarse aggregates and fibers in multilayers and then injecting cement slurry to fill the voids. With this special casting method, the proportion of aggregates in MLPAFC is typically much higher than that in conventional single-layered concrete, and therefore, much less cement is required in MLPAFC. Moreover, fibers can be prepacked in relatively concentrated areas where they really need, which helps to maximize fiber utilization. In addition to the benefits of being more material efficient, MLPAFC also has the potential to provide a better impact resistance. For example, Murali and Ramprasad [5] produced a MLPAFC and their study shows that this three-layered specimen has a superior impact strength under falling weight collision. A similar research is done by Ramkumar et al., [6] which further confirms the advantage of MLPAFC under impact. It is worth noting that in the above studies, the coarse aggregate and the steel fibers are pre-mixed together and then prepacked in the molds, i.e., fibers are incorporated throughout the specimen while the types of fibers are different in each layer. However, consider the failure mode of concrete under impact, especially under ballistic penetration (see Figure 1 [7]), the distribution of steel fibers can be further improved to achieve a better fiber utilization [8].

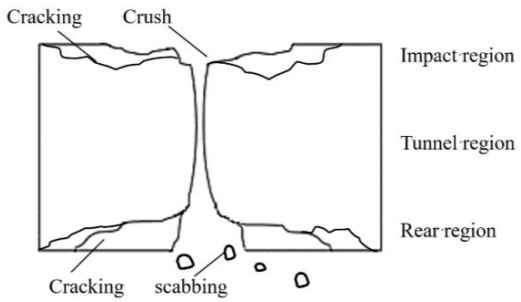


**Figure 1.** Illustration of a concrete target under penetration [7].

In this study, high-strength concrete (HSC) protective element is developed by an optimized layered-structure concept to enhance its damage resistance under ballistic impact. The protective element has three layers: the top and bottom layers are designed to resist cracking under penetration, while the middle layer utilizes the high strength of coarse aggregates to stop the bullet. Therefore, steel fibers are preplaced at the top and bottom of the mold (crack-resistant layers), whereas the middle is filled with a large amount of coarse basalt aggregates (penetration-resistant layer). These three layers are combined together by injecting HSC slurry to form an integral protective element. The damage of the designed protective element under penetration is evaluated and compared with conventional single-layered HSC. The layered HSC protective element proposed in this study contributes to the sustainable development of cementitious materials and deepens the understanding of impact resistance of layered structures.

# EXPERIMENTAL METHODS

## Materials and mix design

Table 1 lists the raw materials of the HSC slurry, including CEM I 52.5 R cement, micro silica, limestone powder, very fine sand, PCE superplasticizer and tap water, and their amounts are also listed in the table. Coarse basalt aggregates of three diameter groups are considered, namely 10-30 mm, 30-50 mm and 50-80 mm. Straight steel fiber and hooked-end fiber are used in the protective element, as shown in Figure 2. The diameter and length of the straight fiber are 0.2 mm and 13 mm, respectively, while those of the hooked-end fiber are approximately 0.22 mm and 14 mm. The tensile strengths of the two types of fibers are more than 2300 MPa.

**Table 1.** HSC slurry composition

| Cement [kg/m$^3$] | Micro silica [kg/m$^3$] | Limestone powder [kg/m$^3$] | Sand [kg/m$^3$] | Superplasticizer [kg/m$^3$] | Water [kg/m$^3$] |
|---|---|---|---|---|---|
| 900 | 60 | 240 | 780 | 23 | 276 |

(a) Straight fiber (b) Hooked-end fiber

**Figure 2.** Steel fibers.

## Design of the layered protective elements

The designed layered protective elements are listed in Table 2, in which No.1-7 are the three-layered specimens and No. 8-9 are single-layered ones. In the identification, the letters T and O indicate that the sample has three layers or one layer, respectively. The letters S and H represent the straight steel fiber and the hooked-end fiber, respectively. The numbers following the letters T and O indicate the aggregate size range (in mm), and those following S and H give the volume fractions of the straight and hooked-end fibers, respectively. For example, T13-S1H1 is a three-layered protective element with 10-30 mm basalt aggregates in the middle layer and a mixture of 1% straight fibers and 1% hooked-end fibers in both the top and bottom layers.

**Table 2.** Design of layered protective elements

| No. | Identification | Variables | | |
|---|---|---|---|---|
| | | Aggregate size [mm] | Straight steel fiber [%] | Hooked-end steel fiber [%] |
| 1 | T13-S2 | 10-30 | 2 | 0 |
| 2 | T35-S2 | 30-50 | 2 | 0 |
| 3 | T58-S2 | 50-80 | 2 | 0 |
| 4 | T13-S1H1 | 10-30 | 1 | 1 |
| 5 | T13-H2 | 10-30 | 0 | 2 |
| 6 | T58-S1H1 | 50-80 | 1 | 1 |
| 7 | T58-H2 | 50-80 | 0 | 2 |
| 8 | O13-S2 | 10-30 | 2 | 0 |
| 9 | O35-S2 | 30-50 | 2 | 0 |

## Casting procedure

The steel mold used to cast the protective element has a length of 400 mm, a height of 300 mm and a tube thickness of 5.5 mm. The casting procedure of the three-layered samples generally includes three main stages. (1) Materials are preplaced in the mold in the designed amounts in the order of steel fibers, coarse aggregates and steel fibers. (2) HSC slurry is mixed as follows: mix all powders and fine sand for around 3 minutes; add 70% water and mix for approximately 2 minutes; add the superplasticizer and the remaining water and mix for an additional 3 minutes. (3) A funnel is used to inject the HSC slurry into the mold so that it gradually submerges the fibers and aggregates from the bottom of the specimen upwards (see Figure 3). This casting method provides a denser structure and avoids the problem of possible honeycomb voids inside the protective element, in comparison to pouring the HSC slurry directly from the top of the sample downwards to the bottom by gravity effect [9]. In the designed three-layered sample, the thickness of the crack-resistant layers at the top and bottom is around 30 mm to 35 mm, depending on the type of steel fibers and their random distribution. Correspondingly, the

thickness of the penetration-resistant layer in the middle of the sample is about 230 mm to 240 mm. Two samples are casted for the ballistic experiments in each group. The compressive and tensile strengths of the designed protective elements are also casted using 150 mm cubes, as shown in Figure 4. Moreover, cubes of the HSC slurry are also casted in order to evaluate the strengths of the substrate. For the compressive and tensile experiments, three samples are casted in each group.

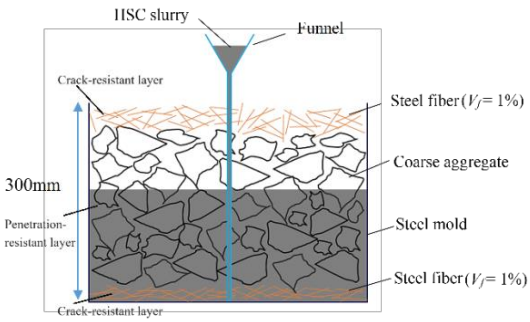


**Figure 3.** Illustration of the casting procedure.

**Figure 4.** Cube casting procedure.

## Testing methods

The compressive and tensile strengths of the designed protective elements as well as the HSC slurry are tested with a universal testing machine according to GB/ T 50081- 2002. For the penetration tests, 7.62 mm projectile is utilized and the impact velocity is around 820 m/s. The protective element is fixed by a steel frame to prevent its movement under the ballistic impact. More information about the test setup can be found in [10]. Damage of the protective element is measured after the test, including the equivalent diameter $D_{eq}$, height $H_c$ and volume $V_c$ of the impact crater and the total penetration depth $P$, as illustrated in Figure 5. The equivalent diameter $D_{eq} = \sqrt{D_1 D_2}$. The volume of the crater is measured by filling the crater with sand and calculating the amount of sand used.

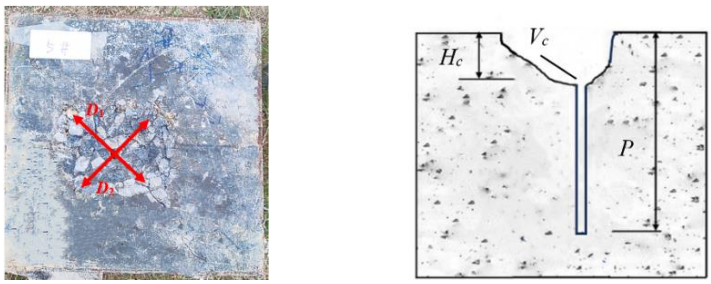


(a) Top view (b) Section view

**Figure 5.** Diagram of damage parameters

# RESULTS AND DISCUSSIONS

## Compressive and tensile strengths

The 28d compressive and tensile strengths are given in Table 3, which are the averaged values of three samples in each group. It can be obtained from the table that the tensile strengths of both the three-layered and one-layered cubes are higher than that of the HSC slurry thanks to the addition of steel fibers. Moreover, the particle size of the coarse aggregate has almost no effect on the tensile strength of the three-layered cube, while the strength of the one-layered cube deceases with the increase of the aggregate size. This is due to the fact that the fibers and aggregates are mixed together in the one-layered cube, and the relatively large aggregate size affects the homogeneous distribution of the fibers, therefore, the tensile strength is weakened.

**Table 3.** Compressive and tension strengths

| No. | Identification | Variables | |
|---|---|---|---|
| | | Compressive strength [MPa] | Tensile strength [MPa] |
| 1 | T13-S2 | 80.9 | 8.6 |
| 2 | T35-S2 | 85.8 | 8.2 |
| 3 | T58-S2 | 87.5 | 8.3 |
| 4 | T13-S1H1 | 85.7 | 11.5 |
| 5 | T13-H2 | 81.1 | 10.1 |
| 6 | T58-S1H1 | 81.4 | 8.5 |
| 7 | T58-H2 | 78.7 | 9.5 |
| 8 | O13-S2 | 87.0 | 11.1 |
| 9 | O35-S2 | 84.6 | 8.8 |
| 10 | HSC slurry | 91.3 | 6.4 |

In addition, the compressive strengths of the three-layered cubes are smaller than that of the HSC slurry, which is consistent with the conclusion in [11]. This is because the three-layered cubes consist mainly of coarse basalt aggregates and steel fibers, leaving only a few of voids to be filled with the HSC slurry. When the three-layered cube is under compression, the stresses are transferred though the fiber layer to the HSC and then to the aggregates, causing the aggregate to detach the HSC grout [11]. Consequently, the compressive strength of the three-layered cube depends mainly on the bond between the aggregate and the HSC grout, which is usually weaker than the material strength of the HSC itself due to the higher porosity of the aggregate-HSC interfacial transition zone. Furthermore, larger aggregates are found to increase the compressive strength of the three-layered cube. This may be attributed to the larger contact area between the larger aggregate and the HSC, which enhances the adhesion between them and hence improves the compressive strength.

## Damage after penetration

The equivalent diameter $D_{eq}$, height $H_c$ and volume $V_c$ of the crater and the total penetration depth $P$ are given in Figure 6, which are the average results of two specimens in each group. It can be obtained from the figure that the three-layered protective element T58-S2 achieves the smallest penetration depth, followed by the one-layered sample O13-S2, thanks to their relatively high compressive strengths. However, compared to the damage level of the impact crater, namely $D_{eq}$, $H_c$ and $V_c$, the penetration depth $P$ of all tested protective elements have no significant difference and the value of $P$ is more dependent on the compressive strength of the specimen rather than the layered-structure.

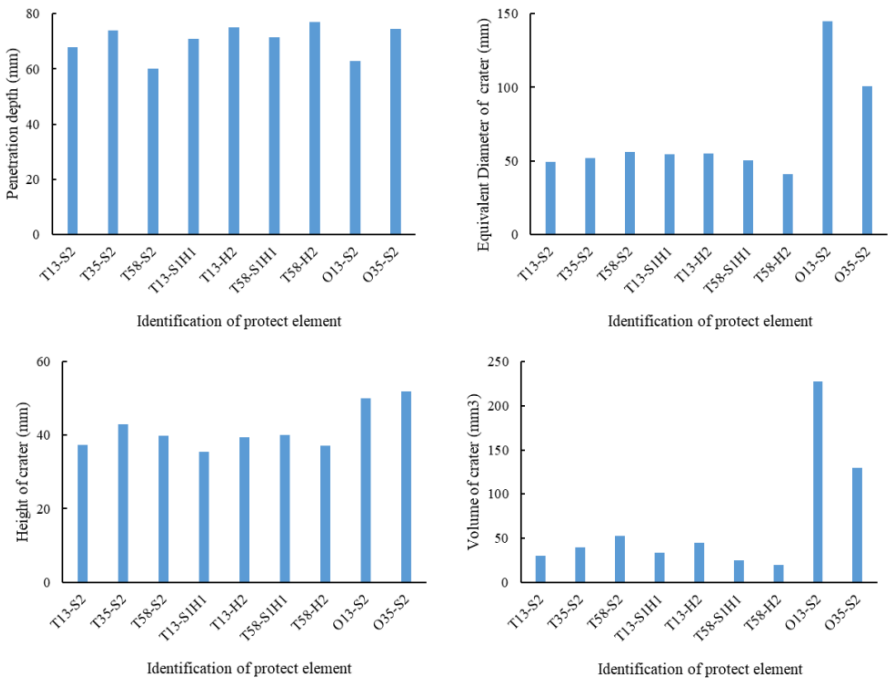


**Figure 6.** Damage parameters

In contrast, the crater dimensions are remarkably different between the three-layered and one-layered protective elements. The layered-structure, in particular, contributes to obvious reductions of the equivalent diameter $D_{eq}$ and the volume of crater $V_c$. To specify, $D_{eq}$ and $V_c$ of group T35-S2 are around 52.1 mm and 40 mm$^3$, respectively, while those of group O35-S2 are approximately 100.8 mm and130.0 mm$^3$. Comparisons between groups T13-S2 and O13-S2 further confirm the effectiveness of applying the layered-structure concept to reduce $D_{eq}$ and $V_c$, with T13-S2 showing a 66% reduction in the crater diameter and a crater volume approximately 13% of that of O13-S2 (see Figure 7). The improved damage resistance of the layered protective element is associated with the synergistic effect of the aggregate size and the fibers shape.

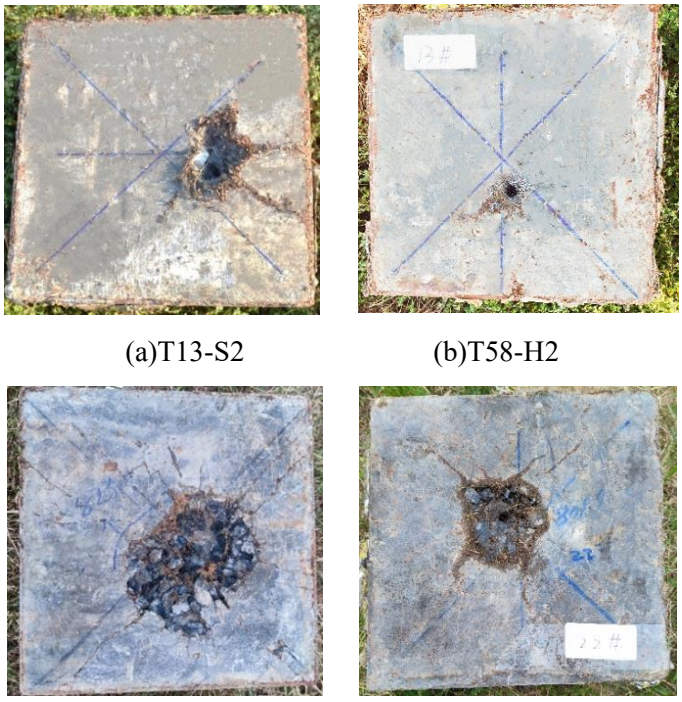

(a)T13-S2 (b)T58-H2

(c)O13-S2 (d)O35-S2

**Figure 7.** Damage after penetration

Moreover, it is exhibited that when the penetration-resistant layer consists of smaller aggregates, namely 10 mm to 30 mm, using the straight fibers in the crack-resistant layer benefits the reduction of the crater size. For example, $D_{eq}$ and $V_c$ of group T13-S2 are around 11% and 33% smaller than those of T13-H2. Conversely, when the aggregate size is 50-80 mm, the hooked-end fibers produce better resistance with respect to the impact crater dimensions. The crater volumes of groups T58-S2, T58-S1H1 and T58-H2 are 52.5 mm$^3$, 25 mm$^3$ and 20 mm$^3$, respectively, and the equivalent diameters are around 56.2 mm, 50.3 mm and 40.9 mm, suggesting that increasing the proportion of the hooked-end fibers contributes to an obvious

reduction in the crater size. This different optimum fiber shapes suitable for different aggregate sizes may be caused by the reflection of impact waves in the protective elements. When the coarse aggregates are relatively large, more waves are reflected from the penetration-resistant layer to the crack-resistant layer, and since the hooked-end fibers are more difficult to pull out from the HSC grout, they can better resist the effects of the reflected waves and provide better damage resistance. On the other hand, when the aggregates are relatively small, the intensity of the reflected wave is also smaller, and the straight fibers are sufficient to resist the waves. In this case, under a certain fiber volume, the use of straight fibers in the crack-resistant layer yields a greater number of fibers than the use of hook-ended fibers, and therefore the straight fibers result in smaller crater sizes under ballistic impacts.

# CONCLUSIONS

In the present study, three-layered HSC protective elements containing coarse basalt aggregates and steel fibers are developed using a prepackaged casting method. The mechanical properties and ballistic performances of the protective elements are evaluated experimentally. Some specific conclusions can be drawn from the study:

(1) The compressive strength of the three-layered HSC is smaller than that of the HSC slurry because it depends mainly on the aggregate-HSC bond, which is weaker than the HSC material strength due to the higher porosity of the aggregate-HSC interfacial transition zone.
(2) For the three-layered HSC, the use of larger aggregates increases the compressive strength thanks to the larger contact area between the aggregates and the HSC grout, which enhances the adhesion between them.
(3) The layered-structure contributes to obvious reductions of the equivalent diameter and volume of the impact crater. However, the penetration depth is more dependent on the compressive strength of the protective element rather than the layered-structure.
(4) The suitable fiber shape varies with the size of the aggregate, which is mainly related to the reflection of impact waves inside the protective element. The straight fibers results in smaller crater sizes when the penetration-resistant layer consists of 10-30 mm aggregates. In contrast, when the aggregate size is 50-80 mm, the hooked-end fibers are preferred.

## ACKNOWLEDGMENTS

The financial supports from the National Natural Science Foundation of China (No. 52208297) and the Scientific Research Project of National University of Defense Technology (No. ZK21-50) are acknowledged.

# REFERENCES

[1] R. Yu, Development of sustainable protective Ultra-High Performance Fibre Reinforced Concrete (UHPFRC), Eindhoven University of Technology, 2015.

[2] Y.Y.Y. Cao, Q.L. Yu, Effect of inclination angle on hooked end steel fiber pullout behavior in ultra-high performance concrete, Compos. Struct. 201 (2018) 151–160. https://doi.org/10.1016/j.compstruct.2018.06.029.

[3] Y.Y.Y. Cao, Q.L. Yu, H.J.H. Brouwers, W. Chen, Predicting the rate effects on hooked-end fiber pullout performance from Ultra- High Performance Concrete, Cem. Concr. Res. 120 (2019) 164–175. https://doi.org/10.1182/blood-2016-03-705590.

[4] G. Murali, S.R. Abid, Y.H. Mugahed Amran, H.S. Abdelgader, R. Fediuk, A. Susrutha, K. Poonguzhali, Impact performance of novel multi-layered prepacked aggregate fibrous composites under compression and bending, Structures 28 (2020) 1502–1515. https://doi.org/10.1016/j.istruc.2020.10.001.

[5] G. Murali, K. Ramprasad, A feasibility of enhancing the impact strength of novel layered two stage fibrous concrete slabs, Eng. Struct. 175 (2018) 41–49. https://doi.org/10.1016/j.engstruct.2018.08.034.

[6] V.R. Ramkumar, G. Murali, N.P. Asrani, K. Karthikeyan, Development of a novel low carbon cementitious two stage layered fibrous concrete with superior impact strength, J. Build. Eng. 25 (2019) 100841. https://doi.org/10.1016/j.jobe.2019.100841.

[7] Y.Y.Y. Cao, M. Sluijsmans, Q.L. Yu, H.J.H. Brouwers, Ballistic performances of multi-layered Ultra-high Performance Fibre Reinforced Concrete, in: 2nd Int. Conf. Sustain. Build. Mater., Eindhoven, 2019: pp. 1–9.

[8] Y.Y.Y. Cao, P.P. Li, H.J.H. Brouwers, Q.L. Yu, Resistance of multi-layered UHPFRC against in-service projectile: Experimental investigation and modelling prediction, Compos. Struct. 244 (2020) 112295. https://doi.org/10.1016/j.compstruct.2020.112295.

[9] P.P. Li, Q.L. Yu, H.J.H. Brouwers, W. Chen, Conceptual design and performance evaluation of two-stage ultra-low binder ultra-high performance concrete, Cem. Concr. Res. 125 (2019). https://doi.org/10.1016/j.cemconres.2019.105858.

[10] D. Song, Q. Tan, C. Meng, Y. Huang, Y. Cao, Resistance of grid steel-tube-confined concrete targets against projectile impact: Experimental investigation and analytical engineering model, Def. Technol. 18 (2022) 1622–1642.

[11] M.F. Najjar, A.M. Soliman, M.L. Nehdi, Critical overview of two-stage concrete: Properties and applications, Constr. Build. Mater. 62 (2014) 47–58. https://doi.org/10.1016/j.conbuildmat.2014.03.021.

# STRUCTURAL INTEGRITY OF MILD STEEL SANDWICH PANELS SUBJECTED TO AIR-BACKED UNDERWATER SHOCK LOADS

*Anupoju Rajeev[1], and Prince Jeya Lal Lazar[2]*

[1] Research Fellow, Civil and Environmental Engineering, NUS, Singapore, DrRajeev@nus.edu.sg

[2] Associate Professor, Department of Mechanical Engineering, Rajalakshmi Institute of Technology, India, princejeyalal@gmail.com

**Corresponding Author: Prince Jeya Lal Lazar, PhD**

Rajalakshmi Institute of Technology, Chennai, Tamil Nadu, India, 600124

**Email:** princejeyalal@gmail.com

## ABSTRACT

A computational fluid-structure interaction (FSI) approach was employed to assess the structural integrity of sandwich panels under air-backed underwater explosion (UNDEX) loading conditions. Square honeycomb core sandwich panels (300×250 mm) with a core relative density ranging from 3 – 10 % were developed using mild steel, with identical 2 mm front and back face sheets. Two sandwich configurations were developed: (i) with varying core relative density and (ii) with varying core height with equivalent relative density. All simulations utilized the Finite Element (FE) Explicit Solver and a UNDEX algorithm, with shock factor variations from 0.42 to 0.73 at a constant standoff distance of 150 mm. Simulations revealed that the core relative density of the sandwich panels served as a predominant design variable. Dominant failure modes included front face sheet stretching, and core crushing, alongside front face sheet midpoint deflection. This numerical analysis demonstrates the potential of computational simulations to accurately predict the structural response of sandwich panels under extreme events like underwater explosions.

***Keywords:*** *Fluid-structure interaction, structural integrity, underwater explosion, honeycomb sandwich panel, Abaqus CAE*

## INTRODUCTION

Shock loading poses critical challenges to both civil and marine structures, demanding robust design against sudden, intense forces to ensure structural integrity and safety [1, 2]. Sandwich structures incorporating periodic and metallic cellular cores have demonstrated exceptional crushing characteristics when subjected to dynamic loading conditions. Over the past few decades, researchers have favored the utilization of sandwich panels as protective barriers, owing to their ability to mitigate structural damage resulting from extreme load cases, such as impact and blast events The simplistic yet efficient design of these sandwich panels, comprising metallic face sheets and periodic cores, exhibits progressive crushing behavior and remarkable load-bearing capabilities [3,4].

The functional performance of sandwich panels can be further augmented through the integration of novel core topologies inspired by biomimetic concepts, metallic foams, corrugated structures, functionally graded materials, and hybrid face sheet configurations [5–9]. Pioneering studies by Zhu et al., [10] and Fan et al., [11] have investigated the structural integrity of sandwich panels by varying parameters such as face sheet thickness, unit cell size, core wall thickness, standoff distance (SoD), and charge mass.

Experimental investigations involving underwater explosions typically require the detonation of an explosive charge, a process that poses significant risks to research personnel, disrupts marine ecosystems, and contributes to environmental pollution. To circumvent these challenges, researchers [12,13] have established safer and more economical lab-scale underwater shock generator facilities, enabling controlled experimental conditions.

Sandwich panels exhibit enhanced damage mitigation capabilities during underwater explosions due to the intricate fluid-structure interactions (FSI) [6]. When subjected to an air-backed underwater explosion, these sandwich panels undergo distinct phases: (i) FSI, (ii) front face sheet deformation, (iii) core compression, and (iv) back face sheet deformation and panel bending [14].

The present study aims to numerically investigate the effects of shockwaves on metallic sandwich panels subjected to underwater explosions of varying magnitudes. To this end, a series of simulations were performed using validated finite element analysis (FEA) models to establish FSI on the sandwich panels and evaluate their mechanical properties. Two distinct core designs were developed by varying the core relative density and core height. The influence of these core design variables is evaluated and presented.

# COMPUTATIONAL MODELING

## Underwater explosion (UNDEX)

Underwater explosions generate shock waves that release immense quantities of energy over an extremely short duration, typically lasting between $10^{-5}$ to $10^{-3}$ seconds. The decay of the blast pressure induced by these shock waves can be approximated as a function of two key parameters: the mass of the explosive charge and the standoff distance from the explosion source. The pressure profile resulting from an underwater explosion event can be evaluated using the following empirical equation [17]:

$$P(t) = P_{\max}\, exp\left[-\frac{(t-t_d)}{\theta}\right];\ 0 \leq t \leq \theta \quad (1)$$

This empirical formulation provides a means to estimate the pressure characteristics based on the explosive mass and standoff distance, enabling researchers to predict and analyze the effects of underwater blast loading on structures and materials.

$P_{max}$ is determined by,

$$P_{max} = K_1 \left( \frac{W^{1/3}}{R} \right)^{A_1} \tag{2}$$

the decay constant $\theta$ is determined by,

$$\theta = W^{1/3} K_2 \left( \frac{W^{1/3}}{R} \right)^{A_2} \tag{3}$$

The impulse (I) and the total energy (E) is determined by

$$I = W^{1/3} K_3 \left( \frac{W^{1/3}}{R} \right)^{A_3} \tag{4}$$

$$E = W^{1/3} K_4 \left( \frac{W^{1/3}}{R} \right)^{A_4} \tag{5}$$

Fluid-structure interaction (FSI) during underwater explosions (UNDEX) gives rise to nonlinearities stemming from the cavitation phenomenon. It is crucial to account for these nonlinearities in computational analyses using a continuum approach to accurately predict the deformation behavior of structures subjected to UNDEX events. The total pressure evolving after FSI must be incorporated into the analysis, which can be determined using Taylor's theory.

Table 1 lists the values of the constants present in Equations (2) to (5) for the tri-nitro toluene (TNT) explosive, providing the necessary parameters related to the weight (W) of the explosive charge and the standoff distance (SoD) from the explosion source.

Incorporating these nonlinearities and the total pressure resulting from FSI, along with the empirical constants specific to the explosive material, enables researchers to conduct accurate computational simulations and analyses to predict the structural response and deformation characteristics during UNDEX scenarios.

**Table 1.** Constants for TNT explosives [15]

| Parameter | Constant | Value |
|---|---|---|
| Peak Pressure ($P_{max}$) | $K_1$ | 52.4 |
| | $A_1$ | 1.13 |
| Decay Constant ($\theta$) | $K_2$ | 0.084 |
| | $A_2$ | -0.23 |
| Impulse (I) | $K_3$ | 5.75 |
| | $A_3$ | 0.89 |
| Total Energy ($E$) | $K_4$ | 84.4 |
| | $A_4$ | 2.04 |

The severity of an underwater explosion (UNDEX) event can be quantified using the shock factor (SF), which is a function of the TNT weight, standoff distance (SoD), and the angle of the underwater explosion. In this computational analysis, a range of SFs was considered, varying from 0.42 to 0.73, by modulating the TNT mass while maintaining a constant standoff distance. The specific values of SFs employed in the present analysis are presented in Table 2. The shock factor can be evaluated using the following expression:

$$SF = \frac{(1+cos\varphi)}{2}\frac{\sqrt{W}}{R} \tag{6}$$

This shock factor parameter serves as a measure of the intensity of the UNDEX event, considering the explosive charge mass, standoff distance, and the angular orientation of the explosion. By considering a range of shock factor values, the computational analysis can investigate the structural response and deformation behavior under varying intensities of underwater blast loading.

**Table 2.** Shock Factors for Underwater Explosion (UNDEX) [16]

| Sl. No. | Standoff distance | Charge Weight W (kg) | Shock Factor SF ($kg^{1/2}/m$) | Peak Pressure (MPa) |
|---|---|---|---|---|
| 1 | 0.150 | 0.020 | 0.42 | 202.0 |
| 2 | | 0.040 | 0.6 | 268.0 |
| 3 | | 0.050 | 0.67 | 302.6 |
| 4 | | 0.060 | 0.73 | 313.0 |

## Johnson-Cook (J-C) constitutive material model

In the present fluid-structure interaction analysis for underwater explosions (UNDEX), the all-metallic honeycomb panel is constructed using mild steel. The selection of mild steel is consistent with the material employed by Ramajeyathilagam and Vendhan [16] in their experimental evaluation of deformation in rectangular plates subjected to underwater explosions. To ensure accurate computational modeling, an elasto-viscoplastic material model, known as the Johnson-Cook (J-C) model, is employed. This model incorporates the effects of thermo-elasticity, strain rate hardening, and adiabatic softening, making it widely preferred for computational analyses involving intense impulse loading scenarios, such as those encountered during detonation of explosives [17]. Table 3 and Table 4 list the J-C material and damage parameters for mild steel, summarized from [18,19]. The employed J-C plastic model can be expressed as (eq. 7), where A, B, C, n, and m are material constants, and $\bar{\varepsilon}_{pl}$, $\dot{\varepsilon}_0$ represent the equivalent plastic strain rate and reference strain rate, respectively. To account for temperature effects, the model incorporates parameters such as the normal temperature ($T$), the melting temperature ($T_m$), and the transition temperature ($T_t$) of the material.

$$\sigma_y = \left[A + B(\bar{\varepsilon}_{pl})^n\right]\left[1 + C\ln\left(\frac{\bar{\varepsilon}_{pl}}{\dot{\varepsilon}_0}\right)\right]\left[1 - \left(\frac{T - T_t}{T_m - T_t}\right)^m\right] \tag{7}$$

**Table 3.** J-C material parameters of mild steel [18,19]

| $\rho$ | E | $\upsilon$ | A | B | C | n | m | $\dot{\varepsilon}_0$ | Tt | Tm |
|---|---|---|---|---|---|---|---|---|---|---|
| kg/m$^3$ | GPa | | MPa | MPa | | | | s$^{-1}$ | K | K |
| 7850 | 210 | 0.3 | 460 | 1227 | 0.723 | 0.068 | 1.89 | 0.06 | 298 | 1798 |

**Table 4.** Damage parameters of mild steel [18,19]

| D1 | D2 | D3 | D4 | D5 |
|---|---|---|---|---|
| 0.1152 | 1.0116 | -1.7684 | -0.05279 | 0.5262 |

## Validation of the UNDEX model

The numerical simulation of fluid-structure interaction (FSI) established in the present work for a mild steel plate with dimensions of 300 x 250 x 2 mm under varying shock factors (SFs) is validated against the experimental results reported in Ramajeyathilagam and Vendhan [16]. The permanent midpoint deformation of the target plates subjected to underwater explosion (UNDEX) loading is presented and compared with the experimental values in Figure 1. The deformed plates under UNDEX loading are visualized through multi-view cuts to represent the depth of deformation, as shown in Figure 2. Table 5 summarizes the validated results of the present simulation and their comparison with the experimental values. The accuracy of the present numerical FSI scheme exhibited an error of less than 5% for SFs up to 0.67. However, an error of 8.48% was observed for SF 0.73. Consequently, the validated numerical FSI scheme was employed to further analyze the structural integrity of sandwich targets subjected to underwater explosions.

The validation process involved comparing the numerical simulations of FSI for a mild steel plate under varying shock factors with experimental data from Ramajeyathilagam and Vendhan [16]. The key comparison metric was the permanent midpoint deformation of the target plates under UNDEX loading. Visualization of the deformed plates and tabulated results confirmed the accuracy of the numerical scheme, with errors within an acceptable range for most shock factors considered, enabling its application to sandwich panel analyses under underwater blast loading.

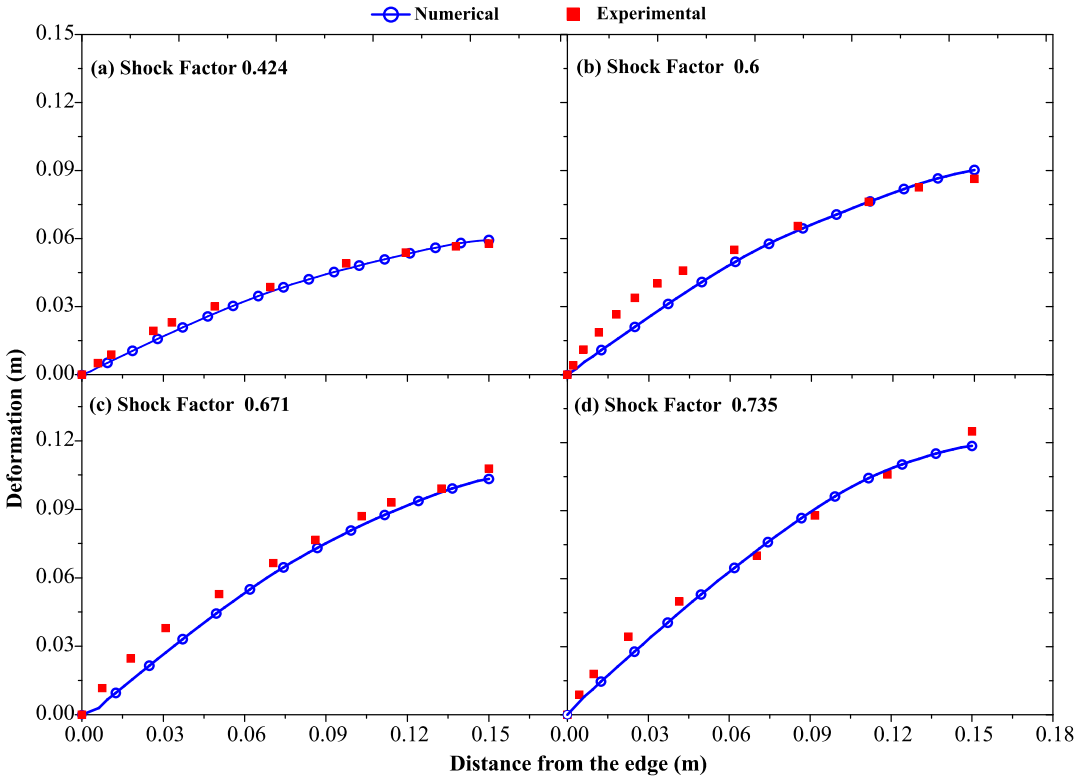


**Figure 1.** Comparison of present numerical and experimental data [16] of front face midpoint deflection for varying SFs

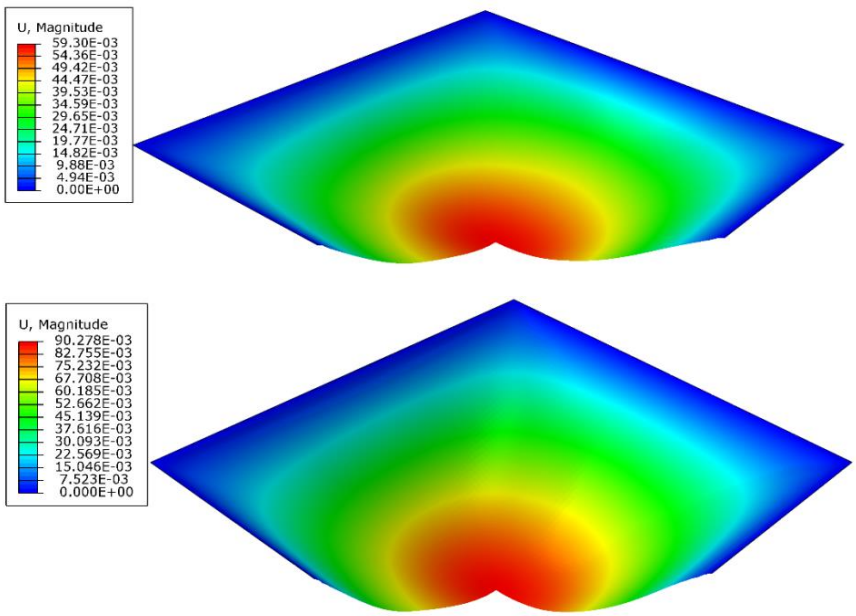

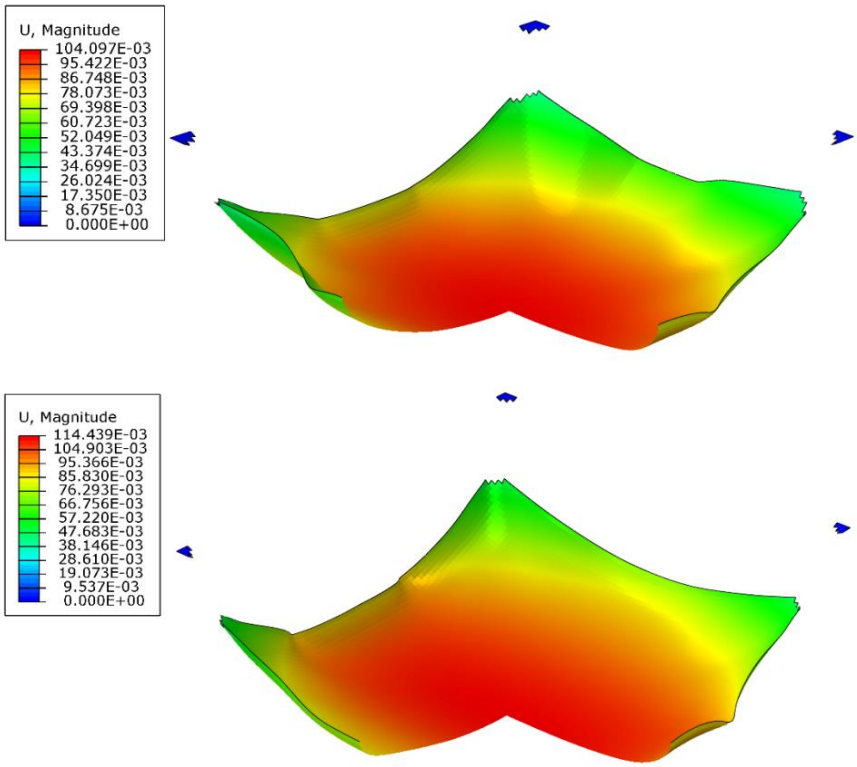


**Figure 2.** Contours of permanent deformation of mild steel plates subjected to UNDEX loading in the present simulations (a) SF 0.42 (b) SF 0.6 (c) SF 0.67 (d) SF 0.73

**Table 5.** Summary of numerical results validated with the experiments.

| Sl. No. | Standoff distance R (mm) | Shock Factor SF ($kg^{1/2}/m$) | Front face midpoint deformation (mm) | | Error (%) |
|---|---|---|---|---|---|
| | | | Experimental [16] | Numerical [Present Work] | |
| 1 | 150 | 0.42 | 57.8 | 59.3 | 2.59 |
| 2 | | 0.60 | 86.4 | 90.2 | 4.39 |
| 3 | | 0.67 | 107.8 | 104.0 | 3.52 |
| 4 | | 0.73 | 125.0 | 114.4 | 8.48 |

## Target geometry, mesh, and constraints

A sandwich panel is composed of three main components: the front face sheet, the core, and the back face sheet. In the present numerical investigation of all-metallic honeycomb sandwich panels, the inner core dimensions were 300 x 250 x 15 mm. Both the front and back face plates had dimensions of 300 x 250 x 2 mm, resulting in an overall panel height of 19 mm. The cell walls of the square honeycomb core were evenly spaced at 15 mm. The relative density (RD) of the core can be tailored by varying the cell height and cell wall thickness. Figure 3 provides

a clear illustration of the sandwich panel configuration used in this analysis. Table 6 presents the different sandwich configurations with varying RD values.

The sandwich panel targets were categorized into two groups based on their RD values. Group A sandwich panels had increasing RD values achieved by incrementing the cell wall thickness while maintaining a constant core height. In contrast, Group B sandwich panels had an increased core height but with identical RD values, achieved by decreasing the cell wall thickness.

This systematic variation in core parameters allowed for the investigation of the influence of relative density and core geometry on the structural response and deformation behavior of the sandwich panels under underwater explosion loading.

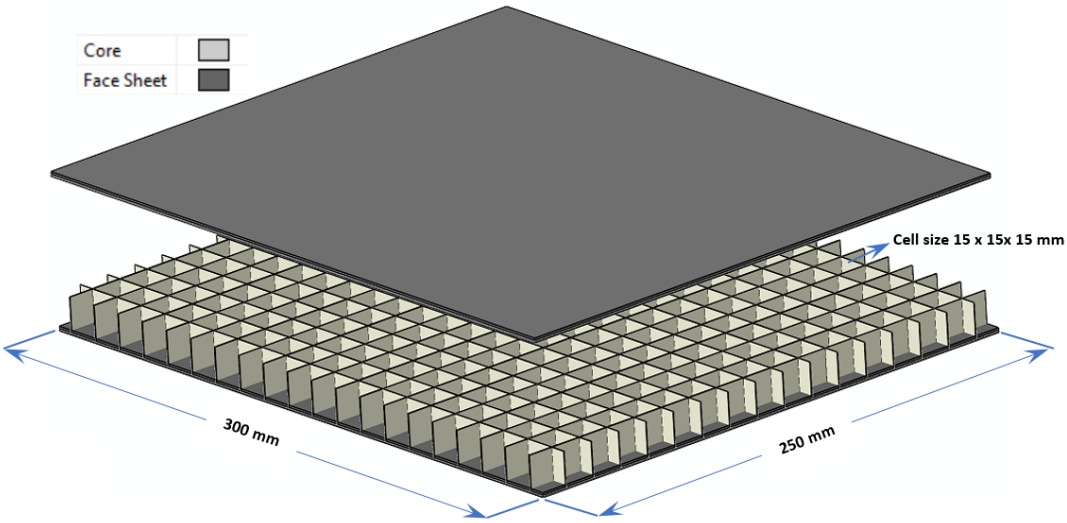


**Figure 3.** Sandwich geometry with square honeycombs of dimensions 300 x 250 x 19 mm (face sheet thick 2 mm)

**Table 6.** Sandwich Configurations

| Group ID | Target ID | Core height (mm) | Core cell wall thickness (mm) | Relative density of core (%) | Core mass (kg) |
|---|---|---|---|---|---|
| Group A | SW-RD3.2 | 15 | 0.25 | 3.2 | 0.289 |
| | SW-RD6.5 | | 0.50 | 6.5 | 0.578 |
| | SW-RD9.7 | | 0.75 | 9.7 | 0.867 |
| Group B | SW-CH15 | 15 | 0.25 | 3.2 | 0.289 |
| | SW-CH20 | 20 | 0.18 | 3.2 | 0.285 |
| | SW-CH25 | 25 | 0.15 | 3.2 | 0.289 |

The top and bottom face sheets, as well as the core of the sandwich panel, were discretized using 8400 linear quadrilateral elements with reduced integration linear shell elements of type S4R. These S4R elements incorporate hourglass control to prevent element distortion. The core

was meshed with 16365 linear quadrilateral elements of the same type (S4R). To represent a permanent connection between the core and face sheets, the top and bottom edges of the core were tied to the respective top and bottom face sheet surfaces using a tie constraint.

All sides of the front and back face sheets were constrained, and the source of the underwater explosion was located 150 mm away from the midpoint of the front face sheet. The fluid-structure interaction (FSI) of the incident shock wave on the front face sheet, induced by the underwater detonation of varying TNT masses ranging from 20 to 60 grams, was established using the UNDEX definition in the numerical model.

This discretization approach, along with the appropriate boundary conditions and FSI modeling, enabled the numerical investigation of the sandwich panel's response to underwater explosion loading of varying intensities, facilitated by the detonation of different TNT charge masses.

# RESULTS AND DISCUSSION

## Effects of Core Relative Density

The influence of core relative density (RD) on front face deformation and core energy absorption was investigated through mechanical analysis of metallic sandwich panels SW-RD3.2, SW-RD6.5, and SW-RD9.7 subjected to underwater explosion (UNDEX) loading conditions. These panels exhibited varying masses due to differences in core wall thickness, with SW-RD3.2 having the lowest mass (0.289 kg) and SW-RD9.7 the highest (0.867 kg), attributed to variations in core cell thickness. Notably, this change in core mass significantly influenced panel behavior.

Underwater explosions established shock wave-sandwich front face sheet interaction, resulting in permanent dimple deformation of the face sheet. However, as the face sheet is permanently connected to the core, deformation is constrained by the core. Core yielding initiates core crushing, followed by back face deformation until the incident shock wave effects dissipate.

**Error! Reference source not found.**4 (a) illustrates the maximum deformation in SW-RD3.2, SW-RD6.5, and SW-RD9.7 for varying SFs. Front face midpoint deflection increased with SF but decreased with core RD due to higher core stiffness achieved through increased cell wall thickness. Lesser deformation was observed in cores with higher RD, indicating their enhanced resistance to bending and crushing.

Energy absorption by square honeycomb cores with varying RDs for SFs ranging from 0.4 to 0.73 is depicted in 4 (b) and (c). Energy absorption increased with SF due to greater plastic deformation, while a decrease was recorded with increasing RD due to enhanced core stiffness, resulting in minimal permanent deformation. However, noteworthy increments in core energy absorption were observed for SF 0.67 and 0.73 across all panels exhibiting higher blast-resistant potential.

Permanent deformations induced in Group A sandwich panels SW-RD3.2, SW-RD6.5, and SW-RD9.7 for varying shock factors (SFs) are depicted in Figure 5. Despite experiencing

higher damage at the center due to TNT positioning, the degree of damage varied significantly with SF magnitude. For SF 0.42, all panels exhibited out-of-plane permanent deformation without significant core crushing. However, as SF increased to 0.6 and 0.73, SW-RD3.2 underwent complete core crushing for all SFs, whereas SW-RD9.7 resisted core crushing across all SFs with lesser deformation compared to other panels.

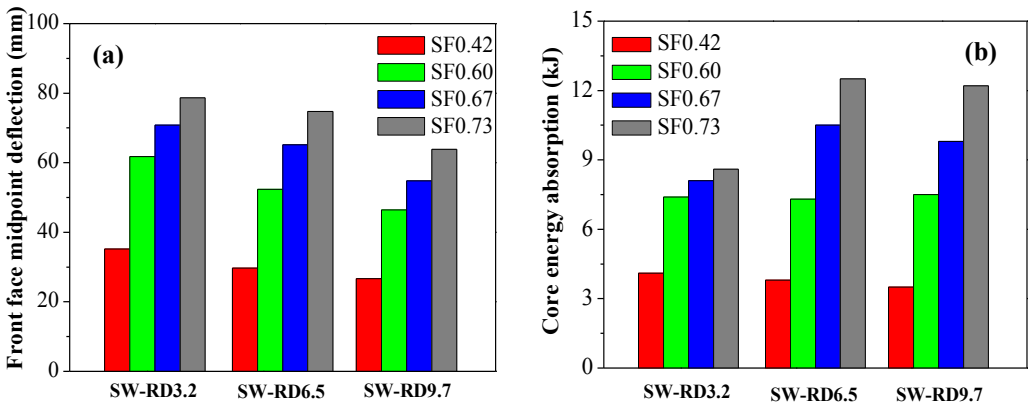


**Figure 4. (a)** Peak midpoint deformation on the front face of sandwich panel **(b)** Core energy absorption against varying SFs

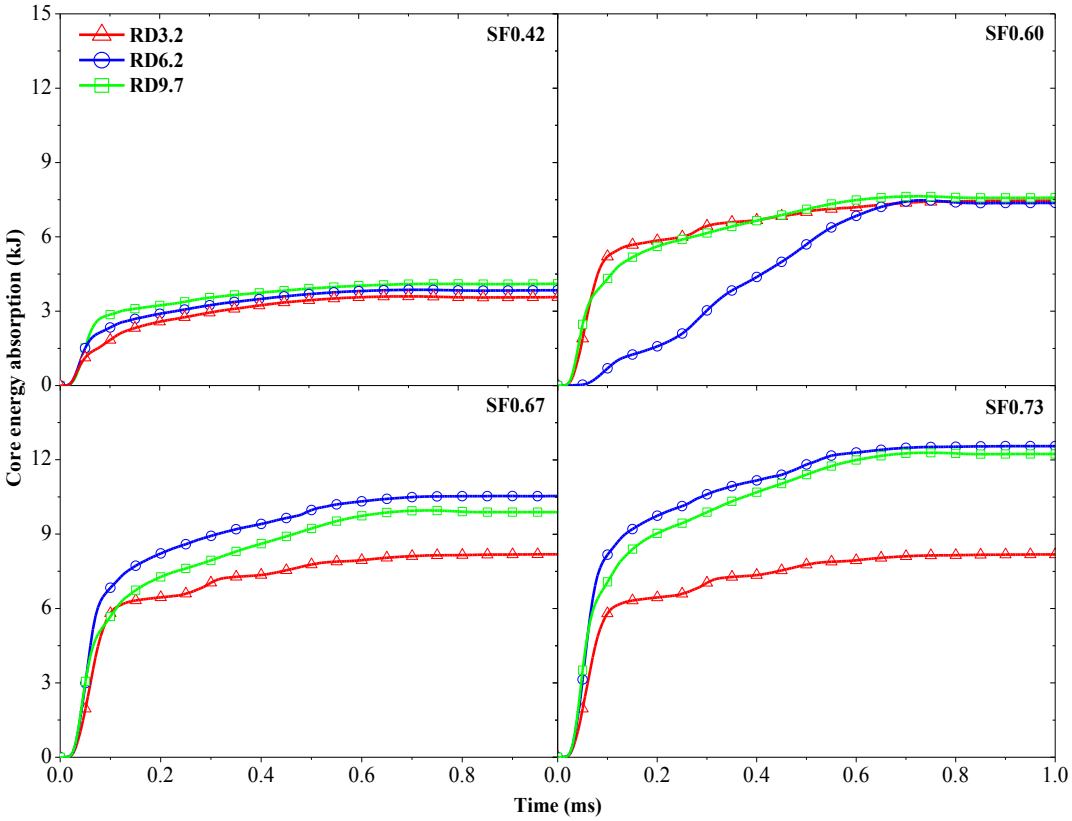


**(c)** Core energy absorption vs Time plots for varying SFs

| Shock Factor (SF) | Target ID | | |
|---|---|---|---|
| | SW-RD3.2 | SW-RD6.5 | SW-RD9.7 |
| SF=0.42 | 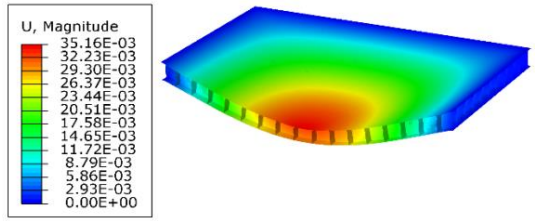 | 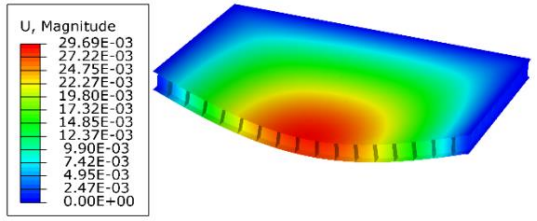 | 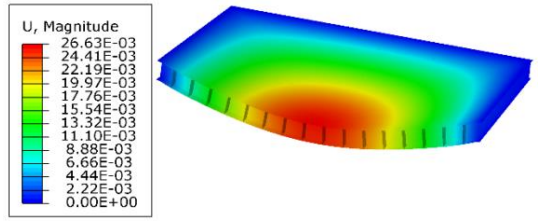 |
| SF=0.6 | 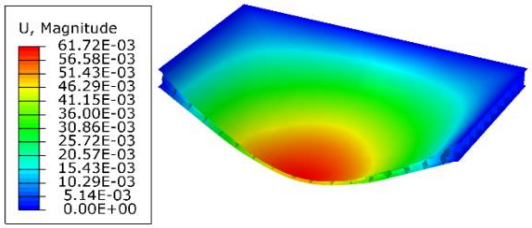 | 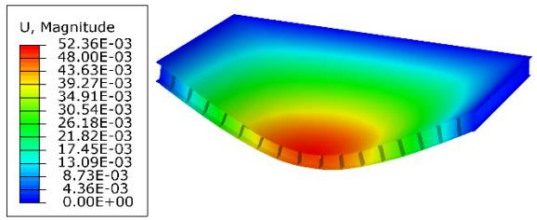 | 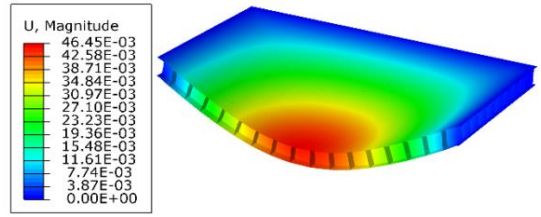 |
| SF=0.67 | 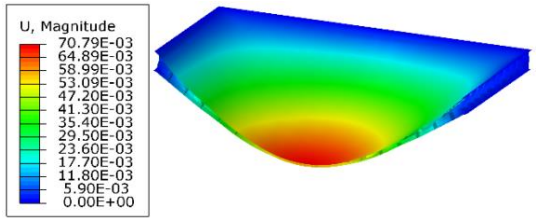 | 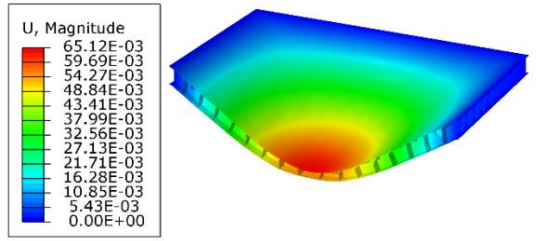 | 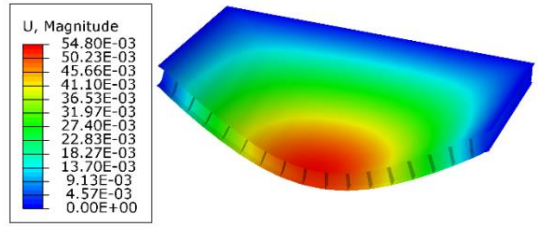 |
| SF=0.73 | 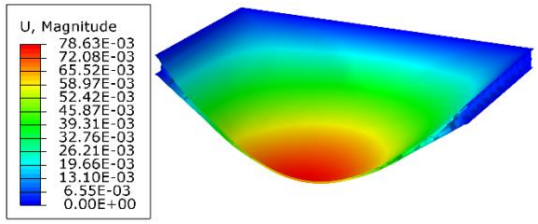 | 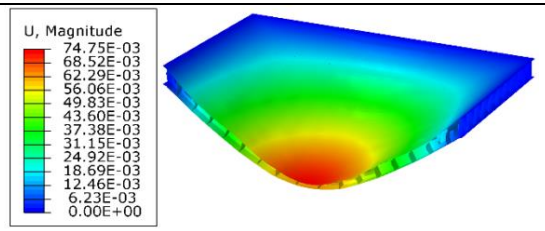 | 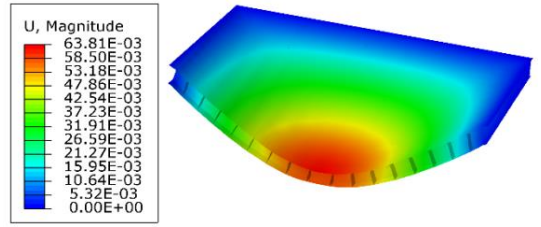 |

**Figure 5.** Front face midpoint deflection of Group A sandwich panels against varying SFs

## Effects of core height for identical RD

The influence of core height on sandwich panels with equivalent relative densities (RD) subjected to varying shock factors (SFs) was investigated using Group B sandwich panels SW-CH15, SW-CH20, and SW-CH25. Cores with equivalent RD were achieved by varying core cell wall thickness. Front face deformation contours and peak front face midpoint deflections for different SFs were analyzed (Figure  (a) and Figure  respectively), along with peak core energy absorption (Figure 6 (b) & (c).

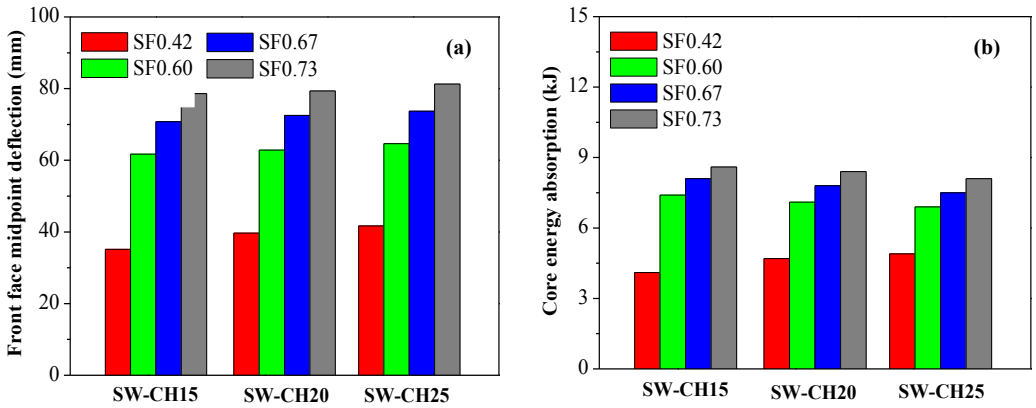


**Figure 6. (a)** Peak midpoint deformation on the front face of sandwich panel **(b)** Core energy absorption against varying SFs

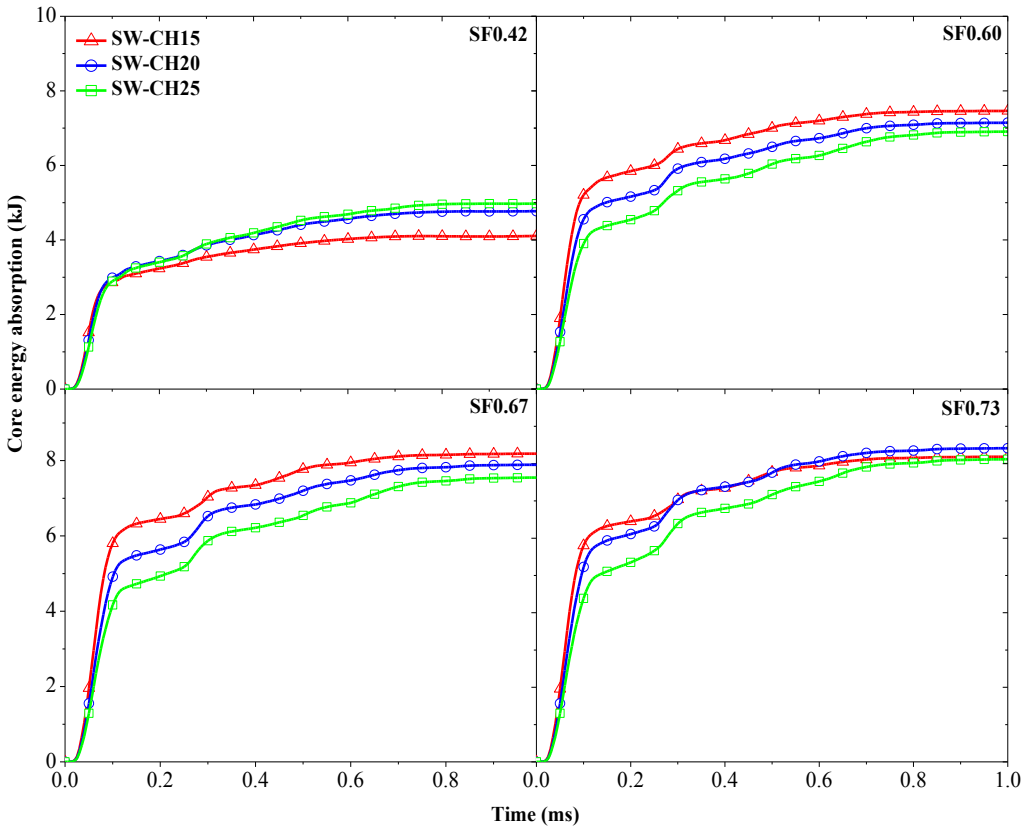

**(c)** Core energy absorption vs Time plots for varying SFs

Observations revealed that front face sheet deflection and core energy absorption increased with rising SFs, with a notable increase observed at low SF 0.42 for SW-CH15, while variations were minimal for higher SF magnitudes. As core height increased, cell wall thickness decreased to maintain equivalent core mass. For example, SW-CH15 had a core thickness of 0.25 mm, while SW-CH20 and SW-CH25 had reduced thicknesses of 0.18 mm and 0.15 mm, respectively, representing decreases of 28% and 40% compared to SW-CH15, and 16.6% compared to SW-CH20. This design modification directly impacted core stiffness, thereby influencing panel deformation and energy absorption behavior.

| Shock Factor (SF) | Target ID | | |
|---|---|---|---|
| | SW-CH15 | SW-CH20 | SW-CH25 |
| SF=0.42 | 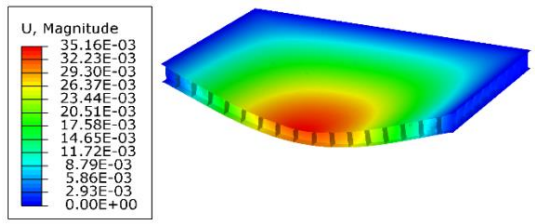 | 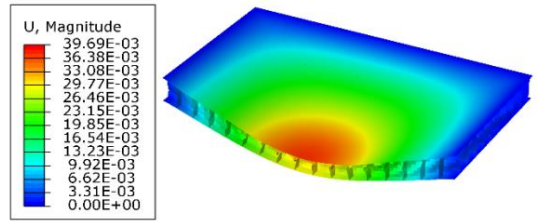 | 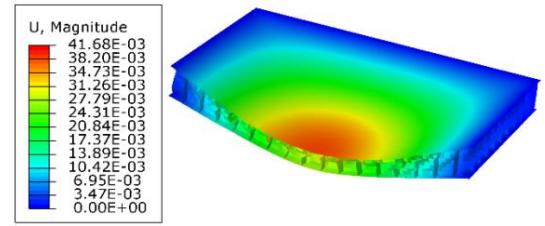 |
| SF=0.6 | 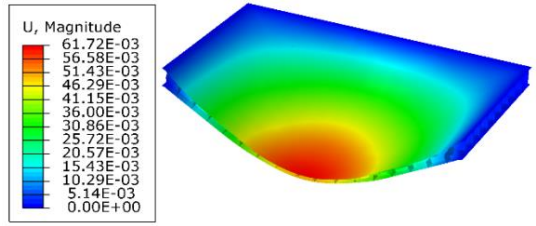 | 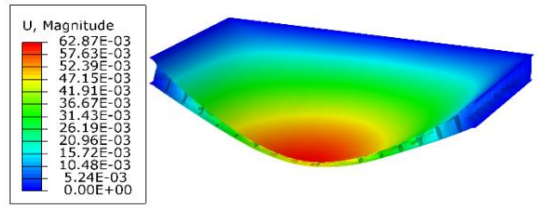 | 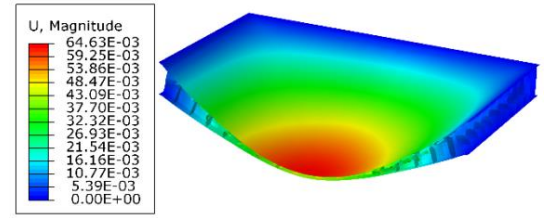 |
| SF=0.67 | 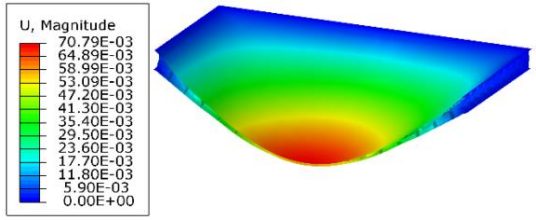 | 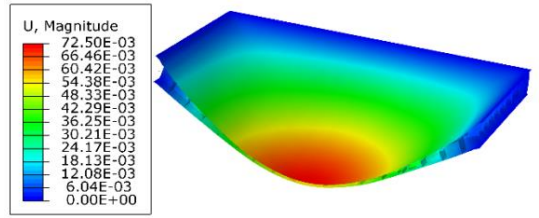 | 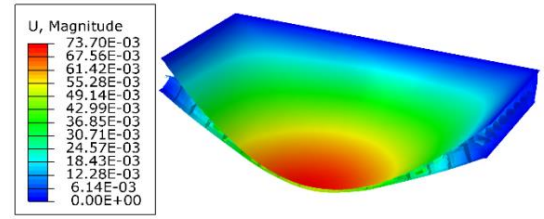 |
| SF=0.73 | 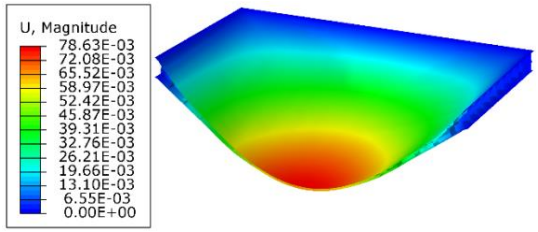 | 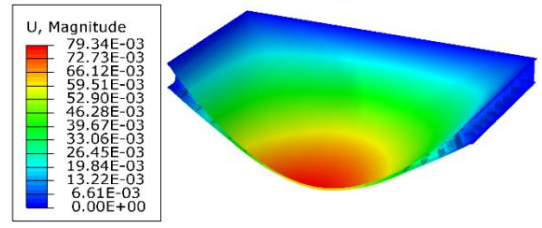 | 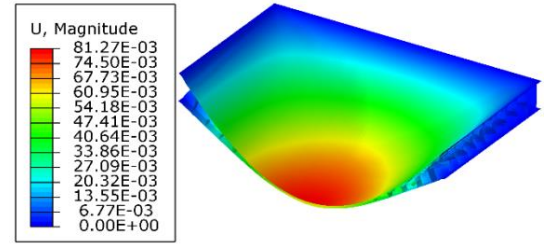 |

**Figure 7.** Front face midpoint deflection of Group B sandwich panels against varying SFs

# CONCLUSIONS

This study assessed the impact of design parameters such as core relative density and core height on the deformation and energy absorption characteristics of metallic sandwich panels subjected to underwater explosions with varying shock magnitudes. The key findings are outlined below:

- Across all cases, an increase in shock factor (SF) led to a corresponding rise in permanent deformation on the front face, accompanied by increased core energy absorption.
- Higher core relative density resulted in reduced front-face midpoint deflections and decreased core energy absorption. Conversely, an increase in core height was associated with an escalating trend in front-face sheet deflection.
- For SF 0.4, predominant failure modes included front face sheet deformation and core cell wall buckling across all cases. As SF increased, a transition to front-face deflection followed by core crushing was observed.

## Future scope

Following an extensive review of existing literature, it is evident that research on the blast mitigation capabilities of sandwich panels incorporating bio-inspired core designs is scarce. Previous studies primarily focus on conventional core geometries such as circular, hexagonal, and square. Furthermore, investigations into the use of composite materials and fiber metal laminates (FMLs) in sandwich panels for explosion resistance are limited.

Therefore, it is recommended to explore the potential of bio-inspired core designs to enhance the blast mitigation effectiveness of sandwich panels, both for surface and underwater applications. Additionally, the utilization of FMLs and hybrid materials presents an opportunity to develop lightweight sandwich panels for blast mitigation applications.

# REFERENCES


[1] Anupoju Rajeev, Sai Sharath Parsi, Prince Jeya Lal Lazar, Dynamic Response Analysis of Reinforced Column Subjected To Shock Wave Loading, Procedia Structural Integrity, Volume 60, 2024, Pages 222-232, https://doi.org/10.1016/j.prostr.2024.05.044.

[2] Prince Jeya Lal Lazar, Anupoju Rajeev, Deformation behavior of super-austenitic stainless steel sandwich panels subjected to air blast and underwater explosion, Procedia Structural Integrity, Volume 60, 2024, Pages 185-194, https://doi.org/10.1016/j.prostr.2024.05.040

[3] Qi C, Remennikov A, Pei L-Z, Yang S, Yu Z-H, Ngo TD. Impact and close-in blast response of auxetic honeycomb-cored sandwich panels: Experimental tests and numerical simulations. Composite Structures 2017;180:161–78.

[4] Karagiozova D, Nurick GN, Langdon GS. Behavior of sandwich panels subject to intense air blasts–Part 2: Numerical simulation. Composite Structures 2009;91:442–50.

[5] Tran P, Ngo TD, Mendis P. Bio-inspired composite structures subjected to underwater impulsive loading. Computational Materials Science 2014;82:134–9.

[6] Hutchinson JW, Xue Z. Metal sandwich plates optimized for pressure impulses. International Journal of Mechanical Sciences 2005;47:545–69.

[7] Imbalzano G, Linforth S, Ngo TD, Lee PVS, Tran P. Blast resistance of auxetic and honeycomb sandwich panels: Comparisons and parametric designs. Composite Structures 2018;183:242–61.

[8] Sun G, Huo X, Chen D, Li Q. Experimental and numerical study on honeycomb sandwich panels under bending and in-panel compression. Materials & Design 2017;133:154–68.
[9] Boonkong T, Shen Y, Guan Z, Cantwell W. The low-velocity impact response of curvilinear-core sandwich structures. International Journal of Impact Engineering 2016;93:28–38.
[10] Zhu F, Zhao L, Lu G, Wang Z. Deformation and failure of blast-loaded metallic sandwich panels—experimental investigations. International Journal of Impact Engineering 2008;35:937–51.
[11] Fan Z, Liu Y, Xu P. Blast resistance of metallic sandwich panels subjected to proximity underwater explosion. International Journal of Impact Engineering 2016;93:128–35.
[12] Deshpande V, Heaver A, Fleck N. An underwater shock simulator. Proceedings of the Royal Society A: Mathematical, Physical and Engineering Sciences 2006;462:1021–41.
[13] Ren P, Zhou J, Tian A, Ye R, Shi L, Zhang W, et al. Experimental investigation on dynamic failure of carbon/epoxy laminates under underwater impulsive loading. Marine Structures 2018;59:285–300.
[14] Schiffer A, Tagarielli V. One-dimensional response of sandwich plates to underwater blast: fluid-structure interaction experiments and simulations. International Journal of Impact Engineering 2014;71:34–49.
[15] Kumar YP, Gupta N, Rao YS, Kant B. On shock response of marine sandwich structures subjected to UNDEX loading. Procedia Engineering 2017;173:1932–42.
[16] Ramajeyathilagam K, Vendhan C. Deformation and rupture of thin rectangular plates subjected to underwater shock. International Journal of Impact Engineering 2004;30:699–719.
[17] Gupta N, Kumar P, Hegde S. On deformation and tearing of stiffened and un-stiffened square plates subjected to underwater explosion—a numerical study. International Journal of Mechanical Sciences 2010;52:733–44.
[18] Yadav S, Singhal S, Jasra Y, Saxena RK. Determination of Johnson-Cook material model for weldment of mild steel. Materials Today: Proceedings 2020;28:1801–8.
[19] Senthil K, Iqbal MA, Bhargava P, Gupta N. Experimental and numerical studies on mild steel plates against 7.62 API projectiles. Procedia Engineering 2017;173:369–74.

# RESEARCH ADVANCEMENT ON CFST WITH LOCALIZED PITTING CORROSION SUBJECTED TO STATIC AND IMPACT LOADING

*Chao Hou[1], Wendong Chen[2], Gen Li[3]*

[1] Ph.D., Southern University of Science and Technology, houc@sustech.edu.cn.

[2] B.Eng., Southern University of Science and Technology, 12332237@mail.sustech.edu.cn.

[3] Ph.D., Indara Digital Infrastructure, Gen.Li@indara.com.

**Corresponding Author: Chao Hou, Ph.D., etc.**

Southern University of Science and Technology, Shenzhen, Guangdong, China, 518055

**Email:** houc@sustech.edu.cn.

## ABSTRACT

Concrete-filled steel tubular (CFST) columns have been widely utilized in the field of ocean construction in recent years, while the degradation induced by localized pitting corrosion is becoming increasingly prominent. Considering their random nature in terms of the distribution patterns and the geometric characteristics of corrosion pits, refined finite element analysis models are developed in the authors' recent studies, which take into account the strain rate effects on concrete and steel materials. Comprehensive investigations are then presented on the static and lateral impact behaviour of CFST with no corrosion, uniform corrosion, and localized pitting corrosion. The obtained analytical results reveal that the influence of localized pitting corrosion damage can be categorized as the stress concentration around the corrosion pits along the steel tube, the increased susceptibility to local buckling of the steel tube, the weakened confinement towards concrete, together with the reduction in the bearing capacity and energy absorption. On this basis, an extended parametric study is carried out to determine the key parameters of pitted CFST. Finally, simplified design models for the residual strength prediction are introduced through modifying the methods in existing design standards.

***Keywords:*** *Concrete-filled steel tube (CFST), Localized pitting corrosion, Static loading, Impact loading, Residual strength prediction.*

## 1. INTRODUCTION

Concrete-filled steel tubes (CFST) have been utilized as the prominent load-bearing components of modernized infrastructure due to their favourable structural behaviour, excellent constructability, and remarkable energy absorption capacity [1,2], which have been widely explored in offshore and ocean engineering [3,4]. Figure 1 and Table 1 show three typical loading scenarios of CFST in an offshore structure, i.e., the axial compression scenario, the combined compression-bending scenario, and the lateral loading scenario.

Pitting corrosion is considered the primary corrosion form for structural steel in practice [5], the complex process of which is affected by multiple factors such as temperature, microorganisms, bacteria, pH, etc [6,7]. For simplicity, existing design methods normally treat localized pitting corrosion as uniform corrosion with equivalent thickness losses. If poorly designed, the residual capacity of steel-related components with localized pitting corrosion tends to be overestimated. Therefore, it is necessary to quantitatively reveal the effect of localized pitting corrosion on the behavior of CFST in typical service scenarios.

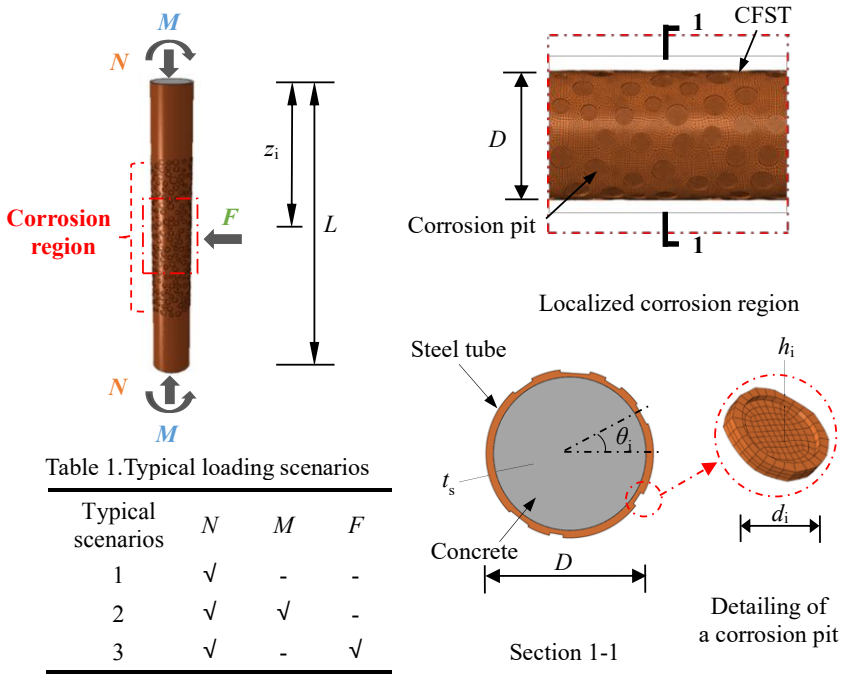


Table 1.Typical loading scenarios

| Typical scenarios | *N* | *M* | *F* |
|---|---|---|---|
| 1 | √ | - | - |
| 2 | √ | √ | - |
| 3 | √ | - | √ |

**Figure 1.** Typical loading scenarios and the FEA modelling for CFST with localized pitting corrosion

## 2. FINITE ELEMENT MODELLING TECHNIQUE

### 2.1. General description of the FEA modelling

In the authors' recent studies, numerical models considering CFST with localized pitting corrosion are established using the finite element platform ABAQUS [8], which are shown to be able to predict the performance of CFST with localized pitting corrosion under the axial compression scenario [9], the combined compression-bending scenario [10], and the lateral loading scenario [11].

A typical CFST prototype is adopted for the benchmark member, with a degree of volume loss $DoV$ of 7.5% ($DoV$=$V_p$/$V_s$, where $V_p$ and $V_s$ represent the gross volume of corrosion pits and that of the steel tube, respectively). The corrosion region is set as a single patch with a half-column length encircling the mid-height of the column, as shown in Figure 1. For the sake of simplicity, the shape of each corrosion pit, which is found to have a moderate effect on the strength deterioration [12], is set as a cylinder. Individual corrosion pits can be described by these four variables shown in Figure 1, randomly generated based on their statistical characteristics in the modelling process [9] as described in Figure 2. Shape-related variables of geometric characteristics include the diameter [$d_i$] and depth [$h_i$] of the pit. Distribution-related variables of distribution patterns include the radius angle [$\theta_i$] and the height [$z_i$] along the column. The overlap of pits is not considered for simplicity. A targeted corrosion state is benchmarked against the index $DoV$, i.e., if the current $DoV$ is less than the target value, the current pit is recorded as a valid one and the pit-generation process is repeated. This pit-generation process is terminated when the current $DoV$ is close enough to the target value, namely, within a 0.1% tolerance.

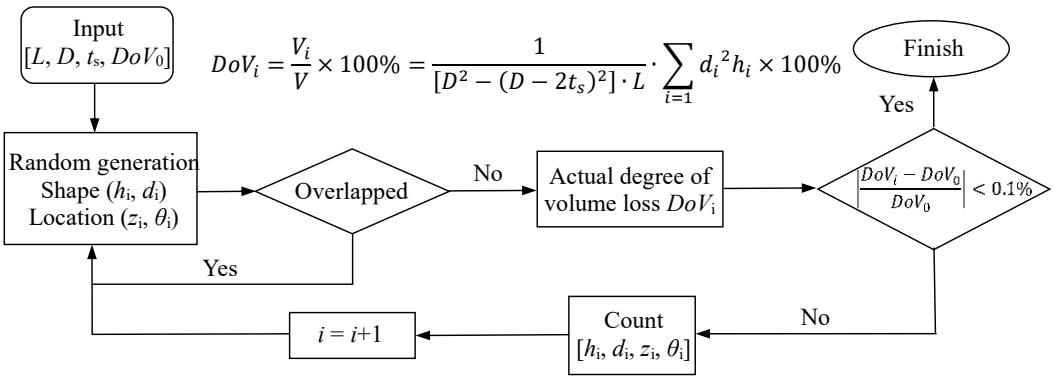


**Figure 2.** Illustration of the modelling process for random localized pitting corrosion

According to the mesh convergence study, the mesh size from the corrosion region to the end of the column is gradually increased from the average pit depth to $D$/15, where $D$ is the outer diameter of the steel tube [2]. In order to reflect the geometric characteristics of the corrosion pits and better explain the stress concentration around them, solid elements are used to simulate the steel tube [13]. The stress-strain models introduced by Han et al. [14] are utilized to determine the constitutive relation of the steel and the concrete components, which describe the composite action through a proposed confinement factor on concrete.

## 2.2. Verification of the FEA modelling

Verification of the proposed FEA modelling technique is conducted in terms of failure patterns, ultimate strength predictions, and strain development predictions. The simulated and observed failure patterns for pitted hollow steel tubes can be clearly observed, as shown in Figure 3. With the comparison between the predicted and measured strengths, the mean value and the standard deviation of the ratio indicate good agreement. Further details of model verification can be obtained from Li et al. [9,10,11]. The proposed FEA model is therefore considered capable of simulating steel tubular members subjected to localized pitting corrosion damage under the three typical scenarios.

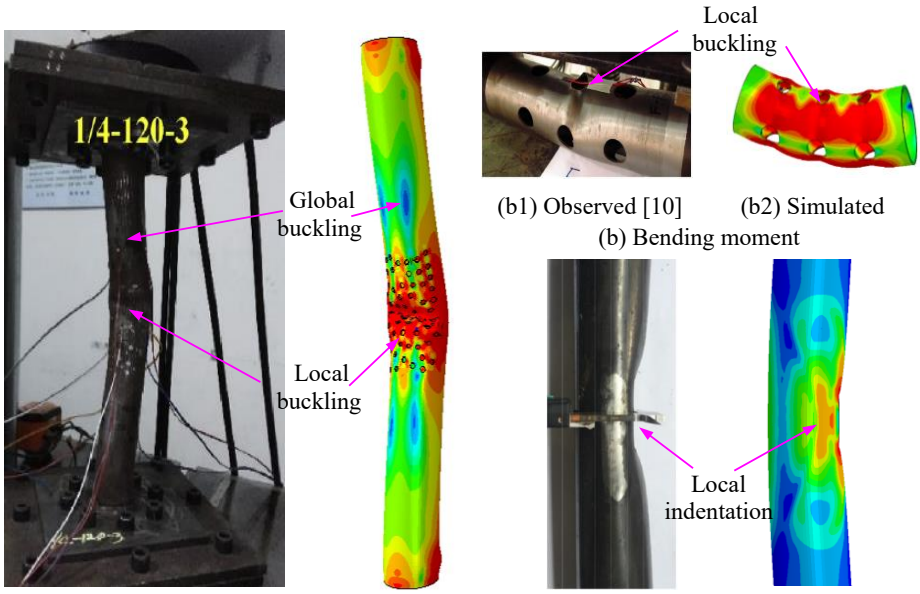


**Figure 3.** Model verification in terms of the observed and simulated failure modes

## 3. NUMERICAL INVESTIGATION

The above FEA models are adopted to conduct numerical investigations on the performance of pitted CFST. On the basis of numerical simulations, the influence of localized pitting corrosion on CFST under the three different loading scenarios is discussed in the following aspects.

### 3.1. Bearing capacity and energy absorption

As presented in Figure 4a, the decrease in the ultimate strength of the corroded steel-based columns is 12.6% and 20.5% for the CFST and hollow steel tube, respectively. According to Figure 4b, under compression-controlled failure, i.e., $e/D = 0.1$, the moment for pitted CFST is 52.8 kNm, 8.9% and 1.6% lower than its uncorroded and uniformly corroded counterparts, respectively. Under tension-controlled failure, i.e., $e/D = 3$, the moment for pitted CFST is 100.4 kNm, 26.2% and 15.5% lower than its uncorroded and uniformly corroded counterparts, respectively. Figure 4c presents the typical impact force history of CFST subjected to the lateral

impact load. During the peak stage OA, there is an obvious decrease, i.e., 15.7% in the peak load $F_p$ for pitted CFST. During the stable stage AB, the plateau load $F_0$ can be obtained, i.e., 701.1, 642.4, and 610.7 kN for CFST with no corrosion, uniform, and localized pitting corrosion, respectively. During the unloading stage BC, the duration time $t$ increases by 12.6% when localized pitting corrosion is considered.

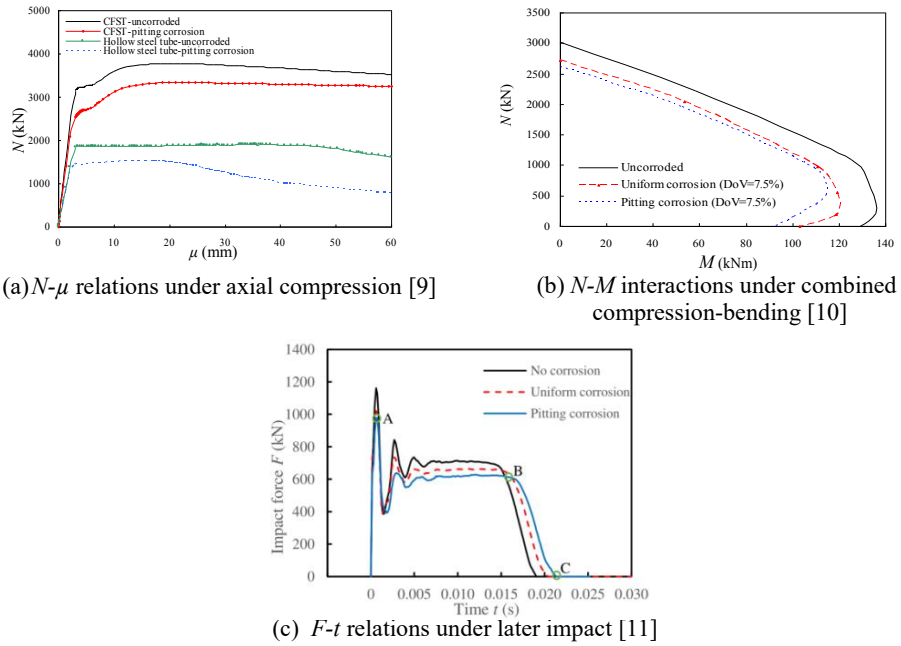


(a) $N$-$\mu$ relations under axial compression [9]

(b) $N$-$M$ interactions under combined compression-bending [10]

(c) $F$-$t$ relations under later impact [11]

**Figure 4.** Typical static and lateral impact behavior diagrams of CFST with localized pitting corrosion

### 3.2. Stress concentration and local buckling

As shown in Figure 3, stress concentration and local buckling can be found on all hollow steel tubes under different typical scenarios. Corrosion pits along the uneven surface of steel tubes not only reduce the effective steel tube thickness but also intensify the stress concentration around the pits [15]. For CFST columns subjected to localized pitting corrosion, stress concentration can result in early local buckling within the corrosion region, which can refer to Li et al. [9]. On the pitted steel tube with an eccentricity ratio of 0.1, the longitudinal stress distributes unevenly, while the maximum value corresponding to the ultimate state is 10.1% higher than that of the uncorroded counterpart [10].

### 3.3. Contact stress (p) between steel tube and concrete

The structural performance of CFST is highly correlated with contact behaviors of the steel-concrete interaction. The developments of the contact stress ($p$) in the compressive zone at the mid-height section for CFST are exhibited in Figure 5. The contact stress within the uncorroded and uniformly corroded counterparts is also shown in Figure 5.

As seen from Figure 5a, steel tubes with localized pitting corrosion begin to contact the core concrete when the axial displacement $\mu$ reaches 3.50 mm, which is 25.7% and 23.9% smaller than that of uncorroded and uniformly corroded counterpart, respectively. For CFST with an

eccentricity ratio of 0.5, displayed in Figure 5b, the contact stress is obtained when the lateral displacement reaches 5.38 mm, 49.5%, and 32.6% smaller than that of uncorroded and uniformly corroded counterparts, respectively. As exhibited in Figure 5c, as for the contact pressure at the impact loading area, the peak value is apparently lower than that of other counterparts. During the stable stage, significantly larger contact stress between the pitted steel tube and the concrete infill can be observed. More details regarding the development of contact stress can refer to Li et al. [9,10,11].

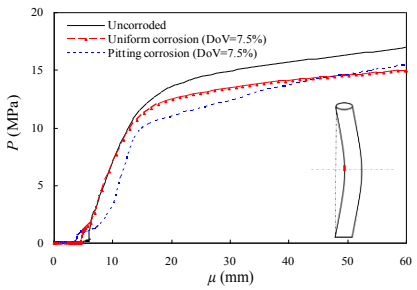


(a) $p$-$\mu$ curves under axial compression [9]

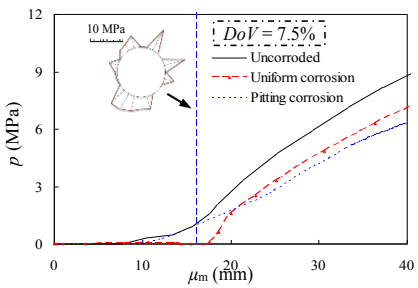


(b) $p$-$\mu_m$ curves under combined compression-bending [10]

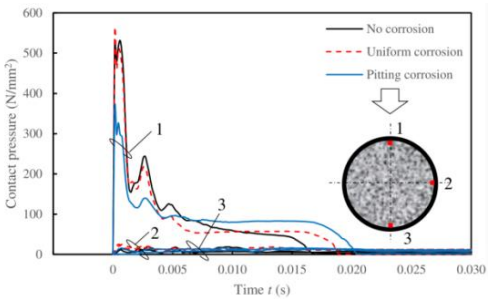


(c) $p$-$t$ curves under later impact [11]

**Figure 5.** Contact stress (p) at the mid-height section of CFST under typical loading scenarios

## 4. SIMPLIFIED DESIGN METHODS

On the basis of parametric analysis, the following factors evidently affect the behavior of pitted CFST, including the mean pit depth $h_m$, the confinement factor $\xi$, the steel ratio $\alpha_s$, etc. By modifying existing design formulas in standards, two simplified design methods are proposed as follows,

a. The statistics-based method: As shown in Figure 6, equivalent uniform corrosion is defined for the localized pitting corrosion as usual, where the effective tube thickness $t_{se}$ is obtained based on the statistical characteristics of the corrosion pits instead of the $DoV$, followed by $A_{se}$. Considering both precision and economic efficiency, the minimum pit depth for a 95% confidence interval is recognized as the equivalent tube thickness loss through trial-and-error learning. Thus, the statistics-based effective tube thickness $t_{se}$ and section modules $W_{sce}$ of a pitted CFST can be calculated as Eq. (2) and Eq. (3),

$$t_{se} = t_s - \Delta t_s = t_s - (h_m - 2\sigma) \tag{2}$$

$$W_{sce} = \pi \cdot {D_e}^3/32 = \pi(D - 2\Delta t_s)^3/32 \tag{3}$$

where $t_s$ and $\Delta t_s$ stand for the original tube thickness and the equivalent tube thickness loss due to localized pitting corrosion, respectively; $h_m$ and $\sigma$ stand for the mean value and the standard deviation of the normal distribution features adopted for corrosion pits, respectively.

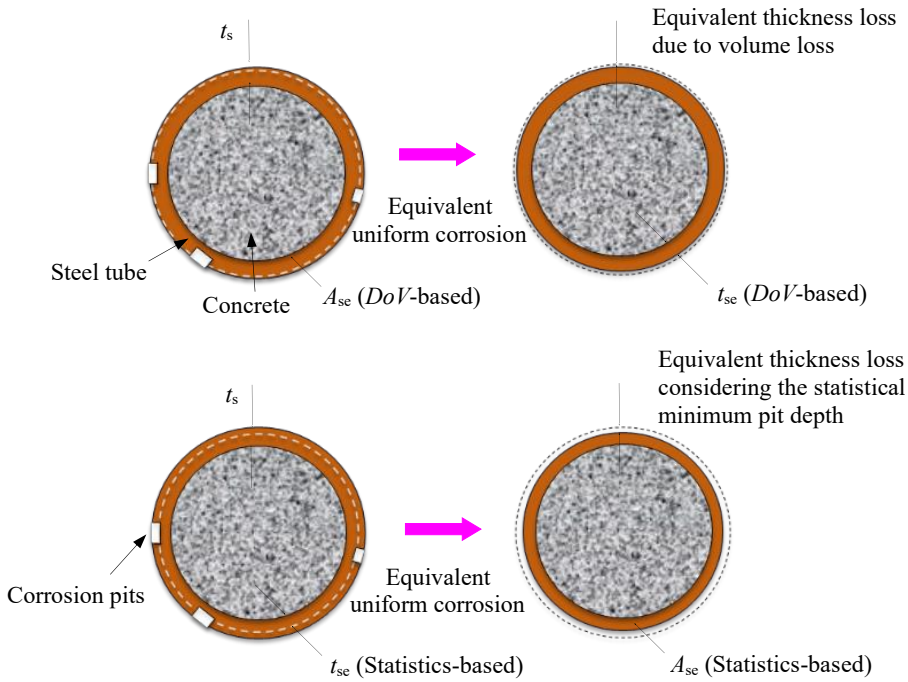


**Figure 6.** Schematic view of the DoV-based method and statistics-based method [9]

b. The confinement-specified method: To address the reduced steel tube cross-sectional area and the weakened confinement on concrete infill separately, the reduced effective steel tube cross-sectional area is determined using the degree of volume loss as expressed in Eq. (4). The above recognized statistics-based $\Delta t_s$ is utilized to calculate the decreased section modulus. Taking code GB/T 51446 (2021) for example, the predicted dynamic flexural capacity of CFST with localized pitting corrosion can be evaluated as Eq. (5) and Eq. (6).

$$A_{se} = (1 - DoV) \times A_s \tag{4}$$

$$M_{de} = R_{de} M_{ue} = 1.49 \cdot f(f_{ys}) \cdot f(\alpha_{se}) \cdot f(D_e) \cdot f(V_0) \cdot M_{ue} \tag{5}$$

$$M_{ue} = [1.1 + 0.48ln(\xi_e + 0.1)] \cdot [(1.14 + 1.02\xi_e) f_{ck}] \cdot W_{sce} \tag{6}$$

where $A_s$ is the original cross-sectional area of steel tube; $M_{de}$ and $M_{ue}$ are the dynamic and static flexural capacity of CFST, respectively; $f_{ck}$ is the characteristic compression strength of concrete infill; $R_{de}$ is the dynamic coefficient related to steel yield strength $f_{ys}$, steel ratio $\alpha_{se}$, diameter $D_e$ and the impact velocity $V_0$.

Figure 7 exhibits the comparison of the dynamic flexural capacity of localized pitted CFST

subjected to lateral impact load between the calculated and simulated results. The statistics-based method provides the average prediction of 0.710 and the standard deviation of 0.05, which are 0.882 and 0.04 as for the confinement-specified method. The latter method is testified to be effective in dynamic flexural capacity prediction.

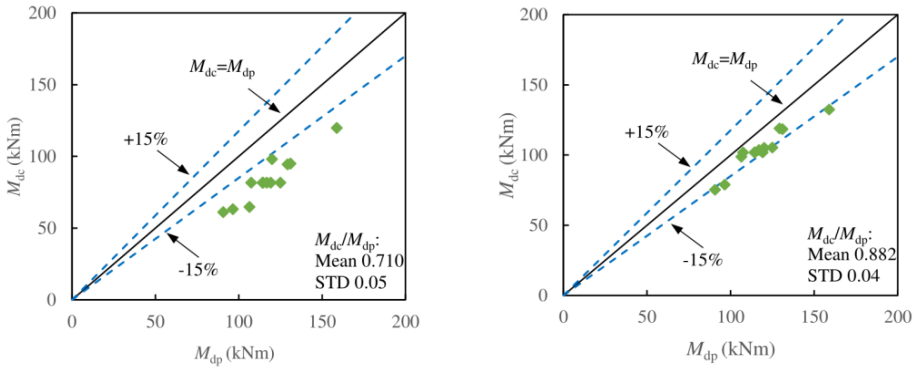


(a) Statistics-based method (b) Confinement-specified method

**Figure 7.** Comparison between predicted and calculated results of CFST with localized pitting corrosion [11]

## 5. CONCLUSION

The paper summarizes the static and lateral impact behaviour of CFST with no corrosion, uniform corrosion, and localized pitting corrosion, verified by reported test data. The analytical results reveal that compared with uniform corrosion, the deterioration of bearing capacity and energy absorption caused by localized pitting corrosion is more significant, which can be attributed to the stress concentration around corrosion pits, the increased susceptibility to local buckling, and the weakened confinement towards concrete. The proposed confinement-specified method can estimate the residual capacity with reasonable accuracy.

## ACKNOWLEDGMENTS

This work is financially supported by Shenzhen Science and Technology Program (No. RCYX20210706092044076). The financial support is highly appreciated.

**REFERENCES**

[1] Ellobody, E., Young, B., & Lam, D. (2006). Behaviour of normal and high strength concrete-filled compact steel tube circular stub columns. *Journal Of Constructional Steel Research*, 62(7), 706-715.

[2] Tao, Z., Wang, Z.B., & Yu, Q. (2013). Finite element modelling of concrete-filled steel stub columns under axial compression. *Journal Of Constructional Steel Research*, 89, 121-131.

[3] Han, L.H., Hou, C., & Wang, Q.L. (2012). Square concrete filled steel tubular (CFST) members under loading and chloride corrosion: experiments. *Journal Of Constructional Steel Research*, 71, 11-25.

[4] Wang, Y.H., Wang, Y.Y., Hou, C., Zhou, X.H., Deng, R., Lan, Y.S., Luo, W., & Kong, W.B. (2020). Combined compression-bending-torsion behaviour of CFST columns confined by CFRP for marine structures. *Composite Structures*, 242, Article 112181.

[5] Rivas, D., Caleyo, F., Valor, A., & Hallen, J.M. (2008). Extreme value analysis applied to pitting corrosion experiments in low carbon steel: comparison of block maxima and peak over threshold approaches. *Corrosion Science*, 50, 3193-3204.

[6] Valor, A., Caleyo, F., Alfonso, L., Rivas, D., & Hallen, J.M. (2007). Stochastic modelling of pitting corrosion: a new model for initiation and growth of multiple corrosion pits. *Corrosion Science*, 49, 559-579.

[7] Bhandari, J., Khan, F., Abbassi, R., Garaniya, V., & Ojeda, R. (2015). Modelling of pitting corrosion in marine and offshore steel structures-a technical review. *Journal of Loss Prevention in the Process Industries*, 37, 39-62.

[8] Dassault Syst`emes Corp. (2016) *ABAQUS, ABAQUS Standard User's Manual.* Version 6.16, Providence, RI, USA.

[9] Li, G., Hou, C., Shen, L.M., & Yao, G.H. (2022). Performance and strength calculation of CFST columns with localized pitting corrosion damage. *Journal Of Constructional Steel Research*, 188, Article 107011.

[10] Li, G., Hou, C., & Shen, L.M. (2022). Combined compression-bending performance and design of CFST with localised pitting corrosion. *Journal of Constructional Steel Research*, 192, Article 107247.

[11] Li, G., Hou, C., Shen, L.M., & Hou, C.C. (2023). Lateral impact behaviour of concrete-filled steel tubes with localised pitting corrosion. *Steel and Composite Structures*, 47(5), 615-631.

[12] Wang, R.H., & Shenoi, R.A. (2019). Experimental and numerical study on ultimate strength of steel tubular members with pitting corrosion damage. *Maine Structures*, 64, 124-137.

[13] Jin, D.Y.D., Hou, C., & Shen, L.M. (2021). Effect of welding residual stress on the performance of CFST tubular joints. *Journal of Constructional Steel Research*, 184, Article 106827.

[14] Han, L.H., Yao, G.H., & Tao, Z. (2007). Performance of concrete-filled thin-walled steel tubes under pure torsion. *Thin-Walled Structures*, 45(1), 24-36.

[15] Guo, L.H., Huang, H.J., Jia, C., & Romanov, K. (2020). Axial behaviour of square CFST with local corrosion simulated by artificial notch. *Journal of Constructional Steel Research*, 174, Article 106314.

# THE PERFORMANCE OF CABLE CLAMP SYSTEMS IN SUSPENSION BRIDGES CONSIDERING BOLT FRACTURE UNDER VEHICLE FIRE

*Rujin Ma[1], Huseyin Saglik[2], Zichao Pan[3] and Airong Chen[4]*

[1] Associate Professor, College of Civil Engineering, Tongji University, rjma@tongji.edu.cn.

[2] Ph.D. Candidate, College of Civil Engineering, Tongji University, hsaglik@tongji.edu.cn.

[3] Associate Professor, College of Civil Engineering, Tongji University, z.pan@tongji.edu.cn.

[4] Professor, College of Civil Engineering, Tongji University, achen@tongji.edu.cn.

**Corresponding Author: Huseyin Saglik, Ph.D. Candidate**

College of Civil Engineering, Tongji University, 200092 Shanghai, China

**Email:** hsaglik@tongji.edu.cn

## ABSTRACT

Cable clamp systems play an essential role in force transferring and stability of suspension bridges by linking various key elements such as main cables and vertical hangers. Cable clamps consist of multiple high-strength bolts, steel clamps, main cable, hanger rope, and a bolted pin connection linking the clamps and hanger. Failure in one of these may cause the stability of suspension bridges to deteriorate, especially in fire accidents. This study numerically investigates the performance of cable clamp systems adopted from a real suspension bridge under vehicle fire. The structural and heat transfer analysis is performed in Abaqus considering ductile fracture of the bolts at elevated temperatures. The effects of fire intensity and tension load in the cables on the fire performance are investigated by adopting different fire locations in the longitudinal direction of the suspension bridge. The findings are discussed from the points of local performance of the connection and the overall behavior of the suspension bridge.

***Keywords:*** *Fire, Suspension Bridge, Cable Clamp, Ductile Fracture, Abaqus, Finite Element Method.*

## INTRODUCTION

Fire accidents significantly endanger the stability of not only residential buildings but also bridges [1]. Among different types of bridges, cable-stayed and suspension bridges are particularly important in modern transportation networks. Due to rapid industrialization worldwide, the possibility of fire accidents on these types of bridges caused by transporting hazardous petrochemicals has been increasing progressively. Recent fire accidents on

suspension bridges [2,3] have shown that the main cable and suspenders, as well as the suspender anchorages that provide force transfer between these members, can be damaged or even collapse under high temperatures. Cable clamp systems play an essential role in force transferring and stability of suspension bridges by linking main cable and suspenders. Since the clamp systems consist of multiple pre-tensioned high-strength bolts, pin connection, clamps, main cable, suspender, and suspender anchorages, the failure in one of these may cause the stability of suspension bridges to deteriorate, especially in fire accidents. In this study, a sequentially coupled thermo-mechanical analysis was performed to examine the performance of cable clamp systems under a tanker fire accident.

# CASE STUDY

## Engineering Background

The investigated bridge has a main span of 2,300 m. A total of 142 suspenders providing the connection between the deck and two main cables are located with 16 m intervals in the main span. The deck consists of a total of 8 lanes in two ways with two emergency lanes. The total width of the deck is 39.5.

Fig. 1 illustrates the details of cable clamp, main cable, the fork socket, and suspenders. The upper and lower parts clamp the main cable with the help of pre-tensioning Grade 10.9 high-strength bolts. The main cable has a 1106 mm diameter. Grade 2060 and 1770 wires are used to constitute parallel wire strands in the main and suspender cable sections, respectively. The vertical loads from the deck are transmitted by hot-cast fork sockets to the lower clamp by two high-strength bolts having diameters of 150 mm. The cables of the suspenders are embedded in zinc copper alloy.

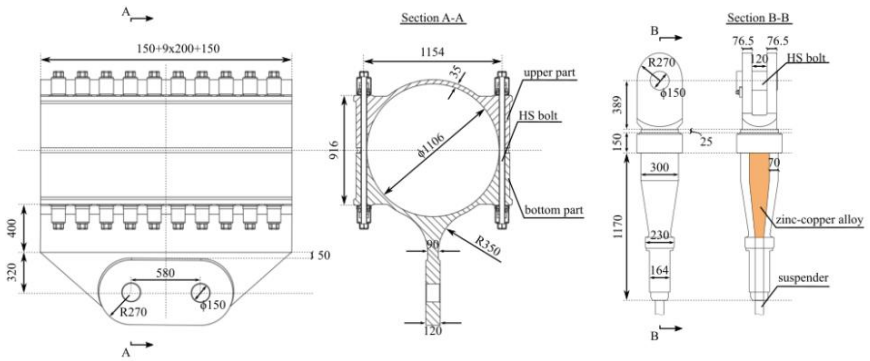


**Figure 1**. Cable clamp system details, dimensions in mm.

# DETERMINATION OF CRITICAL CLAMP SYSTEMS

## Bridge fire scenario and parameters

A tanker-induced fire scenario was considered in the lanes closest to the cable clamp systems. The tanker fire parameters were adopted from Ma et al. [4] without considering the wind effect.

The tanker fire dimensions were considered as 10.4 m × 12 m in transverse and longitudinal directions of the suspension bridge, respectively with the burning time of 120 min. The temperature-time curves with respect to different heights and normalized maximum temperature values are given in Fig. 2.

## Heat transfer between tanker fire and plane surface

A heat transfer analysis was performed between the fire source and the plane in Abaqus as adopted before [5,6]. Two parts were modelled in Abaqus as shell parts for the tanker fire part and the affected plane surface at the level of the suspenders and main cable. The tanker fire was modelled in a cuboid shape that have the dimensions of 10.4m x 12 m x 40 m. The dimensions of the affected plane surface are as 2 and 1.5 times larger than the tanker dimension in width and height of the tanker flame, respectively. The model is shown in Fig. 3a. DS4 element type was assigned to both part with the global mesh size of 0.8 m [7]. The idealized temperature-time curves with respect to fire height (Fig.2) were defined in the tanker part. Convective and open cavity radiation transfer modes were defined in the heat transfer with surface emissivity coefficients of 1.0 and 0.85 [6,8] for the flame and affected surface, respectively. A convective heat transfer coefficient of 50 W/m2°C was assigned for the fire-exposed surface as per EN 1991-1-2 [9]. Fig. 3b illustrates the temperature distribution on the plane surface after 120 min of burning. While the maximum temperature is 1045 °C on the tanker fire model, the maximum resultant temperature on the affected plane surface is about 570 °C.

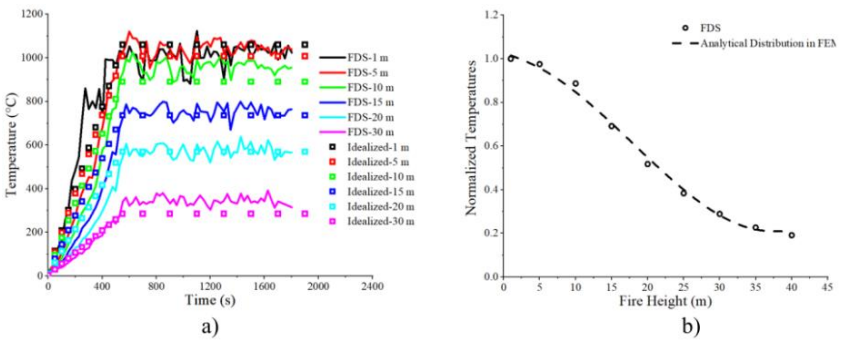


**Figure 2.** a) Time-temperature curves and b) normalized maximum temperatures with respect to fire heights for tanker fire.

## Critical cable clamps

Critical temperature has been determined as 300°C based on the strength reduction change of the used materials, recommendation (300°C) by PTI DC45.1-12 [10], and the melting temperatures of HDPE (330-350°C), and zinc-copper alloy (420-460°C). The strength reductions for Grade 10.9 bolts, Grade 2060 wires for the main cable, Grade 1770 wires for suspenders, and structural steel were adopted from Saglik et al. [11], Chen et al. [12], Zheng et al. [13], and EN 1993-1-2 [14], respectively. The grey area in the Fig.3b shows the critical temperature area in which the temperature is larger than 300 °C. The critical temperature of the tanker fire reached 15 m in the vertical direction. Accordingly, 26 cable clamps can be

attributed as critical in the suspension bridge examined as shown in Fig. 4. Three cable clamps were selected to investigate further.

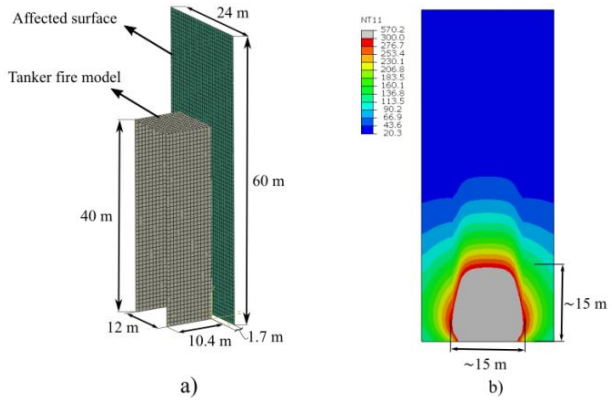


**Figure 3.** Finite element model of the heat transfer analysis between tanker fire and plane surface.

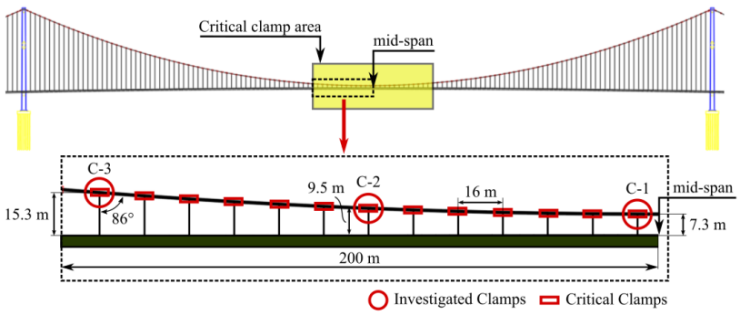


**Figure 4.** Critical clamp area and chosen clamp systems to be investigated.

## FINITE ELEMENT MODEL

The analysis was simply divided into two main stages: heat transfer and structural analysis. Structural analysis was divided into three steps: pre-loading of the high-strength bolts, tension loading of the cables, and thermal loading. C3D8R elements were used to mesh all parts. The densities of 0.01 m, 0.02 m, and 0.05 m were assigned to high-strength bolts, suspenders, and main cables, respectively, with the general density of 0.04 m. The general assembly of the cable clamp system is given in Fig. 5. The interaction between zinc-copper alloy and suspender was ensured by defining 'embedded constraint' to reflect the realistic behaviour. In the first step, pre-tension loads (0.7Fu) were applied to the high-strength bolts connecting the upper and lower clamps. In the second step, tension forces of $5.94\times10^8$ N and $2.51\times10^6$ N were applied to reference nodes belonging to the main cable and suspenders, respectively. In the thermal step, the nodal temperatures obtained from heat transfer analysis were transferred to the structural analysis while all loads and boundary conditions were kept same as previous step. In heat transfer analysis, DC3D8R elements were used to mesh the parts. The nodal temperature-

time changes have been adopted from plane surface temperature distributions and applied to the half of the clamp system surface.

## Material properties

Stress-strain relationships for Grade 10.9 bolts were adopted from [11] and [15] before and after necking. Ductile fracture definitions were defined from [15]. Stress-strain curves until ultimate stress for Grade 2060 wires (main cable), Grade 1770 (suspender), and zinc-copper alloy were adopted from [12], [13], and [16], respectively, at elevated temperatures. An elastic perfectly-plastic model was used for clamps and fork sockets, ZG20Mn steel. After ultimate stress, true curves were defined as the lower bound proposed by Ling et al. [17]. The fundamental mechanical properties at ambient temperature are presented in Table 1. The density of steel and zinc-copper alloy was adopted as 7850 kg/m$^3$ and 6930 kg/m$^3$ [18]. Thermal properties of steel and zinc-copper alloy were taken in accordance with [14] and [18], respectively. A thermal expansion coefficient of 1.4 $\times 10^{-5}$ [19] was used for steel members.

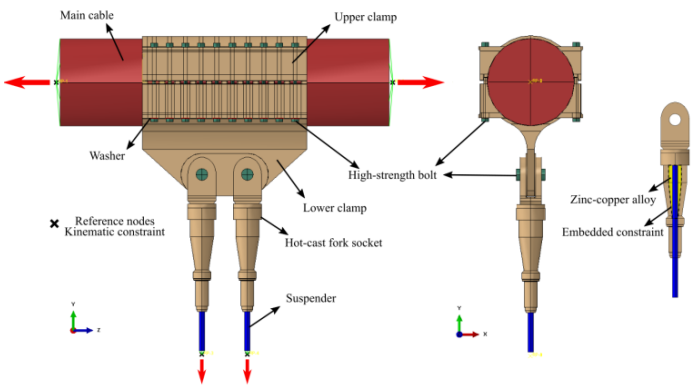


**Figure 5.** Cable clamp system assembly in Abaqus.

**Table 1.** Mechanical properties of the all parts in clamp system at ambient temperature.

| Material | Grade 10.9 | Grade 2060 | Grade 1770 | Zinc-copper alloy | ZG20Mn |
|---|---|---|---|---|---|
| E (GPa) | 210 | 197 | 204 | 14 | 210 |
| Fy (MPa) | 900 | 2058 | 1634 | 125 | 295 |
| Fu (MPa) | 1000 | 2156 | 1803 | 175 | - |

# RESULTS

## Results of the heat transfer analysis

Heat transfer results are given for only hot-cast fork socket since the melting temperature can be reached for zinc-copper alloy which can cause the loss of bonding with suspenders. For the sake of brevity, the temperature distribution for C-1 is investigated herein. The general temperature distribution pattern is similar in all cases.

### *Temperature distribution on hot-cast fork socket*

Here, the temperature distribution of the hot-cast fork socket is investigated including zinc-copper alloy. As mentioned before, the melting temperature of the alloy is approximately 440 °C. Since the melting of the alloy was not explicitly modelled here, it is assumed that the melting, consequently the failure of the bonding occurs when the temperature of any section of the alloy reaches the value of 440 °C. Fig. 6 shows the temperature distribution of the socket and alloy part with respect to time. Since the hot-cast socket is closer to the tanker fire source compared to the other shown parts, higher temperatures are observed for this part. The temperature gradient between the two sides of the socket is considerable during the fire which can cause different thermal expansion. After an hour, the maximum temperature of the alloy reaches about 400 °C. The critical time when the critical alloy section attains melting temperature is between 60-90 min, specifically about 75 min for C-1. The time when the melting alloy occurs is found as 100 min for C-2. In C-3, the temperature distribution did not reach the melting temperature of the alloy. It is expected that the bonding between the alloy and suspender can deteriorate completely within the obtained times.

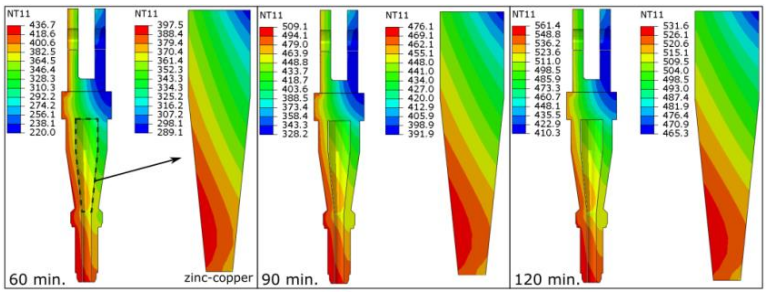


**Figure 6.** Temperature distribution change on the socket and zin-copper alloy for C-1 with respect to time.

## Results of the structural analysis

### *Structural response under pre-tension and cable tension loads at ambient temperature*

The first two steps of the structural analysis, pre-tension, and cable tension load steps, are the same for all cases. The pre-tension load was sufficiently achieved at the end of pre-tension step. The stresses on the upper and lower surfaces of the clamps are higher than the other parts due to the pre-tension effect. The stress exceeds about 120 MPa which is well below the yield strength of steel material. Under cable tension and gravity loads, the stress distribution as well as the interaction of the components become more sophisticated. The Mises stress of the main cable is around 620 MPa under tension load while the maximum Mises stress of high-strength pin bolts is 220 MPa, which is well below the yield stress. The maximum Mises stress in the suspenders under tension loads is found as 770 MPa. The design stress corresponds to 50% of the suspender yield stress at ambient temperature. The suspender is highly suspicious of failure considering the obtained maximum temperature in heat transfer analysis.

### *Structural response under tanker fire*

Here, the structural response of only Case-1 is evaluated at the failure time for the page limitation. However, the stress distributions are similar for other cases.

*Case-1*

Fig. 7a shows the Mises stress distribution on the clamp system at about 63 min after tanker fire initiation. In 63 min of tanker fire, the necking of the suspender cable was observed and the analysis stopped. The necking area of the suspender is seen in Fig. 7b. The failure of the suspender is expected based on the high-temperature field and higher stress distribution under tensile load to yield strength ratio comparing other components shown in previous steps. Also, it is seen that plastic deformation occurs in the alloy section. In the previous section, the estimated time of alloy melting was found as about 75 min. The first hour of the tanker fire seems highly important for the structural safety of suspension bridges based on the obtained failure times for suspender necking and the alloy melting. Small inelastic deformations are seen in clamps, bolt heads, and zinc copper alloy.

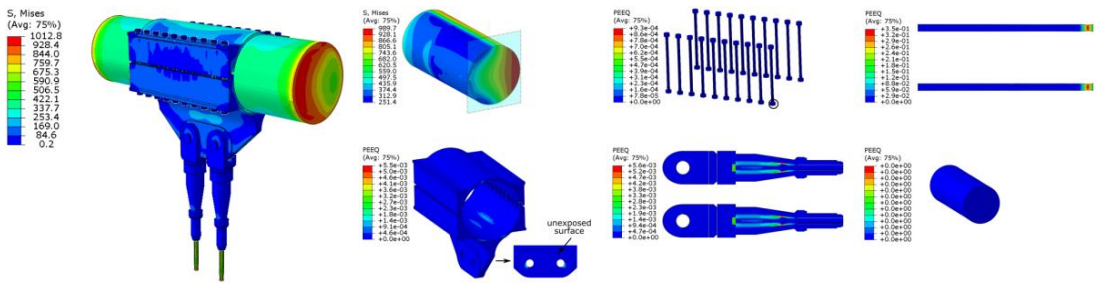


a) b)

**Figure 7.** a) Stress distribution of the clamp system, and b) Equivalent plastic strain of each component at about 63 min for C-1.

*Case-2*

Even though the general pattern is similar to the C-1, the plastic deformations are smaller due to lower temperatures. No plastic strain is observed in pre-tensioned bolts and pinned bolts. The failure occurred as suspender cable necking within about 80 min of the fire. From the previous section, the alloy melting was estimated to occur within 100 min. Therefore, the failure of melting alloy and suspender necking is also found as a predicted failure of the clamp system.

*Case-3*

In C-3, no failure in the components has been detected. However, localized small inelastic deformations have been observed in suspension cable and zinc-copper alloy.

## Investigation of tension force change in high-strength bolts

The pre-tension load changes in bolt mid-sections are illustrated in Fig. 8 by extracting the tensile force from two bolts chosen at both fire-exposed and unexposed sides. the tension load decreases by almost 40 percent to about 500 kN due to the transverse deflection of the main cable under tensile load caused by Poisson's rule. During tanker fire, the tensile load begins to be different depending on the location of the cable system and bolts with respect to fire. In

general, the tension loads obtained from the bolts located on the side not exposed to fire increase over time due to load transfer shifts. Also, thermal expansion contributes to the pre-tension loss at the exposed face. The tension loads in C-1 and C-2 are very similar for the bolts on both sides. While the tension loads decrease approximately by 58 percent for the bolt located at the side exposed to fire, the tension loads of the bolts at the unexposed side increase about by 30 percent in C-1 and C-2. The force changes for C-3 are slighter than the other cases due to lesser fire exposure. The decrease in pretension load can cause the decrease the friction between clamps and main cables. It can further cause sliding of the clamps and should be investigated further.

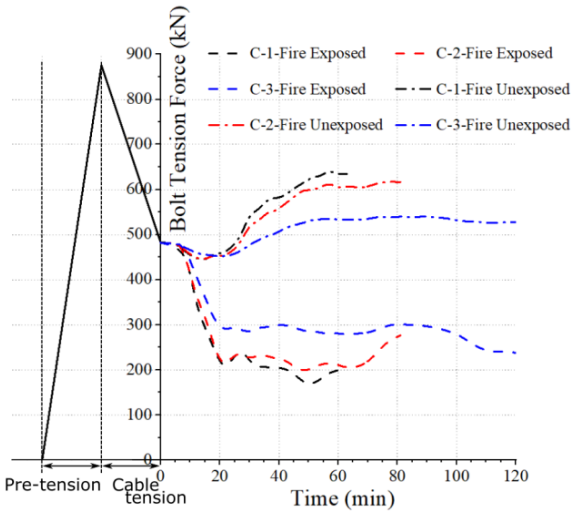


**Figure 8.** Bolt tension force change with respect to time.

# CONCLUSION

The following conclusions can be drawn from the study:

- The necking of the suspender and melting of the zinc-copper alloy are found as the dominant failure modes. The failure can occur within an hour.
- There are some localized plastic deformations observed in upper and lower clamps and pre-tensioned bolts.
- The fire performance of the components, except for the alloy, highly depends on the loading level at ambient temperature. However, the melting of the alloy can be considered as unavoidable so the appropriate thermal insulations should be implemented.
- The pre-tension of the high-strength bolts can decrease with tensile load application and during the fire. A further study should be conducted.

The suspension bridge is further evaluated by the importance factor approach developed by Kodur and Naser [20]. The importance factor matches the current study. As also authors suggested, fire protection systems would be beneficial to improve the fire safety.

## ACKNOWLEDGMENTS

R. Ma, H. Saglik, and A. Chen and acknowledge financial support from the Key Projects of the National Natural Science Foundation of China (grant 52238005).

## REFERENCES

[1] Saglik, H., Chen, A., & Ma, R. (2022). Performance of bolted splice connection in I-girder composite bridges under tanker fire. Journal of Constructional Steel Research, 199, 107590.

[2] Giuliani, L., Crosti, C., & Gentili, F. (2012, July). Vulnerability of bridges to fire. In Proceedings of the 6th International Conference on Bridge Maintenance, Safety and Management (pp. 8-12).

[3] Yuan, A., Yang, T., Xia, Y., Qian, L., Dong, L., & Jin, X. (2022). Replacement of the fire-damaged long suspenders of the Runyang Suspension Bridge. Structural Engineering International, 32(4), 484-490.

[4] Ma, R., Cui, C., Ma, M., & Chen, A. (2021). Numerical simulation and simplified model of vehicle-induced bridge deck fire in the full-open environment considering wind effect. Structure and Infrastructure Engineering, 17(12), 1698-1709.

[5] Quiel, S. E., Yokoyama, T., Bregman, L. S., Mueller, K. A., & Marjanishvili, S. M. (2015). A streamlined framework for calculating the response of steel-supported bridges to open-air tanker truck fires. Fire Safety Journal, 73, 63-75.

[6] Ma, R., Cui, C., Ma, M., & Chen, A. (2019). Performance-based design of bridge structures under vehicle-induced fire accidents: basic framework and a case study. Engineering Structures, 197, 109390.

[7] da Silva Santos, F., & Landesmann, A. (2014). Thermal performance-based analysis of minimum safe distances between fuel storage tanks exposed to fire. Fire safety journal, 69, 57-68.

[8] Cui, C., Chen, A., & Ma, R. (2020). Stability assessment of a suspension bridge considering the tanker fire nearby steel-pylon. Journal of Constructional Steel Research, 172, 106186.

[9] EN 1991-1-2. (2002). Eurocode 1: Actions on Structures - Part 1-2: General Actions - Actions on Structures Exposed to Fire, European Committee for Standardization (CEN), Brussels.

[10] PTI (Post-Tensioning Institute). (2012). PTI DC45.1-12: Recommendations for stay-cable design, testing, and installation. Phoenix, AZ: PTI.

[11] Saglik, H., Etemadi, A., Chen, A., & Ma, R. (2024). Constitutive model and mechanical properties of grade 8.8 and 10.9 high-strength bolts at elevated temperatures, Journal of Structural Engineering, DOI: 10.1061/JSENDH/STENG-12629

[12] Chen, W., Shen, R., Chen, X., Qi, D., & Yang, J. (2024). High-temperature mechanical properties and failure modes of UHSS wire for cable-supported bridge. Journal of Constructional Steel Research, 212, 108292.

[13] Zheng, W., Hu, Q., & Zhang, H. (2007). Experimental research on the mechanical property of prestressing steel wire during and after heating. Frontiers of Architecture and Civil Engineering in China, 1, 247-254.

[14] EN 1993-1-2. (2005). Eurocode 3: Design of Steel Structures - Part 1-2: General Rules - Structural Fire Design. European Committee for Standardization (CEN), Brussels.

[15] Saglik, H., Chen, A., & Ma, R. (2024). Ductile fracture of high-strength bolts under combined actions at elevated temperatures. Journal of Constructional Steel Research, 213, 108437.

[16] Huang, L., Du, Y., Qi, H. H., & Wang, Y. (2023). Mechanical properties and constitutive model of filling medium in hot casting socket at elevated temperatures. Construction and Building Materials, 408, 133791.

[17] Ling, Y. (1996). Uniaxial true stress-strain after necking. AMP Journal of technology, 5(1), 37-48.

[18] Du, Y., Zhu, Y., Jiang, J., & Li, G. Q. (2019). Transient temperature distribution in pre-tensioned anchors of cable-supported structures under ISO834 fire. Thin-Walled Structures, 138, 231-242.

[19] GB 51249-2017. (2017). Code for fire safety of steel structures in buildings, Standardization Association Professional Committee of Steel, China Planning Press.

[20] Kodur, V. K. R., & Naser, M. Z. (2013). Importance factor for design of bridges against fire hazard. Engineering Structures, 54, 207-220.

# SEISMIC PERFORMANCE OF A HYBRID SYSTEM OF HOT-ROLLED STEEL FRAME AND STEEL SHEATHED COLD-FORMED STEEL SHEAR WALL

*Shen Liu*[1]

[1] Assistant professor, Xi'an University of Architecture and Technology, liushen@xauat.edu.cn

**Corresponding Author: Shen Liu, PhD.**

Xi'an, Shaanxi Province, China, 710055

**Email:** liushen@xauat.edu.cn

**ABSTRACT**

A novel hybrid system consisting of the steel frame and the steel-sheathed cold-formed steel (CFS) shear wall is proposed to improve the seismic performance of CFS shear walls. The cyclic test was carried out on three full-size specimens. First, the hysteretic curves, energy dissipation, ductility coefficient, and column strain were obtained. Then, the effects of vertical load and screw spacing on the seismic performance of the specimens were analysed. The results show that: The connection between the frame and the shear wall is reliable, and both systems exhibit coordinated deformation under loading. The shear capacity of the proposed system ranges from 121.3kN to 136.7kN, with a ductility coefficient between 1.99 and 2.75. Decreasing the screw spacing of the central stud in CFS shear walls and increasing vertical loads can enhance the specimen shear capacity. The hybrid system of frame and steel-sheathed CFS shear wall exhibits excellent seismic performance, making it applicable for multi-story steel residential housings.

***Keywords:*** *Seismic performance, Cold-formed steel, Hot-rolled steel, Numerical modelling.*

## 1. INTRODUCTION

Cold-formed steel (CFS) structures are extensively used across many countries and are well-supported by various design specifications [1]. With the progression of urbanization, the construction of mid-rise CFS structures has significantly increased in the 21st century. This trend towards taller buildings demands higher shear and compressive capacities. To meet these requirements, several innovative solutions have been proposed, including steel-sheathed CFS shear walls, strap-braced CFS shear walls, and reinforced concrete CFS shear walls.

The steel-sheathed CFS shear wall system has been extensively applied and studied due to its superior shear performance. Balh et al. [2] enhanced the design of steel-sheathed CFS framed

shear walls for inclusion in North American standards, utilizing a database of monotonic and reversed cyclic shear wall tests from research programs in Canada and the US. Yu [3][4] conducted a series of tests on steel sheet-sheathed CFS shear walls, considering variables such as steel sheathing thickness, aspect ratio, and framing web depth. These studies established the nominal and seismic shear strengths of CFS shear walls for design purposes. Mohebbi et al. [5] compared the performance of CFS shear walls with single and double-sided steel sheathing. The results indicated that walls with double-sided sheathing exhibited greater energy dissipation, shear strength, and elastic stiffness compared to those with single-sided sheathing. However, the use of sheathing on both sides necessitates precautions to avoid chord stud failure. Iman Shamim modeled dynamic tests of steel-sheathed CFS framing in OpenSees using Pinching 04 hysteretic material [6]. The results demonstrated that these advanced models could accurately reproduce the shear strength, displacement time history, and hysteretic response of the structures.

In addition, some scholars have adopted steel columns to strengthen CFS systems. Sharafi et al. [7] proposed a hybrid solution for CFS structures, which replaces some studs with hot-rolled steel (HRS) frame in order to achieve higher capacity. The CFS part resists the major portion of gravity loads, while the HRS frame bears most of the lateral load, results in an improved performance. A new hybrid CFS shear wall system with an HRS truss skeleton is proposed by Ronagh et al. [8] in order to improve the lateral behavior of lightweight steel frames, the results showed that employing the truss configuration for one side of the light steel walls can significantly enhance the energy absorption, compared to the traditional CFS walls. The low strength-to-weight ratio of hybrid walls makes them a practical solution for mid-rise lightweight constructions. Ye et al. [9-10] proposed shear walls with concrete-filled rectangular steel tube columns as end studs and conducted cyclic loading tests. The results indicated that the shear strength of the wall was improved due to the concrete core in the reinforced end studs, which reduced screw tilting. Dao et al. [11] investigated the seismic performance of a new CFS system. This system includes floor trusses, open panels, V-braced panels, columns, and connections. Both test results and numerical analysis showed that the system exhibits good ductility and performs well at four stories, making it a viable option for mid-rise construction in seismic regions.

Referring to existing systems, a novel steel-sheathed cold-formed steel shear wall system reinforced by the steel moment frame was proposed. The moment frame can constrain the shear wall and enhance its lateral performance. Both the moment frame and CFS shear wall bear vertical and horizontal load so that the section size of columns is smaller than the normal moment frame. The smaller column dimension will increase the interior space, especially in residential buildings. Furthermore, the proposed system features dual lateral-resisting mechanisms, offering improved safety and resilience in the face of seismic events.

In this paper, a cyclic test of the proposed system was conducted. The failure modes, hysteretic curves, and strain of the specimens were obtained. The effects of screw spacing and vertical load were analyzed, and the strengthening effect of this novel system was compared to that of the traditional CFS shear wall system.

# 2. EXPERIMENTAL PROGRAM

## 2.1 Test specimens

Three prototypes were developed for the hybrid system, comprising steel frames and CFS shear walls with steel sheathing. These prototypes were dimensioned in accordance with typical requirements for multi-story residential buildings, as illustrated in Figure 1. The CFS shear walls with steel sheathing measure 2.4 meters in width and 3.3 meters in height. The framing utilizes C-shaped CFS channels for studs, characterized by Q345 grade strength and a 1.8 mm thickness. The channels' cross-sections measure 150 mm × 51 mm × 12 mm (web length × flange length × lip length), while the tracks' cross-sections are 152 mm × 51 mm (web length × flange length). Each wall is sheathed on one side with two steel sheets, each measuring 3500 mm × 1200 mm × 0.8 mm (length × width × thickness). The design features back-to-back double studs at the boundaries and single studs as standard wall studs, spaced 600 mm apart. Connections within the wall are secured with self-tapping screws, with a 300 mm spacing for back-to-back studs and a 100 mm spacing for attaching the steel sheet edges to the wall framing.

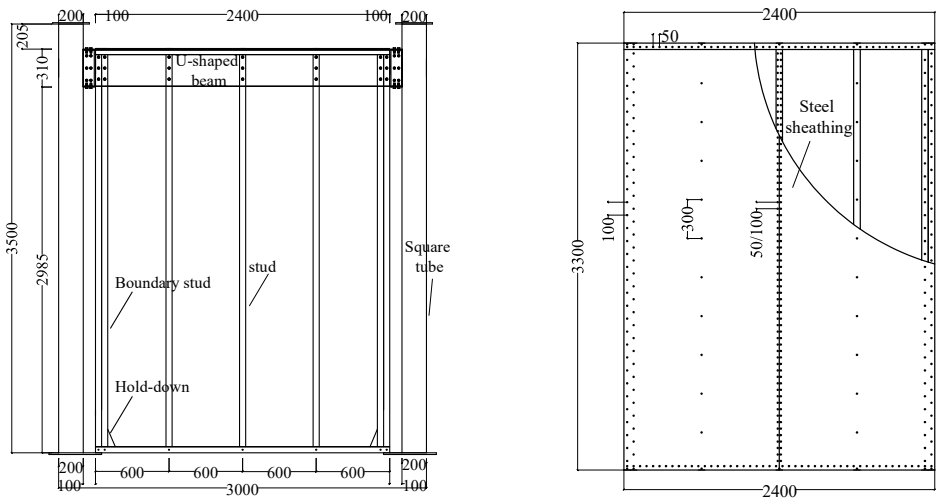


(a) Steel frame (b) Steel sheathed CFS shear wall

**Figure 1**. Dimensions of the frame and steel sheathed CFS shear wall.

The steel frame comprises columns, beams, and beam-column joints. The columns are fabricated from hot-rolled Q345 square steel tubes with a cross-section of 200mm × 200mm × 5mm. The beams, made of hot-rolled Q345 steel in a U-shape and positioned on both sides, have a cross-sectional dimension of 300mm × 60mm × 4mm. The beam-column joints feature a symmetrical U-shaped design, with one end welded to the square tube and the other connected to the frame beam via M12 bolts. The details of the beam-column joint are depicted in Figure 2.

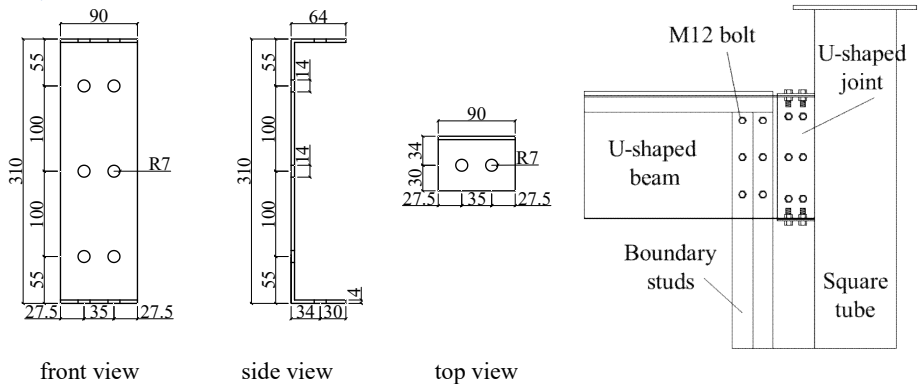


**Figure 2.** Dimensions and details of the column-beam joint.

The design parameters of the steel frame-steel sheathed CFS shear wall specimens are delineated in Table 1, incorporating two primary variables: the minimum screw spacing and the applied vertical load. The specimens are designated according to the format "S-(minimum screw spacing)-(vertical load)." Specifically, a vertical load of 120kN indicates the first floor in low-rise residential structures, whereas a vertical load of 240kN corresponds to the first floor of multi-story residential structures.

**Table 1.** Design parameters of the specimens

| Name | Frame dimensions | Shear wall dimensions | Beam thickness | Column thickness | Minimum screw spacing | Vertical Load |
|---|---|---|---|---|---|---|
| | H × L (m) | H × L (m) | (mm) | (mm) | (mm) | (kN) |
| S-100-120 | 3.5×3.0 | 3.3×2.4 | 4 | 5 | 100 | 120 |
| S-50-120 | 3.5×3.0 | 3.3×2.4 | 4 | 5 | 50 | 120 |
| S-50-240 | 3.5×3.0 | 3.3×2.4 | 4 | 5 | 50 | 240 |

## 2.2 Materials properties

The steel material properties were obtained through the coupon test according to the requirements of the specifications [12]. Three specimens were tested for each member, and the average results are provided in Table 2.

**Table 2.** Properties of steel

| Name | Thickness (mm) | 0.2% proof stress (MPa) | Tensile strength (MPa) | The initial elastic modulus (GPa) | Fracture strain (%) |
|---|---|---|---|---|---|
| Steel sheathing | 0.8 | 423.14 | 451.02 | 212.17 | 24.95 |
| Stud and track | 1.8 | 342.33 | 493.07 | 178.49 | 25.34 |
| Column | 5 | 403.75 | 428.32 | 228.93 | 25.04 |
| Beam | 3 | 274.70 | 389.78 | 171.43 | 22.93 |

The sheathing and CFS framing are connected with cross-recessed countersunk head tapping screws with a diameter of 3.2mm. The single overlap shear test was conducted to obtain the load-deformation relationship of the CFS stud-sheet connection according to the specification (AISI TS-4-02) [13], and the test result is shown in Figure 3.

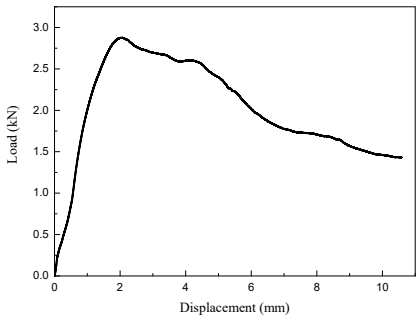


**Figure 3.** Shear load-deformation curve of the connection.

## 2.3 Test setup

The CFS shear wall and frame column were bolted to the steel base beam, which was fixed to the concrete floor slab with anchor bolts. The testing specimens were equipped with a 500 kN hydraulic actuator with ±250 mm stroke, and the movement of the hydraulic actuator was controlled electrically. The specimen was connected to the actuator with two loading plates and four long threaded rods. The horizontal loading was applied on the top of the specimen via the loading plate and threaded rods. Lateral supports with rollers were installed on both sides of the specimen to avoid out-of-plane displacement as shown in Figure 4.

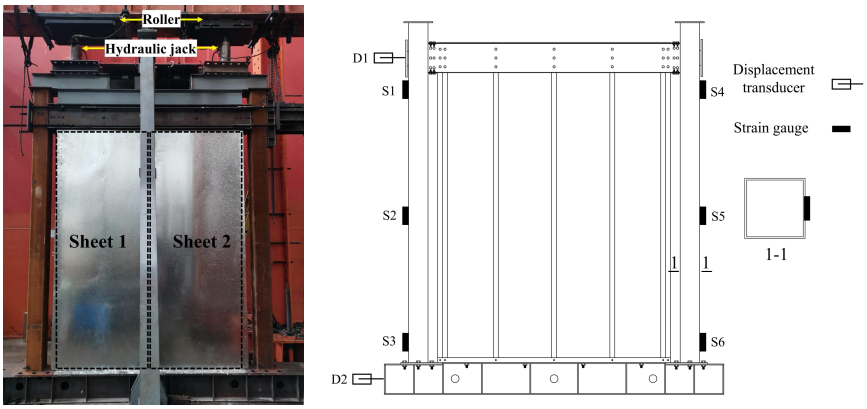


(a) Test setup (b) Measuring points

**Figure 4.** The test setup and measuring points.

The test data were collected through the transducers. The measuring point arrangement of the specimen is shown in Figure 4(b). The displacement transducers D1 and D2 measured the horizontal displacement of the top and bottom of the specimen, respectively. Strain gauges S1~S6 were used to measure the vertical strain of the frame column at different heights, and

gauges S7~S10 measured the vertical strain of the boundary studs of the CFS shear wall. The measuring frequency of the data acquisition system was 1Hz.

## 2.4. Loading protocol

The loading scheme followed the Chinese Specification [14]. A preload was conducted first which is taken as 10% of the ultimate load. According to the numerical prediction of the specimens, a preload of 10kN was applied to the specimens. The official loading started with a load-control mode, the amplitude for the first cycle is also selected as 10kN. After yielding, the displacement-control loading scheme was adopted, and the amplitudes of each cycle were shown in Figure 5. The loading speed is 5mm/min, and the test stopped when the load was less than 75% of the peak load.

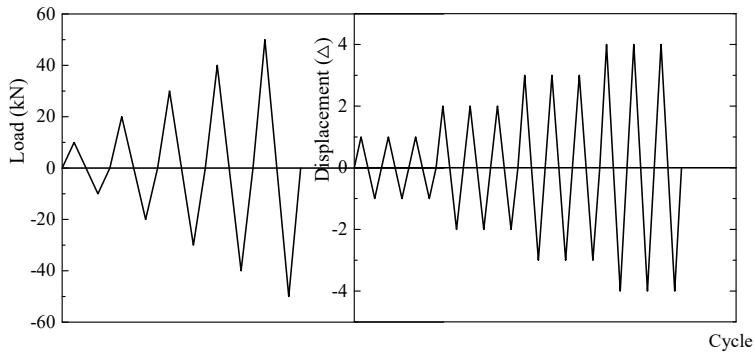


**Figure 5.** Loading scheme.

# 3. RESULTS AND DISCUSSIONS

## 3.1 Failure modes

The observed failure phenomena of the three specimens, as illustrated in Figures 6 and 7, reveal that the frame system sustained no significant damage throughout the cyclic test. Notably, the frame columns, frame beams, and their joints remained free from plastic deformation and damage. The degradation in strength and failure were exclusively noted in the steel-sheathed CFS shear walls, attributable primarily to buckling of the steel sheets, failure of the screw connections, and torsion of the studs.

(a) Initial loading (b) After loading (c) Connections failure (d) Corner failure

**Figure 6.** Failure phenomenon of specimen S-100-120.

The specimens featured a dual lateral force resistance system, comprising the frame system and the shear wall system. Post-testing examination indicated that the bolted connections within the specimens were intact, suggesting a robust and reliable linkage between the frame and the shear wall, capable of cooperative performance under seismic conditions. During the loading process, the shear wall emerged as the principal component for energy dissipation and lateral resistance. Upon the shear wall's failure, the frame system preserved its elastic state, thereby significantly enhancing the structure's collapse resistance and overall safety performance.

(a) Specimen S-50-120 (b) Specimen S-50-240

**Figure 7.** Failure phenomenon of specimen S-50-120 and S-50-240.

## 3.2 Hysteretic curves

The total lateral displacement at the top of the CFS shear walls is the sum of the displacement due to shear deformation, overall horizontal movement, and rotation of the walls. Given the steel frame's constraining effect on the test specimen, rotation is negligible compared to that observed in unrestrained CFS shear walls. Consequently, the specimen's horizontal displacement is determined by subtracting the overall horizontal displacement (D2) from the total displacement at the top (D1), as measured by the LVDTs. The load-displacement hysteresis curves of the specimens, depicted in Figure 8, show characteristics similar to those of bare CFS shear walls, including a pinching effect and suboptimal energy dissipation.

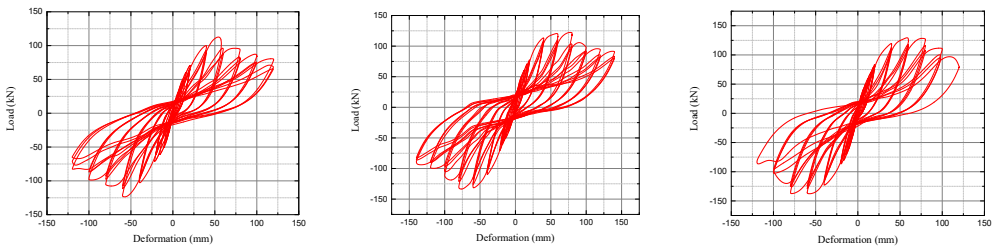


(a) Specimen S-100-120 (b) Specimen S-50-120 (c) Specimen S-50-240

**Figure 8.** Hysteretic curves of the specimens.

Initially, the specimens exhibit fusiform hysteresis loops, indicative of better energy dissipation. However, as loading progresses, failure of screw connections and buckling of the steel sheets were observed, and slip deformation increases. Towards the late stages of loading,

the screw connections at the shear wall's four corners predominantly fail, undermining the stressed skin action. This leads to a continuous decrease in specimen stiffness and a reduction in the energy dissipation capacity of the hysteresis loops.

## 3.3 Envelope curves and ductility

The main results of the test are shown in Table 3, and the envelope curves of the specimens are shown in Figure 9. $F_y$ and $\Delta_y$ is the yield strength and the corresponding displacement; $F_p$ and $\Delta_p$ is the peak load and the corresponding displacement; $F_u$ is the ultimate load which is 0.85 $F_p$, and $\Delta_u$ is the ultimate displacement. The yield limit was calculated using the equivalent energy elastic-plastic model (EEEP) [15]. The secant line was chosen so that the bilinear curve dissipates an identical amount of energy as the original curve as illustrated in Figure 10. The ductility factor is determined as follows: $\mu=\Delta_u/\Delta_y$, where $\Delta_u$ and $\Delta_y$ can be obtained from Figure 10.

**Table 3.** Test results

| Specimens | Direction | Yield point | | Peak point | | Ultimate point | | $\mu$ |
|---|---|---|---|---|---|---|---|---|
| | | $\Delta_y$/mm | $F_y$/kN | $\Delta_p$/mm | $F_p$/kN | $\Delta_u$/mm | $F_u$/kN | |
| S-100-120 | Positive | 37.3 | 98.5 | 54.3 | 115.8 | 73.9 | 98.5 | 2.0 |
| | Negative | 42.3 | 107.8 | 59.3 | 126.7 | 84.5 | 107.7 | 2.0 |
| | Average | 39.8 | 103.2 | 56.8 | 121.3 | 79.2 | 103.1 | 2.0 |
| S-50-120 | Positive | 35.2 | 107.5 | 78.6 | 124.8 | 94.6 | 106.1 | 2.7 |
| | Negative | 47.7 | 119.8 | 77.1 | 135.3 | 99.9 | 115.0 | 2.1 |
| | Average | 41.5 | 113.7 | 77.9 | 130.1 | 97.3 | 110.6 | 2.4 |
| S-50-240 | Positive | 35.9 | 114.5 | 78.1 | 132.9 | 100.9 | 113.0 | 2.8 |
| | Negative | 36.8 | 120.0 | 60.0 | 140.4 | 97.8 | 119.3 | 2.7 |
| | Average | 36.4 | 117.3 | 69.1 | 136.7 | 99.4 | 116.2 | 2.7 |

Overall, the load-displacement curves of the three specimens exhibit similar trends. Specifically, the average load-carrying capacities in the push-pull direction for specimens S-100-120, S-50-120, and S-50-240 are 121.3kN, 130.1kN, and 136.7kN, respectively; while the displacement ductility coefficients are 1.99, 2.34, and 2.75, respectively. Comparison reveals that reducing the screw spacing in the shear wall studs and increasing the vertical load on the specimens both enhance the load-carrying capacity and ductility coefficient. Observing the rate of load decrease in the final two loading cycles of the specimens' skeleton curves, specimen S-50-240 exhibited the fastest rate of decrease, yet its displacement ductility coefficient was higher than those of the specimens subjected to lower vertical loads. This phenomenon is attributed to the rapid load decline of specimen S-50-240 occurring after reaching an ultimate displacement corresponding to 85% of the load, with an average

ultimate displacement of 99.4mm, which is greater than that of the other two specimens. Furthermore, its average yield displacement was 69.1mm, less than those of the other specimens, resulting in a higher ductility coefficient.

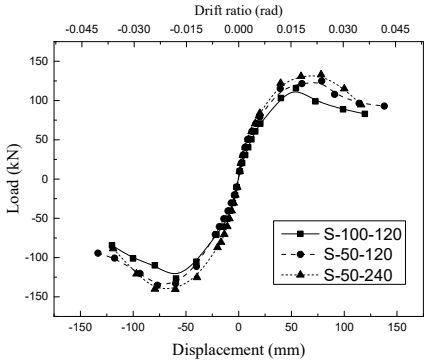


**Figure 9.** Envelope curves of specimens.

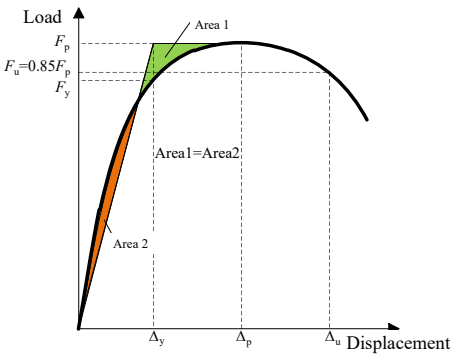


**Figure 10.** Definition of yielding and failure.

## 3.4. Energy dissipation

Figure 11 depicts the energy dissipation characteristics of the specimens throughout the loading process. Initially, the energy dissipation patterns of all three specimens were comparable. However, upon reaching a horizontal displacement of 60mm, a notable decline in energy dissipation was observed in specimen S-100-120, distinguishing it from the others. At a horizontal displacement of 100mm, the energy dissipation of specimen S-100-120 amounted to 7356.57 kN·mm, approximately 80% of that observed in the benchmark specimen S-50-120. This reduction can be attributed to the extensive failure of connections between the studs and steel sheets in specimen S-100-120, where the screwed connections serve as the primary contributors to the specimen's energy dissipation. Moreover, the specimen S-50-240 did not exhibit an increase in energy dissipation during the final loading cycle, aligning with the significant decrease in horizontal load observed for specimen S-50-240, a consequence of the substantial vertical load applied in the last cycle.

## 3.5. Stiffness degradation

The secant stiffness of the hysteresis curve was used to draw the stiffness degradation curve of the specimen, as shown in Figure 12.

The calculation method of secant stiffness $K_i$ is

$$K_i = \frac{|+F_i| + |-F_i|}{|+X_i| + |-X_i|} \tag{1}$$

Where $+F_i$ and $-F_i$ denote the peak load in the positive and negative directions of the $i$th stage loading, respectively, and $+X_i$ and $-X_i$ represent the peak displacement corresponding to the positive and negative directions of the $i$th stage loading.

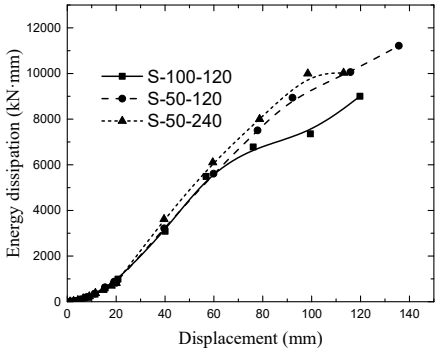


**Figure 11.** Energy dissipation of specimens.

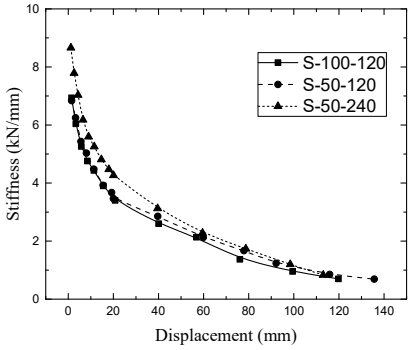


**Figure 12.** Stiffness degradation of specimens.

The stiffness degradation trend of the three specimens is similar, and the curves are generally smooth. The initial secant stiffness of specimens S-100-120 and S-50-120 is about 7.0kN/mm, and the initial stiffness of specimens S-50-240 with large vertical load is higher, about 8.3kN/mm. The stiffness of the specimen decreases rapidly with the increase of horizontal displacement. Before 40mm, the stiffness of specimen S-100-120 and S-50-120 is similar. After 40mm, the stiffness of specimen S-50-120 is higher than that of S-100-120, which corresponds to the fact that specimen S-50-120 reduces the screw spacing of the central stud, avoiding the failure of the stud-sheet connections in that region.

## 3.6. Strain analysis

Figure 13 presents the strain envelopes for frame columns in specimens S-100-120 and S-50-120, derived from data collected via strain gauges S1-S3. The envelopes exhibit a near-symmetrical behavior, with significant strain amplitudes observed at both the top and bottom of the column, escalating with the horizontal displacement of the specimen. The peak strain recorded in the columns approximated 1200 microstrain during testing, approaching the yield strain of the material. Conversely, the strain at the column's midpoint remained minimal and relatively constant, aligning with the expectation that the bending moment at the column's inflection point is zero.

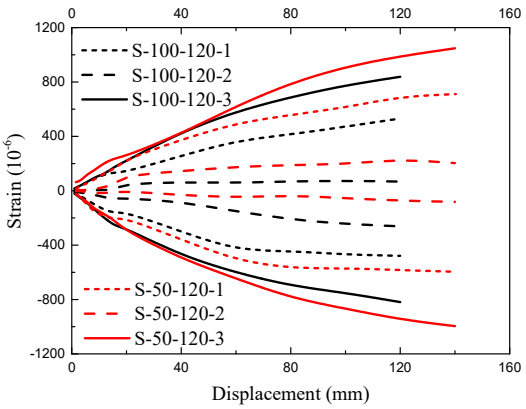


**Figure 13.** Strain envelopes of columns and corresponding material property.

# 4. CONCLUSIONS

The experimental investigation presented in this research focuses on a hybrid system comprising a HRS frame and a steel-sheathed CFS shear wall. Based on the findings of this experimental study, the following conclusions can be drawn:

1. Throughout the loading process, the bolted connections between the U-shaped steel beams and studs remained intact, indicating the reliability of the connection between the frame and shear wall. Both systems exhibited coordinated deformation under load, demonstrating their ability to function in tandem.

2. The specimens feature a dual lateral force resistance system comprising the frame and shear wall systems. During loading, the shear wall primarily dissipates energy and resists lateral forces. Even after the shear wall's failure, the frame system retains its elastic state, effectively enhancing the structure's collapse resistance and safety performance.

3. The shear bearing capacities of the hybrid structures were 121.3 kN, 130.1 kN, and 136.7 kN, with corresponding ductility coefficients of 1.99, 2.34, and 2.75, respectively. Adjusting the screw spacing of connections and the vertical load of the shear wall can enhance both the shear capacity and displacement ductility coefficient of the specimens. However, when the specimen's bearing capacity falls below 85% of its peak capacity, specimens subjected to higher vertical loads experience a faster decrease in bearing capacity.

## ACKNOWLEDGMENTS

This research was supported by the National Natural Science Foundation of China (Grant No. 51978151), and the Scientific Research Foundation of Graduate School of Southeast University (YBPY1963).

## REFERENCES

[1] Schafer, B. W. (2011). Cold-formed steel structures around the world: A review of recent advances in applications, analysis and design. *Steel Construction*, 4(3), 141-149.

[2] Balh, N., DaBreo, J., Ong-Tone, C., El-Saloussy, K., Yu, C., & Rogers, C. A. (2014). Design of steel sheathed cold-formed steel framed shear walls. *Thin-Walled Structures*, 75, 76-86.

[3] Yu, C., & Chen, Y. (2011). Detailing recommendations for 1.83 m wide cold-formed steel shear walls with steel sheathing. *Journal of Constructional Steel Research*, 67(1), 93-101.

[4] Yu, C. (2010). Shear resistance of cold-formed steel framed shear walls with 0.686 mm, 0.762 mm, and 0.838 mm steel sheet sheathing. *Engineering Structures*, 32(6), 1522-1529.

[5] Mohebbi, S., Mirghaderi, R., Farahbod, F., & Sabbagh, A. B. (2015). Experimental work on single and double-sided steel sheathed cold-formed steel shear walls for seismic actions. *Thin-Walled Structures*, 91, 50-62.

[6] Shamim, I., & Rogers, C. A. (2013). Steel sheathed/CFS framed shear walls under dynamic loading: numerical modelling and calibration. *Thin-Walled Structures*, 71, 57-71.

[7] Usefi, N., Ronagh, H., & Sharafi, P. (2020). Lateral performance of a new hybrid CFS shear wall panel for mid-rise construction. *Journal of Constructional Steel Research*, 168, 106000.

[8] Mortazavi, M., Sharafi, P., Ronagh, H., Samali, B., & Kildashti, K. (2018). Lateral behaviour of hybrid cold-formed and hot-rolled steel wall systems: Experimental investigation. *Journal of Constructional Steel Research*, 147, 422-432.

[9] Wang, X., & Ye, J. (2015). Reversed cyclic performance of cold-formed steel shear walls with reinforced end studs. *Journal of Constructional Steel Research*, 113, 28-42.

[10] Wang, X., & Ye, J. (2016). Cyclic testing of two-and three-story CFS shear-walls with reinforced end studs. *Journal of Constructional Steel Research*, 121, 13-28.

[11] Dao, T. N., & van de Lindt, J. W. (2013). Seismic performance of an innovative light-frame cold-formed steel frame for midrise construction. *Journal of Structural Engineering*, 139(5), 837-848.

[12] GB/T 228.1-2010. (2011). Metallic materials: tensile testing: part 1: method of test at room temperature. Beijing: China Standards Press. (in Chinese)

[13] AISI TS-4-02. (2002). Standard test methods for determining the tensile and shear strength of screws. Washington, DC: American Iron and Steel Institute.

[14] JGJ.101-96. (1997). Specification of Testing Methods for Earthquake Resistant Building. Beijing: China Academy of Building Research. (in Chinese)

[15] Park, R. (1989). Evaluation of ductility of structures and structural assemblages from laboratory testing. *Bulletin of the new Zealand society for earthquake engineering*, 22(3), 155-166.

# PROTECT2024